

Linearly dispersing electrons: Effects of magnetic coupling and disorder

Dissertation

zur Erlangung des Grades eines
Doktors der Naturwissenschaften

am Fachbereich Physik
der Freien Universität Berlin

vorgelegt von
Kevin Alan Madsen

Berlin, 2021

Erstgutachter: Prof. Dr. Piet W. Brouwer
Zweitgutachter: Prof. Felix von Oppen, PhD

Tag der Abgabe: 22.9.2021
Tag der Disputation: 18.2.2022

Selbstständigkeitserklärung

Name: Madsen

Vorname: Kevin Alan

Ich erkläre gegenüber der Freien Universität Berlin, dass ich die vorliegende Dissertation selbstständig und ohne Benutzung anderer als der angegebenen Quellen und Hilfsmittel angefertigt habe. Die vorliegende Arbeit ist frei von Plagiaten. Alle Ausführungen, die wörtlich oder inhaltlich aus anderen Schriften entnommen sind, habe ich als solche kenntlich gemacht. Diese Dissertation wurde in gleicher oder ähnlicher Form noch in keinem früheren Promotionsverfahren eingereicht.

Mit einer Prüfung meiner Arbeit durch ein Plagiatsprüfungsprogramm erkläre ich mich einverstanden.

Datum: 22.9.2021

Unterschrift:

Kurzfassung

In dieser Arbeit werden anhand von drei Beispielen die Effekte von Unordnung und magnetischer Kopplung auf Elektronen mit linearer Dispersionsrelation in verschiedenen Dimensionen untersucht. Zuerst vergleichen wir numerische und analytische Berechnungen der Zustandsdichte von Graphen, einem zweidimensionalen Material, und einem Weyl-Halbmethall in drei Dimensionen am Dirac- beziehungsweise Weylpunkt. Anders als bei Graphen, wo jede endliche Unordnungsstärke eine endliche Zustandsdichte am Diracpunkt zur Folge hat, bleibt sie bei dem Weyl-Halbmethall bis zu einer kritischen Unordnungsstärke am Weylpunkt null. Der Vergleich der numerischen Berechnung mit der analytischen zeigt zwar qualitativ gute Übereinstimmung aber kann quantitativ die Ergebnisse der Numerik nicht exakt reproduzieren. Das zweite System ist ein Interferometer bestehend aus den zwei eindimensionalen helikalen Randzuständen eines zweidimensionalen topologischen Isolators, wovon einer an einen magnetischen Isolator gekoppelt ist der die Zeitumkehrsymmetrie bricht. Diese magnetische Kopplung zusammen mit Interferenzeffekten hat zur Folge, dass bei dem Anschluss einer zeitunabhängigen Spannung an das Interferometer zeitabhängige Ströme fließen. Weiterhin sind in diesem Interferometer die Aharonov-Bohm Oszillationen aufgrund eines durch das Interferometer gelegten Flusses bei niedrigen angeschlossenen Spannungen stark unterdrückt. Als letztes wird eine Heterostruktur, bestehend aus einer Schicht Weyl-Halbmethall mit endlicher Dicke die auf einem Supraleiter plaziert wird, analysiert. Aufgrund der einseitigen Kopplung des Weyl-Halbmethalls an den Supraleiter fließt ein Gleichgewichtsstrom entlang der Grenzschicht zwischen den beiden Systemen. Durch den Vergleich von verschiedenen Parameterregionen kann gezeigt werden, dass dieser Strom hauptsächlich von den Fermi-Bögen (den topologisch geschützten Oberflächenzuständen des Weyl-Halbmethalls) transportiert wird.

Abstract

In this thesis we study systems with linearly dispersing electrons and the effects disorder and a magnetic coupling can have on them. We focus on three examples: First we study the effects of potential disorder on the density of states at the nodal points in two-dimensional graphene and in three-dimensional Weyl semimetals. We obtain high-precision numerical data for the density of states of single nodal points and compare it to analytical perturbation theory calculations. At weak disorder strength, our results for the Weyl semimetal show a semimetallic phase with (to numerical accuracy) zero density of states at the nodal point. At stronger disorder strength, we find a finite density of states at the nodal point, in agreement with theoretical expectations. Second we study the effects of a magnetic coupling on the one-dimensional helical edge states of a two-dimensional topological insulator incorporated in a two-arm interferometer geometry and we find that due to the coupling to a magnetic insulator and interference effects a time-independent bias voltage can give rise to time-dependent currents. Additionally, Aharonov-Bohm oscillations due to a flux through the device are strongly suppressed at small applied bias voltages. The third and last example is a layered heterostructure consisting of a finite-width slab of a magnetic Weyl semimetal placed on top of a superconductor. The asymmetry of the heterostructure caused by the superconductor only being coupled to one of the two surfaces of the slab leads to an equilibrium current that flows parallel to the interface and we are able to show that it is carried mostly by the Fermi-arc surface states of the Weyl semimetal.

List of publications

The following articles constitute the main part of this thesis, they are listed here in chronological order:

- Björn Sbierski, Kevin A. Madsen, Piet W. Brouwer, and Christoph Karrasch,
Quantitative analytical theory for disordered nodal points
Phys. Rev. B 96:064203, August 2017
<https://doi.org/10.1103/PhysRevB.96.064203>
This work is the basis for chapter 2. The initial idea was proposed by Björn Sbierski. I implemented the Kernel Polynomial Method (KPM) numerics, generated all numerical data, performed the perturbation theory calculations and made the figures. I contributed to the writing of the manuscript and revised it together with both co-authors. The functional renormalization group (fRG) calculations in this article were not done by me and are not part of this thesis; the KPM numerics and perturbation theory calculations are both completely independent of the corrections to the fRG part of this article published in the erratum **Phys. Rev. B 97:139903, April 2018**.
- Kevin A. Madsen, Piet W. Brouwer, Patrik Recher, and Peter G. Silvestrov,
Interference effects induced by a precessing easy-plane magnet coupled to a helical edge state
Phys. Rev. B 103:115142, March 2021
<https://doi.org/10.1103/PhysRevB.103.115142>
This work is the basis for chapter 3. The initial idea was proposed by Patrik Recher. I performed the calculations, obtained the results, made the figures and wrote the original manuscript which was then revised together with all co-authors.
- Kevin A. Madsen, Piet W. Brouwer, and Maxim Breitkreiz,
Equilibrium current in a Weyl semimetal–superconductor heterostructure
Phys. Rev. B 104:035109, July 2021
<https://doi.org/10.1103/PhysRevB.104.035109>
This work is the basis for chapter 4. The initial idea was proposed by Maxim Breitkreiz. I contributed to performing the calculations, obtained the main results, plotted them in the figures and contributed to writing the original manuscript which was then revised together with both co-authors.

The author has also published two additional articles, which are not part of this thesis:

- Kevin A. Madsen, Emil J. Bergholtz, and Piet W. Brouwer,
Topological equivalence of crystal and quasicrystal band structures
Phys. Rev. B 88:125118, September 2013
<https://doi.org/10.1103/PhysRevB.88.125118>
This article is based on my Bachelor's thesis.
- Kevin A. Madsen, Emil J. Bergholtz, and Piet W. Brouwer,
Josephson effect in a Weyl SNS junction
Phys. Rev. B 95:064511, February 2017
<https://doi.org/10.1103/PhysRevB.95.064511>
This article is based on my Master's thesis.

Contents

1	Introduction	1
1.1	Helical edge states	4
1.2	Graphene	11
1.3	Weyl semimetals	12
1.3.1	Interfaces between Weyl semimetals and superconductors . . .	18
1.3.2	Disordered Weyl semimetals	22
2	Calculation of the density of states of disordered nodal points in $d = 2$ and $d = 3$	25
2.1	Introduction	25
2.2	Setup	25
2.3	Density of states from the Kernel Polynomial Method	27
2.4	Generating correlated disorder realizations	29
2.5	Self-consistent perturbation theory	30
2.6	Comparison of results	32
2.7	Conclusion	34
3	Interference effects induced by a precessing easy-plane magnet coupled to a helical edge state	35
3.1	Introduction	35
3.2	Model	37
3.3	Right point contact “open”	43
3.3.1	Calculation of DC and AC currents	43
3.3.2	“Classical” vs. “quantum” magnet	49
3.4	Right point contact “closed”	50
3.5	Full interferometer	55
3.6	Finite- T enhancement of DC Aharonov-Bohm currents	57
3.7	Conclusion	60
4	Spontaneous current of a Weyl-semimetal - superconductor heterostructure	63
4.1	Introduction	63
4.2	Model	65
4.2.1	Normal region	66

4.2.2	Heterostructure	67
4.2.3	Block diagonalization, chirality, Fermi arcs	68
4.3	Equilibrium current	70
4.3.1	Scattering formulation	70
4.3.2	Reflection amplitudes of normal region	72
4.3.3	k_z -resolved current density for large W	74
4.3.4	Finite-size effects	78
4.3.5	Total current density	79
4.3.6	Numerical results	80
4.3.7	$[d\mathcal{I}_y(k_z)/d\mu]^{(s)}$ for $\mu \downarrow 0$	82
4.3.8	Continuity of the current in the limit $T_- \downarrow 0$	83
4.4	Discussion and conclusion	86
5	Conclusion	89
	Bibliography	91
	Acknowledgments	105

1 Introduction

Linear energy-momentum dispersion relations can appear in crystal bandstructures where two electronic bands touch at a nodal point. In the vicinity of such nodal points the dispersion relation of the electrons can be approximated as a linear function of the electron momentum. Whether such crossing points are stable depends on symmetry and dimensionality. If no symmetry is required for their stability they are called accidental degeneracies [1].

Some very famous examples of systems with linearly dispersing electrons around nodal points are the bulk electrons of $2d$ graphene [2, 3] close to the Dirac points, which are protected by symmetry, the edge states of a $2d$ topological insulator [4, 5] (a quantum spin Hall insulator), where the crossing is protected by topology and symmetry, and the bulk electrons in a $3d$ Weyl semimetal [6], with Weyl nodes protected by topology. These three examples are the main focus of the research of this thesis.

Linear dispersion relations are closely related to relativistic physics: The velocity of these electrons is a constant independent of momentum, just like for massless relativistic particles, albeit with velocities significantly smaller than the speed of light. The fact that in condensed matter systems in general the electron velocities are much lower than the speed of light allows the observation of relativistic physics at low energies if the systems host nodal points, making ones that do particularly interesting.

Of the examples mentioned above, topological insulators and Weyl semimetals feature spin-orbit coupling, a relativistic effect which leads to the locking of the direction of motion (momentum) of the electrons with their spin. In graphene relativistic spin-orbit coupling is also present but negligible; the bands that cross at the Dirac points are spin degenerate and the momentum couples to a pseudospin degree of freedom rather than to the true spin.

A consequence of time-reversal symmetry and spin-momentum locking in the case of $1d$ edge states of a $2d$ topological insulator is the very strong suppression of backscattering due to disorder or imperfections at the edge of said topological insulator: Only if the symmetry protecting the nodal point is broken can backscattering take place, as a spin flip is required upon backscattering. This suppression of backscattering also exists in $2d$ and $3d$, where states moving in opposite directions also have opposite spin due to spin-momentum locking, however unlike in $1d$ there

are intermediate states available to achieve backscattering after multiple scattering events which individually do not need to completely flip the spin.

For any realistic application it is very important to understand the effects of disorder on the electronic properties of these nodal points, since disorder is generically present in real materials and influences their electronic properties. Studying the effects a magnetic coupling has on nodal points is also important, as these couplings break time-reversal symmetry. Broken time-reversal symmetry is a requirement for the existence of spin-polarized currents and thus understanding how they can be manipulated by such magnetic couplings is necessary for the development of spintronics devices that work on the basis of spin currents rather than charge currents.

Systems with nodal points are also interesting candidates for the development of electronic devices with low power consumption due to the already mentioned protection by symmetry and/or topology that suppresses backscattering. Moreover, the possibilities for devices are almost endless if we consider incorporating systems with nodal points in stacks of multiple layers of different materials. Such layered heterostructures are common and very important for device applications, two famous examples are the transistor [7], consisting of layered semiconductors, and the Josephson junction [8], a device where a normal conductor is sandwiched between two superconductors. Josephson junctions are the basis for the superconducting quantum interference device (SQUID) [9] which is used to measure weak magnetic fields with high precision. Another important example are magnetic multilayers [10, 11] which feature a giant magnetoresistance, also with applications in magnetic field sensors.

In the main part of this thesis we will study the physics of nodal points in different dimensions in three chapters as follows.

First of all, chapter 2 of this thesis will be concerned with the consequences of potential disorder on the electronic density of states at nodal points in $2d$ and $3d$ (graphene and Weyl semimetal) which exhibit vastly different behavior: In $2d$, disorder of any strength gives a finite electronic density of states at the nodal point (the Dirac point), whereas in $3d$ the density of states initially remains zero at the nodal point (the Weyl point) up to a critical value of the disorder strength where it becomes finite, the so called non-Anderson transition [12] between semimetallic and metallic phases. This transition is distinct from the usual Anderson transition between metallic and insulating phases. We contribute evidence in favor of interpreting this transition as a true quantum phase transition, though it remains an open question that is debated in the literature.

Second, in chapter 3 we will study the consequences of locally breaking the time-reversal symmetry that protects edge state electrons of a $2d$ topological insulator from backscattering by a local coupling to a macroscopic magnetization in an interferometer device. Due to the spin polarization of the counterpropagating edge

states, flipping the spin upon backscattering from the magnetization is required and this leads to a conversion of a charge to a spin current, making such systems interesting for spintronics applications. In previous studies by Silvestrov et al. [13] and Meng et al. [14] it was found that this conversion of charge-to-spin has a surprising consequence: If a finite-length magnet is stacked on top of the edge of a topological insulator and a voltage bias is applied across this magnet, the resulting charge current is the same as it would be for the same edge without the magnet. The main goal of this part of the thesis will be the detection of the presence of such a magnet via interference effects by coupling a heterostructure consisting of a magnet stacked on top of a topological insulator edge to a second such edge without a magnet in an interferometer device. Along the way we find that the application of time-independent bias voltages to the device in question can give rise to time-dependent charge currents flowing through it, due to a combination of the effects of the backscattering from the magnetization and the interference of different paths an electron can take between leads. We also find a strong suppression of the Aharonov-Bohm oscillations in this interferometer for Fermi energies inside the magnet-induced gap.

Last of all, in chapter 4 we consider a layered heterostructure consisting of a finite-width normal region which is placed in between a superconductor on one side and the vacuum on the other. The normal region is modeled such that it can be in several distinct topological and trivial phases depending on the model parameters. Our main focus lies on the normal region being a magnetic Weyl semimetal and we find that the breaking of time-reversal symmetry gives rise to an equilibrium current parallel to the interface of normal region and superconductor. The main question we wish to answer is in what way the surface Fermi-arc states of the Weyl-semimetal phase contribute to this current. By comparing this equilibrium current for the different phases of our model we are indeed able to isolate the contribution of the Fermi-arc states, and we then argue that it can be interpreted as a signature of the chiral magnetic effect [15, 16] in real space, a non-equilibrium current that flows parallel to an applied magnetic field due to a chemical potential difference between Weyl nodes of opposite chirality. This equilibrium current also carries the signature of the so called “chirality blockade” [17] which affects bulk Weyl nodes and can lead to a blocking of Andreev reflection [18] from a superconductor.

Before we come to the original research that constitutes the main part of this thesis, we will first introduce and explain important concepts necessary for the understanding of our research and also present some other relevant results from the existing literature in order to give our research some additional context.

1.1 Helical edge states

As an introduction to the topic of chapter 3 we will now discuss some properties of $2d$ topological insulators, or quantum spin Hall insulators, and their $1d$ edge states, as well as present some results from existing research on the effects of a magnetic coupling on said edge states.

After the discovery of the integer quantum Hall effect [19], an effect that occurs in $2d$ electronic systems under the influence of strong magnetic fields which features quantized values of the Hall conductance, it was realized that topology can be used to distinguish and classify new phases of quantum matter that go beyond the standard Landau classification using spontaneously broken symmetries [4]. These topological phases feature an insulating bulk but host conducting edge states where two systems with different topological classifications interface. When a system undergoes a topological phase transition from one topological phase to another the aforementioned insulating bulk gap must close and reopen. For the integer quantum Hall effect the topological invariant is the Chern number C [4], an integer number defined in terms of the bulk band structure [see below, Eq. (1.3)] or, alternatively and equivalently, the number of conducting edge channels for an interface with a vacuum. These edge states are chiral, i.e. they propagate only in one direction, and have fixed spin. This is possible due to the breaking of time-reversal symmetry via the (strong) magnetic field. Later it was discovered that these chiral edge states can also exist without the external magnetic field, due to a combination of spin-orbit coupling and time-reversal symmetry breaking by a magnetization that replaces the external magnetic field. This is the quantum anomalous Hall effect. Materials with this property are called Chern insulators. The topological invariant that counts the number of chiral edge states is the same Chern number C previously mentioned that counts edge channels of the quantum Hall effect. It is defined as the surface integral of the Berry flux $\mathcal{F}^{ab}(\mathbf{k})$

$$\mathcal{F}^{ab}(\mathbf{k}) = \partial_{k_a} \mathcal{A}^b - \partial_{k_b} \mathcal{A}^a, \quad (1.1)$$

$$\mathcal{A} = -i \langle u(\mathbf{k}) | \nabla_{\mathbf{k}} | u(\mathbf{k}) \rangle, \quad (1.2)$$

where the $|u(\mathbf{k})\rangle$ are the Bloch wavefunctions of the valence band, as

$$\frac{1}{2\pi} \int dk_a dk_b \mathcal{F}^{ab}(\mathbf{k}) = C. \quad (1.3)$$

There are many other topological phases of quantum matter, but the one that is most relevant for the research discussed in chapter 3 of this thesis is the quantum spin Hall insulator [4], also called $2d$ topological insulator (TI), which preserves time-reversal symmetry. The quantum spin Hall phase can be understood as two stacked Chern insulators that are time-reversed copies of one another. The edge states are

then counterpropagating, have opposite spin and are called helical edge states. Even when coupling the two time-reversed layers (in a time-reversal symmetry preserving fashion) an odd number of such edge states will not gap out. In this case the edge state spin acquires a dependence on momentum (hence they are called helical). The right- and left-moving helical edge states form a Kramers pair, and Kramers theorem [4] dictates that these two bands must cross inside the energy gap. Close to this crossing point their dispersion is linear, i.e. velocity is independent of momentum. The topological invariant that classifies $2d$ topological insulators is the index $\nu \in \mathbb{Z}_2$ that takes on two distinct values for odd and even numbers of helical edge states.

As a prerequisite for chapter 3 we will now follow the discussion in Ref. [13] by Silvestrov et al. as the physics studied there is crucial to the understanding of that chapter.

As already mentioned, helical edge states are counterpropagating and have opposite spin due to the presence of time-reversal symmetry: In order to backscatter a spin flip is required. However, this is not possible without a time-reversal breaking (magnetic) coupling between the two helical states. To illustrate this we consider

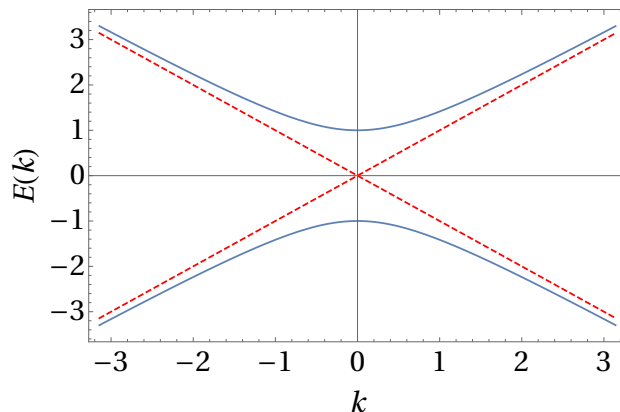


Figure 1.1: Energy levels $E(k) = \pm\sqrt{(\hbar vk)^2 + m^2}$ for $m = 0$ (red-dashed line) and $m = 1$ (solid-blue line). Any nonzero value of the coupling m opens a gap of magnitude $2m$ at the nodal point $k = 0$. $\hbar v$ has been set to 1.

the $1d$ toy model for two counterpropagating helical edge states with opposite spin defined by the Hamiltonian

$$H(k) = \begin{pmatrix} \hbar vk & m \\ m & -\hbar vk \end{pmatrix}, \quad (1.4)$$

with velocity v and energy eigenvalues

$$E(k) = \pm\sqrt{(\hbar vk)^2 + m^2}. \quad (1.5)$$

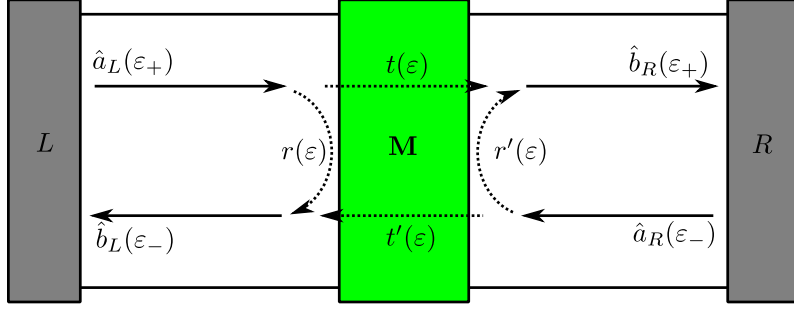


Figure 1.2: A helical edge state (solid-black arrows) is coupled to a magnet \mathbf{M} , shown in green, in between two leads (L, R) with chemical potentials μ_L and μ_R . The magnet breaks time-reversal symmetry locally and therefore opens a gap at the nodal point and allows for the electrons to be backscattered. The scattering problem is given in Eqs. (1.9), the scattering amplitudes $r(\varepsilon)$, $r'(\varepsilon)$, $t(\varepsilon)$ and $t'(\varepsilon)$ are indicated by the black-dashed arrows.

The energy eigenvalues $E(k)$ are plotted in Fig. 1.1 and it is clear that the crossing of the two energy levels can only exist if they are not coupled, i.e. for $m = 0$. This corresponds to the symmetry of this toy model, which is time-reversal symmetry represented by $\sigma_y H^*(-k) \sigma_y = H(k)$, that is broken by a nonzero m that couples opposite spins.

In Ref. [13] a helical edge state, see Fig. 1.2, is coupled locally to an easy-plane magnet described by a macroscopic magnetization $\mathbf{M} = \{M_x, M_y, M_z\}^T$ in the Hamiltonian

$$H = -i\hbar v_F \partial_x \sigma_z + h(x) \boldsymbol{\sigma} \cdot \mathbf{M} + \frac{1}{2} D M_z^2, \quad (1.6)$$

with anisotropy $D > 0$ and spin $\boldsymbol{\sigma}$. This coupling of the helical edge states to the magnetization \mathbf{M} is described by the smooth function $h(x)$ with the property that $h(x) \rightarrow 0$ for $x \rightarrow \infty$. It locally breaks time-reversal symmetry in the way we described previously, see Eq. (1.4) and Fig. 1.1, thus opening a gap in the electronic spectrum and allowing the electrons to be backscattered. Upon reflection by the magnetization an electron flips its spin and so the z component of the magnetization must change by one unit due to the conservation of total angular momentum, $M_z \rightarrow M_z \pm 1$, where the $+$ and $-$ signs correspond to electrons incident from the left or from the right, respectively. This allows the Hamiltonian to be decoupled into two sectors with magnetizations M_z for right-moving electrons and $M_z + 1$ for left-moving electrons via the transformation

$$\tilde{H} = \begin{pmatrix} 1 & 0 \\ 0 & \hat{m}_- \end{pmatrix} H \begin{pmatrix} 1 & 0 \\ 0 & \hat{m}_+ \end{pmatrix}, \quad (1.7)$$

where $\hat{m}_\pm = (m_x \pm im_y)/M_\perp$ are the operators that increase (+) or decrease (-) M_z by one unit and $M_\perp = \sqrt{(M - M_z)(M + 1 + M_z)}$. The operators \hat{m}_\pm have the

property that $\hat{m}_-\hat{m}_+ = \mathbb{1}$. The transformed Hamiltonian is

$$\tilde{H} = \left[-i\hbar v_F \partial_x + h(x)M_z - \frac{\hbar\omega_M}{2} \right] \sigma_3 + M_\perp h(x)\sigma_1, \quad (1.8)$$

neglecting small terms $\sim h(x)$ compared to the large term $\sim h(x)M_z$. This decoupling leads to a difference $\hbar\omega_M = D(M_z + 1/2)$ between the kinetic energies of the left- and right-moving electrons along the edge, where ω_M is the precession frequency of the (classical) magnetization \mathbf{M} around the z axis caused by the spin-transfer torque supplied by the electrons flipping their spin upon backscattering. The maximal gap in the spectrum is $2\varepsilon_{gap}$, with $\varepsilon_{gap} = \max_x h(x)M_\perp$.

The scattering problem describing this setup, see Fig. 1.2, can be formulated using the reflection and transmission amplitudes $r(\varepsilon)$, $r'(\varepsilon)$, $t(\varepsilon)$, $t'(\varepsilon)$ as

$$\begin{aligned} \hat{b}_L(\varepsilon_-) &= r(\varepsilon)\hat{a}_L(\varepsilon_+) + t'(\varepsilon)\hat{a}_R(\varepsilon_-), \\ \hat{b}_R(\varepsilon_+) &= r'(\varepsilon)\hat{a}_R(\varepsilon_-) + t(\varepsilon)\hat{a}_L(\varepsilon_+), \end{aligned} \quad (1.9)$$

with the annihilation operators for outgoing $\hat{b}_L(\varepsilon)$, $\hat{b}_R(\varepsilon)$ and incoming electrons $\hat{a}_L(\varepsilon)$, $\hat{a}_R(\varepsilon)$ on the left (L) and right (R) of the magnet at energies $\varepsilon_\pm = \varepsilon \pm \hbar\omega_M/2$. It is important to note that $r(\varepsilon) \rightarrow 0$ for electrons with energies $|\varepsilon| \gg \varepsilon_{gap}$.

This single-particle picture can be applied to the many-particle problem under the assumption that the fluctuations of M_z caused by the simultaneous scattering of multiple electrons are small compared to the macroscopic magnetization M . This is equivalent to the condition that fluctuations of the precession frequency ω_M are small compared to ω_M itself. In that case we may solve the scattering problem at the mean value $\langle M_z \rangle$. The current flowing through the helical edge to the left of the magnet is then given by

$$I_L = \frac{e}{h} \int d\varepsilon d\varepsilon' \left[\overline{\hat{a}_L^\dagger(\varepsilon)\hat{a}_L(\varepsilon')} - \overline{\hat{b}_L^\dagger(\varepsilon)\hat{b}_L(\varepsilon')} \right], \quad (1.10)$$

where $\overline{\cdots}$ denotes the expectation value, and

$$\overline{\hat{a}_\alpha^\dagger(\varepsilon)\hat{a}_\beta(\varepsilon')} = f_\alpha(\varepsilon)\delta(\varepsilon - \varepsilon')\delta_{\alpha\beta}, \quad \alpha, \beta = \text{L, R}, \quad (1.11)$$

is the distribution function $f_\alpha(\varepsilon) = 1/[e^{(\varepsilon - \mu_\alpha)/k_B T_\alpha}]$ of the incoming electrons in lead $\alpha = \text{L, R}$ at temperature T_α and chemical potential μ_α . A similar expression can be found for the current to the right of the magnet. By substituting Eqs. (1.9) and using the fact that the transmission probability through the magnet is the same for electrons incoming from either side, $|t(\varepsilon)|^2 = |t'(\varepsilon)|^2$, the current to the left of the magnet can be written as

$$I_L = \frac{e}{h} \int d\varepsilon \left[f_L(\varepsilon_-) - |r(\varepsilon)|^2 f_L(\varepsilon_+) - |t(\varepsilon)|^2 f_R(\varepsilon_-) \right]. \quad (1.12)$$

Application of a bias voltage V

$$\mu_L = \mu + eV/2, \quad \mu_R = \mu - eV/2, \quad (1.13)$$

across the magnet leads to a finite out-of-plane magnetization component M_z as the reflection rates of electrons on the right- and left-hand sides are initially not in balance. The rate of change of M_z is the difference of reflection rates for the electrons incoming from the left- and right-hand side of the magnet,

$$\langle \dot{M}_z \rangle = \frac{1}{h} \int d\varepsilon |r(\varepsilon)|^2 [f_L(\varepsilon_+) - f_R(\varepsilon_-)], \quad (1.14)$$

which is a convergent integral since as mentioned before $r(\varepsilon) \rightarrow 0$ for $|\varepsilon| \gg \varepsilon_{gap}$. If both leads are at the same temperature the stationary condition, $\langle \dot{M}_z \rangle = 0$, is reached for $\hbar\omega_M = eV$. The stationary current across the magnet is found by inserting Eq. (1.14) into Eq. (1.12) and using $|r(\varepsilon)|^2 + |t(\varepsilon)|^2 = 1$,

$$I_L = I_R = \frac{e}{h} \int d\varepsilon [f_L(\varepsilon_-) - f_R(\varepsilon_-)] = \frac{e^2}{h} V, \quad (1.15)$$

which is quite surprising as this is the current expected in the absence of a magnet. The same result was also found by Meng et al. [14] who solved the problem by transforming into the rotating frame of the precessing magnetization. This transformation is analogous to the transformation given in Eq. (1.7).

The amount of charge Q that is transported through the magnet per revolution of the precessing magnetization \mathbf{M} is exactly e , as can be seen by integrating Eq. (1.15) over one period $T_M = 2\pi/\omega_M = h/eV$ of the precessing magnetization

$$Q = \int_0^{T_M} dt \frac{e^2}{h} V = e, \quad (1.16)$$

making this setup of a helical edge state coupled to a precessing magnetization equivalent to a Thouless pump [20] operated in reverse or equivalently the quantum motor considered in Ref. [21]. The crucial ingredient for this equivalence is the energy difference of precisely $\hbar\omega_M$ between left- and right-moving helical modes due to the presence of the precessing magnet.

It is the result shown in Eq. (1.15) that motivates the question behind the research presented in chapter 3: How can the presence of the magnet be detected, if the current flowing along the edge is the same as if it were absent?

A natural way of attempting to answer this question is to embed such an edge coupled to a magnetization in an interferometer geometry and look for interference effects caused by the precessing magnetization. The simplest interferometer geometry compatible with the conservation of time-reversal symmetry away from the

magnet requires four helical leads, i.e., two separate edges that are coupled in two places in a time-reversal conserving fashion, see Fig. 1.3.

In chapter 3 we will study such a device consisting of two helical edges in a four-lead interferometer geometry, where one of the arms is locally coupled to a magnet enabling backscattering of the helical states. We find that interference of different electron paths through the interferometer gives rise to time-dependent currents for time-independent bias voltages applied to the interferometer leads due to backscattering of electrons from the magnetization. Furthermore, it turns out that Aharonov-Bohm (AB) oscillations are suppressed for small enough applied biases.

Similar interferometers as the one we study in chapter 3 but without the coupling to a magnet and chiral edge states rather than helical ones were experimentally studied in [22, 23, 24]. They display the expected Aharonov-Bohm [25] oscillations due to the Aharonov-Bohm flux threaded through the interferometer. Coherent transport through such a minimal four-lead interferometer with chiral edge states that gives rise to the aforementioned AB oscillations can be described using scattering theory. To achieve this, we pick eight reference positions labeled $i = 1, 2, \dots, 8$ in the interferometer, see Fig. 1.3. These reference positions are chosen in close proximity to the point contact region, where scattering between the chiral edge states is possible, see the right-hand panel of Fig. 1.3. At each of these reference positions i we consider creation and annihilation operators $\hat{a}_i^\dagger(\varepsilon)$ and $\hat{a}_i(\varepsilon)$ for an electron in a particle-flux normalized scattering state at energy ε . The red arrows in Fig. 1.3 indicate the direction of the chiral states and the positive current direction. The operators $\hat{a}_i(\varepsilon)$ and the corresponding creation operators $\hat{a}_i^\dagger(\varepsilon)$ are related to the current I_i at reference position i as [26, 27]

$$I_i = \frac{e}{h} \int d\varepsilon d\varepsilon' \overline{\hat{a}_i^\dagger(\varepsilon) \hat{a}_i(\varepsilon')}. \quad (1.17)$$

Once again, $\overline{\dots}$ denotes the expectation value. Electrons coming in from the two ideal sources (corresponding to the reference positions $i = 1, 7$) are in thermal equilibrium at temperature T_i and chemical potential eV_i ,

$$\overline{\hat{a}_i^\dagger(\varepsilon) \hat{a}_i(\varepsilon')} = f_i(\varepsilon) \delta(\varepsilon - \varepsilon'), \quad i = 1, 7, \quad (1.18)$$

where $f_i(\varepsilon) = [1 + e^{(\varepsilon - eV_i)/k_B T_i}]^{-1}$ is the Fermi-Dirac distribution function.

Scattering is elastic at the two point contact regions. They are described by the 2×2 scattering matrices $S^{(C1)}$ and $S^{(C2)}$. We assume that the point contact regions are small enough so that $S^{(C1)}$ and $S^{(C2)}$ may be taken independent of the energy ε ,

$$\begin{pmatrix} \hat{a}_2(\varepsilon) \\ \hat{a}_4(\varepsilon) \end{pmatrix} = S^{(C1)} \begin{pmatrix} \hat{a}_1(\varepsilon) \\ \hat{a}_3(\varepsilon) \end{pmatrix}, \\ \begin{pmatrix} \hat{a}_6(\varepsilon) \\ \hat{a}_8(\varepsilon) \end{pmatrix} = S^{(C2)} \begin{pmatrix} \hat{a}_5(\varepsilon) \\ \hat{a}_7(\varepsilon) \end{pmatrix}. \quad (1.19)$$

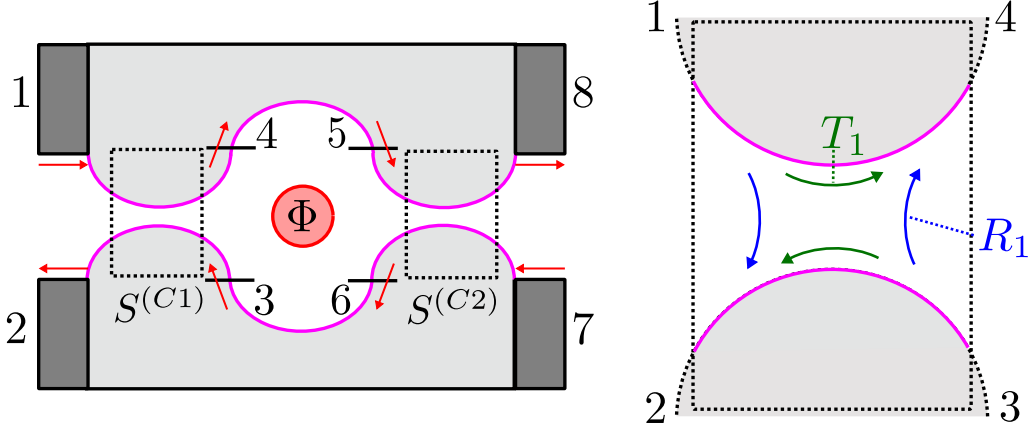


Figure 1.3: In the theoretical description, currents are calculated for eight reference points $i = 1, 2, \dots, 8$, as shown in the left panel. The chiral states (pink) move in the “positive” current direction indicated by the red arrows. The electron spins on both edges point in the same direction. The two tunneling point contacts between the opposing helical edge states are described by scattering matrices $S^{(C1)}$ and $S^{(C2)}$. The definitions of the transmission coefficients T_1 and the reflection coefficient R_1 for the left tunneling point contact are shown in the right panel. The device is threaded by an Aharonov-Bohm flux Φ [25].

Absorbing eventual phase factors into the definitions of the operators \hat{a}_i , this implies that without loss of generality these matrices can be parametrized as

$$S^{(Cj)} = \begin{pmatrix} \sqrt{R_j} & -\sqrt{T_j} \\ \sqrt{T_j} & \sqrt{R_j} \end{pmatrix}, \quad (1.20)$$

with $R_j + T_j = 1$ and $j = 1, 2$. As can be seen in Fig. 1.3, R_j and T_j are the probabilities for reflection via point contact j (changing the edge) and transmission along the same edge, respectively. Note that we assume both upper and lower chiral edge state spins point in the same direction, i.e. there are no spin flips possible anywhere in the interferometer. This can be achieved if both of the edge states in question belong to the same Chern insulator, for example if the central area of a Chern insulator is removed by etching and contacts are added, as seen in Fig. 1.3.

The operators at the two ends of the upper interferometer arm at reference positions “4” and “5” (and also “3” and “6”) are simply related by a phase factor,

$$\begin{aligned} \hat{a}_5(\varepsilon) &= e^{ik(\varepsilon)L+i\phi} \hat{a}_4(\varepsilon), \\ \hat{a}_3(\varepsilon) &= \hat{a}_6(\varepsilon). \end{aligned} \quad (1.21)$$

Here we have chosen a gauge such that all phase factors, including the AB phase shift $\phi = e\Phi/\hbar$ from the magnetic flux Φ , are accumulated for the propagation between

reference positions “4” and “5”. Further, L is the length of the interferometer arm and $k(\varepsilon) = k_F + \varepsilon/\hbar v_F$, with k_F the Fermi wavenumber and v_F the Fermi velocity. The energy ε is measured with respect to the Fermi level.

Taken together, Eqs. (1.19) and (1.21) give a set of six linear equations, which allow us to express all operators \hat{a}_i at the reference positions $i = 4, 5, 6, 7$ and at the drains $i = 2, 8$ in terms of the two operators \hat{a}_1, \hat{a}_7 describing electrons incident from the sources. Using the solution of this set of equations we can express the ϕ -dependent AB currents at the drains $i = 2, 8$, which is what we are interested in. These solutions in the drains $i = 2, 8$ are

$$\begin{aligned}\hat{a}_2(\varepsilon) &= \frac{-\sqrt{R_1} + e^{i(k(\varepsilon)L+\phi)}\sqrt{R_2}}{e^{i(k(\varepsilon)L+\phi)}\sqrt{R_1R_2} - 1}\hat{a}_1(\varepsilon) - \frac{\sqrt{T_1T_2}}{e^{i(k(\varepsilon)L+\phi)}\sqrt{R_1R_2} - 1}\hat{a}_7(\varepsilon), \\ \hat{a}_8(\varepsilon) &= -\frac{\sqrt{T_1T_2}}{e^{i(k(\varepsilon)L+\phi)}\sqrt{R_1R_2} - 1}\hat{a}_1(\varepsilon) + \frac{-\sqrt{R_2} + e^{i(k(\varepsilon)L+\phi)}\sqrt{R_1}}{e^{i(k(\varepsilon)L+\phi)}\sqrt{R_1R_2} - 1}\hat{a}_7(\varepsilon).\end{aligned}\quad (1.22)$$

We assume that scattering processes at the two point contacts where an electron switches chiral edges are much more unlikely than ones where the electron stays in the same edge, i.e. $T_j \gg R_j$. To lowest non-trivial order (neglecting terms $\propto R_j$) in the reflection amplitude $\sqrt{R_j}$ the ϕ -dependent contributions to the currents $\delta I_i(\phi)$ at the drains $i = 2, 8$ are then calculated from Eqs. (1.17, 1.22) as

$$\begin{aligned}\delta I_2(\phi) &= \frac{2e}{h} \int d\varepsilon \sqrt{R_1R_2} \cos(k(\varepsilon)L + \phi) [f_7(\varepsilon) - f_1(\varepsilon)], \\ \delta I_8(\phi) &= -\delta I_2(\phi).\end{aligned}\quad (1.23)$$

We choose the biases in the leads $i = 1, 7$ as $V_1 = V$ and $V_7 = 0$. Making the additional simplification that $eVL/\hbar v_F \ll 1$ allows us to replace $k(\varepsilon) \rightarrow k_F$, the integration in Eqs. (1.23) can be performed and the result is

$$\delta I_2(\phi) = \frac{2e}{h} \sqrt{R_1R_2} \cos(k_F L + \phi) eV. \quad (1.24)$$

This interference current oscillating with the AB-phase ϕ is the expected result from such an AB-interferometer. A very similar scattering approach to the one above is used to calculate the currents for the case that one of the interferometer arms is exchange-coupled to a magnet in chapter 3.

1.2 Graphene

As a preparation for chapter 2 we will first discuss some properties of the linear dispersion relations around the nodal points in the band structures of graphene and the effect potential disorder has on them, as this will be the topic of that chapter.

Graphene is a $2d$ material consisting of carbon atoms on a hexagonal lattice with two triangular sublattices [2, 3]. The dispersion relation features two (due to the combination of inversion, time-reversal and a C_3 rotation symmetry of the lattice) Dirac points $\mathbf{K} = \{2\pi/(3a), 2\pi/(3\sqrt{3}a)\}^T$ and $\mathbf{K}' = \{2\pi/(3a), -2\pi/(3\sqrt{3}a)\}^T$, with $a \approx 0.142\text{nm}$ the distance between two carbon atoms, at the edge of the Brillouin zone where two spin-degenerate bands touch. These bands are well described by a linear-in-momentum dispersion relation

$$H_{2d}(\mathbf{k}) = \hbar v_F \mathbf{k} \cdot \boldsymbol{\sigma} = \hbar v_F (\pm \sigma_x k_x + \sigma_y k_y), \quad (1.25)$$

close to these nodal points, where the $+$ sign is for the node at \mathbf{K} and the $-$ sign for the one at \mathbf{K}' . Momentum \mathbf{k} is defined relative to the Dirac points. The $\boldsymbol{\sigma}$ -degree of freedom in this case is a pseudospin rather than true spin. The electrons thus behave like massless relativistic particles called Dirac electrons, as their velocity v_F is independent of momentum, though much slower than the speed of light (roughly by a factor of 300). Due to this, graphene allows for the observation of relativistic effects [2, 3] at low electron energies, such as Klein tunneling and the “Zitterbewegung” of the electrons.

In chapter 2 we wish to study the effects of intra-nodal potential disorder, i.e. local fluctuations of the potential, on a single Dirac point. This is only possible if we can ensure that the disorder does not couple the two Dirac points, which we do by using a correlated disorder model providing us with a characteristic length scale ξ . For the momentum-space separation Δk between the nodal points this characteristic length must fulfill the condition $\xi \Delta k \gg 1$ so that intra-nodal scattering dominates over inter-nodal scattering, allowing us to obtain results for the density of states of individual nodal points with potential disorder. We achieve this by using an efficient numerical method, the Kernel Polynomial Method (KPM), and also analytically from first- and second-order perturbation theory. We compare the high-precision KPM results to the perturbation theory calculation and show that second-order perturbation theory improves upon the first-order calculation and gives qualitatively correct results. Unlike for $3d$ nodal points of Weyl semimetals, introduced in the next chapter, the density of states of graphene becomes finite at any finite disorder strength. Other effects of disorder on graphene have been studied extensively, see Ref. [28] for a review of the subject.

1.3 Weyl semimetals

Nodal points in $3d$ are either called Dirac nodes, if the bands are degenerate, or Weyl nodes if not. The degeneracy of bands is determined by symmetry: The presence of both inversion and time-reversal symmetry guarantees doubly degenerate bands.

Weyl semimetals, in turn, defined by the presence of Weyl nodes close to the Fermi surface, break at least one of these two symmetries. In general, any two-band Hamiltonian in $3d$ can be expanded [6] in terms of the Pauli matrices in the following way

$$H(\mathbf{k}) = g_0(\mathbf{k})\sigma_0 + g_x(\mathbf{k})\sigma_x + g_y(\mathbf{k})\sigma_y + g_z(\mathbf{k})\sigma_z, \quad (1.26)$$

with four \mathbf{k} -dependent coefficients $g_i(\mathbf{k})$. Here, the Pauli matrices σ_i represent the 2 bands. This is a generalization of the $1d$ toy model of Eq. (1.4). Since the g_0 coefficient is proportional to the unit matrix σ_0 it corresponds to a uniform shift in energy and can be safely ignored, setting $g_0 = 0$. Then, in order for the bands to touch the three other coefficients g_x , g_y and g_z must be each individually adjusted to zero, as the energy gap separating the two bands is $\Delta E = 2\sqrt{g_x^2 + g_y^2 + g_z^2}$. Each condition $g_i = 0$ defines a contour and a gap closing occurs at an intersection of these contours. In $3d$ the contours are surfaces and three surfaces generically intersect at a point, hence one may expect nodal points even in the absence of symmetries. These are called accidental degeneracies [1]. In $2d$ the contours correspond to curves, but three curves will only intersect at a single point if further criteria (related to symmetry) are satisfied. In $1d$ the situation is even more stark, with contours corresponding to individual points. In $1d$ or $2d$, if the perturbation breaks the symmetry condition a gap is opened. For the $3d$ case discussed here, adding a perturbation $V = \sum_i V_i \sigma_i$ will only shift the location of the nodal point.

Fermionic excitations around these Weyl nodes have a well-defined chirality of $C = \pm 1$, defined by $C = \text{sign}(v_x \cdot v_y \times v_z)$, with the velocities given by $v_i = \nabla_{\mathbf{k}} g_i(\mathbf{k})|_{\mathbf{k}=\mathbf{k}_0}$ and \mathbf{k}_0 the position of the node. It turns out that this chirality C is identical to the Chern number defined in Eq. (1.3) with the integral now being over a surface encircling the Weyl node [4, 6]. Depending on the sign of C Weyl nodes act either as sources or sinks of Berry flux $\mathcal{F}^{ab}(\mathbf{k})$, which is defined in Eq. (1.2). Integrating the Berry flux over a closed surface surrounding a Weyl node thus gives its chirality C , see Eq. (1.3). If such a surface, shown in orange/blue in Fig. 1.4, is expanded to include the entire Brillouin zone, the integral vanishes as the Brillouin zone does not have a surface. Therefore, Weyl nodes must always come in pairs of opposite chirality, a fact known as the Nielsen-Ninomiya theorem [29]. This provides a topological argument for the stability of Weyl nodes towards perturbations as mentioned above. Due to this topological nature of the Chern number, Weyl nodes can not disappear unless two Weyl nodes of opposite chirality meet in momentum space where they annihilate.

Close to the Weyl nodes $\pm\mathbf{k}_0$ the dispersion can be well approximated as

$$H_{3d}(\mathbf{k}, C) = C\hbar v_F \mathbf{k} \cdot \boldsymbol{\sigma} = C\hbar v_F (\sigma_x k_x + \sigma_y k_y + \sigma_z k_z), \quad (1.27)$$

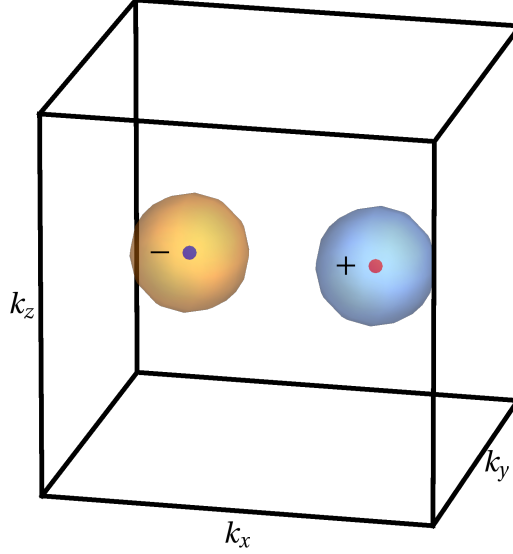


Figure 1.4: Depiction of a Brillouin zone with two Weyl nodes in red and blue at momenta $\pm\mathbf{k}_0$ and chirality $C = \pm 1$ which is given by integration of the Berry flux on the orange and blue surfaces. Figure adapted from Ref. [6].

for the simplest case of two Weyl nodes of opposite chirality and an isotropic dispersion. Here, momentum \mathbf{k} is defined relative to the position of the node $\pm\mathbf{k}_0$. A Weyl semimetal with two nodes may be realized if inversion symmetry is preserved but time reversal symmetry is broken. A time-reversal-symmetric Weyl semimetal with broken inversion symmetry hosts at least four Weyl nodes (or multiples of four), since time-reversal symmetry converts between Weyl nodes at momenta \mathbf{k} and $-\mathbf{k}$ but preserves the chirality, which in turn must vanish when summed over all Weyl nodes as mentioned previously.

The topic of chapter 4 is a heterostructure where a finite-length slab of Weyl semimetal is placed in between the vacuum and a superconductor. This requires the introduction of some additional properties of Weyl semimetals. We will also present results from the existing literature on similar heterostructures that contain Weyl semimetals.

As mentioned above, Weyl nodes always come in pairs of opposite chirality. They are sources and sinks of Berry flux and feature surface states at boundaries with other topological phases. The major difference between these Fermi-arc surface states ($2d$) and the ($1d$) edge states of a $2d$ topological insulator discussed in chapter 1.2 is their dimensionality and whereas the bulk of a topological insulator is gapped, the bulk of a Weyl semimetal is not. To understand the origin of the Fermi-arc states consider a Weyl semimetal with two nodes located at $k_x = \pm k_0$ due to broken time-reversal symmetry. Then it can be shown that any $2d$ plane labeled by k_x in between the

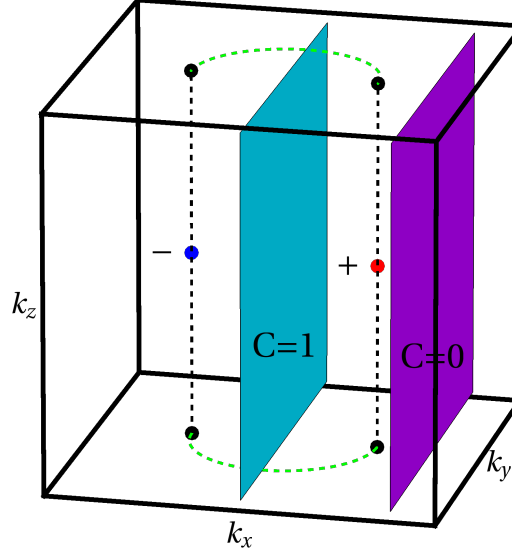


Figure 1.5: Depiction of a Brillouin zone with two Weyl nodes in red and blue at momenta $\pm\mathbf{k}_0$ and Chirality $C = \pm 1$. The blue and purple surfaces indicate $2d$ band structures labeled by k_x with a Chern number of $C = 1$ and $C = 0$ respectively, i.e. the $C = 1$ surface and any such surface that lies in between the nodes can be thought of as the $2d$ Brillouin zone of a Chern insulator with one counterpropagating edge state on opposite surfaces where the Weyl semimetal is terminated. These edge states of all $C = 1$ surfaces taken together form the Fermi-arc surface states, indicated by the green-dashed lines, that connect the projections of the Weyl nodes shown as black points. These two Fermi-arc edge states are located on opposite sides of the Weyl semimetal in real space. Figure adapted from Ref. [30].

Weyl nodes defines the Brillouin zone of a $2d$ Chern insulator with a chiral edge state, see Fig. 1.5. All of these edge states at fixed k_x in between the Weyl nodes at $k_x = \pm k_0$ connect and form the Fermi arc. In a hybrid real-space momentum-space picture, the Fermi arcs exist on surfaces in real space where the Weyl semimetal is terminated by a material in a different topological phase for which the projections of the Weyl nodes onto the corresponding surface Brillouin zone do not coincide. They connect the projections of the two Weyl points onto the surface Brillouin zone. On opposite sides of such a Weyl-semimetal slab in real space the chiral Fermi-arc edge states propagate in opposite directions. In momentum space these two Fermi arcs together with the bulk form closed electron orbits, the so called “Weyl orbits” as the two Fermi arcs although separated in real space are connected via the Weyl points through the bulk, see Fig. 1.5. If a magnetic field is applied to a finite-size Weyl semimetal with broken time-reversal symmetry perpendicular to the separation of the two Weyl nodes in momentum space, the Lorentz force acting on the electrons

will cause them to move along these closed orbits, see Fig. 1.5. We see that these orbits connect surface Fermi arcs and bulk states, and also opposite surfaces of the Weyl semimetal.

As we will study a heterostructure featuring a magnetic Weyl semimetal it is important to discuss another unusual response of Weyl semimetals to magnetic fields, a relativistic effect called the chiral anomaly [31], which is the nonconservation of chiral charge in the presence of parallel electric and magnetic fields. This can

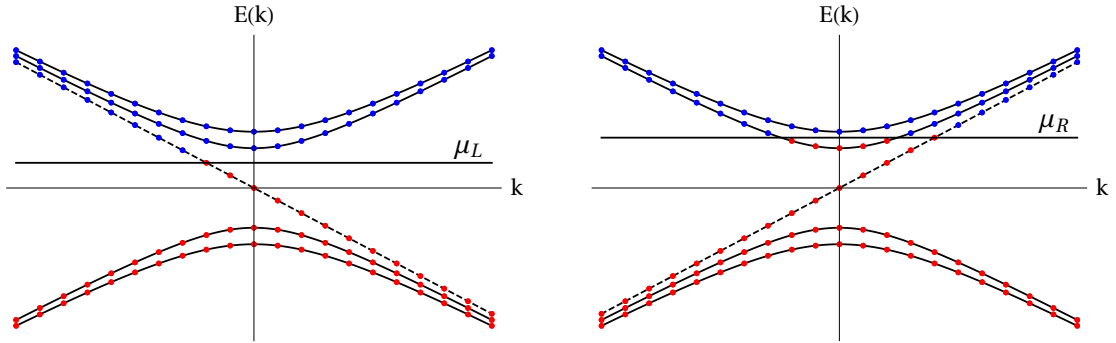


Figure 1.6: Application of a magnetic field $\mathbf{B} \parallel \mathbf{k}$ along the momentum direction \mathbf{k} that separates the Weyl nodes gives rise to the Landau-level dispersion shown here. The zeroth Landau levels (black-dashed lines) are chiral. Applying an electric field $\mathbf{E} \parallel \mathbf{B}$ along the same direction causes the imbalance of chiral charge, indicated by the two different chemical potentials $\mu_{L/R}$. Red/blue dots indicate states that are occupied/empty. This is the chiral anomaly. Since the chiral Landau levels are connected far below the Fermi energy the chiral anomaly produces a current that compensates the charge imbalance, this is the chiral magnetic effect. Figure adapted from Ref. [6].

be understood as follows. Application of a magnetic field to a Weyl semimetal with a pair of opposite chirality Weyl nodes gives rise to two chiral Landau levels, which disperse linearly along or opposite to the field, depending on the chirality of the associated Weyl node, see Fig. 1.6. An electric field \mathbf{E} applied parallel to the magnetic field \mathbf{B} then pumps charge from one Weyl node to the other due to spectral flow. This is possible as the two chiral Landau levels are connected far below the Fermi level and render this system effectively one dimensional. The transferred charge is

$$\frac{dn_{\pm}}{dt} = \pm \frac{e^2}{h^2} \mathbf{E} \cdot \mathbf{B}. \quad (1.28)$$

This process is balanced by internode scattering. The associated non-equilibrium

distribution gives rise to a current

$$J_{CME} = \frac{e^2}{\hbar^2} |\mathbf{B}| \Delta\mu. \quad (1.29)$$

This is called chiral magnetic effect (CME). The current is proportional to the difference $\Delta\mu = \mu_R - \mu_L$ of the chemical potentials of the two Weyl nodes caused by the electric field and flows between them parallel to the direction of the magnetic field.

As shown by O'Brien et al. [15], it is possible to observe the chiral anomaly of a single Weyl cone in superconducting Weyl semimetals. The argument from [15] is the following. A pair of Weyl cones at momenta $\pm\mathbf{k}_0$ is described by the second-quantized Hamiltonian

$$\mathcal{H} = \frac{1}{2} \hbar v_F \sum_{\mathbf{k}} \left[\psi_{\mathbf{k}}^\dagger \boldsymbol{\sigma} \cdot (\mathbf{k} - \mathbf{k}_0) \psi_{\mathbf{k}} - \phi_{\mathbf{k}}^\dagger \boldsymbol{\sigma} \cdot (\mathbf{k} + \mathbf{k}_0) \phi_{\mathbf{k}} \right], \quad (1.30)$$

where $\boldsymbol{\sigma}$ is the vector of Pauli matrices acting on the spinors ψ and ϕ , which describe Weyl Fermions of opposite chiralities from the two Weyl nodes. If we imagine that \mathcal{H} is a Hamiltonian describing a superconductor with singlet zero-momentum Cooper pairs, particle-hole symmetry requires that the electron and hole spinors of opposite chiralities are related as $\phi_{\mathbf{k}} = \sigma_y \psi_{-\mathbf{k}}^\dagger$. Using the identity $\sigma_y \sigma_\alpha \sigma_y = -\sigma_\alpha^*$ and also the anticommutator $\psi \sigma_\alpha^* \psi^\dagger + \psi^\dagger \sigma_\alpha \psi = 0$ Eq. (1.30) can then be rewritten in terms of the spinors of a single chirality

$$\begin{aligned} \mathcal{H} &= \frac{1}{2} \hbar v_F \sum_{\mathbf{k}} \left[\psi_{\mathbf{k}}^\dagger \boldsymbol{\sigma} \cdot (\mathbf{k} - \mathbf{k}_0) \psi_{\mathbf{k}} - \psi_{-\mathbf{k}}^\dagger \boldsymbol{\sigma} \cdot (\mathbf{k} + \mathbf{k}_0) \psi_{-\mathbf{k}} \right] \\ &= \hbar v_F \sum_{\mathbf{k}} \psi_{\mathbf{k}}^\dagger \boldsymbol{\sigma} \cdot (\mathbf{k} - \mathbf{k}_0) \psi_{\mathbf{k}}. \end{aligned} \quad (1.31)$$

Now, a magnetic field $\mathbf{B} = \nabla \times \mathbf{A}$ is applied by introducing a vector potential \mathbf{A} via the transformation $\mathbf{k} \rightarrow \mathbf{k} - e\mathbf{A}$. This produces a flux bias in the superconductor and the zeroth Landau level will carry an unbalanced chiral current. This is the chiral anomaly of a single Weyl cone, as previously explained. It is enabled by the asymmetric action of a flux-biased superconductor that gaps out all but one of the particle-hole conjugate pairs of Weyl nodes. In their work [15], O'Brien et al. go on to find that the sign of the flux bias controls which node carries the unbalanced chiral current.

In our research this idea of an asymmetry between the two Weyl nodes in momentum space due to the chiral magnetic effect is transferred to real space in the asymmetric heterostructure consisting of a finite-width Weyl-semimetal slab sandwiched in between the vacuum and a superconductor. This is the geometry studied in detail in chapter 4. In the following some important background information on

the interface between a normal-conducting Weyl semimetal and a superconductor will be discussed.

1.3.1 Interfaces between Weyl semimetals and superconductors

When a normal-conducting region N is placed next to a superconductor S with spin-singlet s -wave pairing forming an NS-type heterostructure, electrons can backscatter from the superconductor and are converted into holes by so called Andreev reflection [18], transferring a Cooper pair to the superconductor, see Fig. 1.7. If

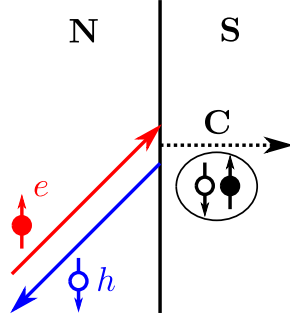


Figure 1.7: At the interface of a normal conductor (N) with a superconductor (S) and incoming electron (in red) can be backscattered as a hole (in blue), transferring a Cooper pair (C) to the superconductor. This process is called Andreev reflection.

the N region is a Weyl semimetal with broken time-reversal symmetry and the superconductor has even-parity spin-singlet pairing, as is the case in our system, this Andreev scattering process is suppressed by the “chirality blockade” [17] which exists because the requirements of the Cooper pair having zero spin and momentum are incompatible with each other for scalar s -wave superconducting pairing. If the superconductor is a multi-orbital superconductor with odd parity, the chirality blockade may be lifted. This situation was discussed in our previous work, Ref. [32].

To better understand the mechanism of this chirality blockade we will now follow the discussion by Bovenzi et al. [17] to show how it is connected to inversion-symmetry breaking. Consider the Hamiltonian of a single Weyl node at momentum $\mathbf{k} = \{0, 0, K\}^T$,

$$H_+ = v_x k_x \sigma_x + v_y k_y \sigma_y + v_z (k_z - K) \sigma_z, \quad (1.32)$$

where the Pauli matrices σ_i refer to spin and with velocities v_i , $i = x, y, z$. As defined previously, its chirality is $C = \text{sign}(v_x v_y v_z)$. For the Weyl node of opposite chirality at momentum $\mathbf{k} = \{0, 0, -K\}$ there are two options

$$H_- = -v_x k_x \sigma_x - v_y k_y \sigma_y - v_z (k_z + K) \sigma_z, \quad (1.33)$$

$$H'_- = +v_x k_x \sigma_x + v_y k_y \sigma_y - v_z (k_z + K) \sigma_z, \quad (1.34)$$

or a different permutation of the signs of the velocities, as long as either all three signs of the velocities (H_-) or only a single sign (H'_-) flips [17]. As we can see, only the first option where all three signs flip satisfies inversion symmetry, $H_-(-\mathbf{k}) = H_+(\mathbf{k})$, whereas the second one does not. The spin texture for the pairs of Weyl cones $H_W = \{H_+, H_-\}$ and $H_W = \{H_+, H'_-\}$ at the Fermi energy is shown in Fig. 1.8 and as we can see, only for the case of broken inversion symmetry do two states at opposite momenta also have opposite spin, as it is required by a scalar zero-momentum spin-singlet superconducting pairing. Therefore, breaking inversion symmetry can remove the chirality blockade and enable Andreev reflection. To see

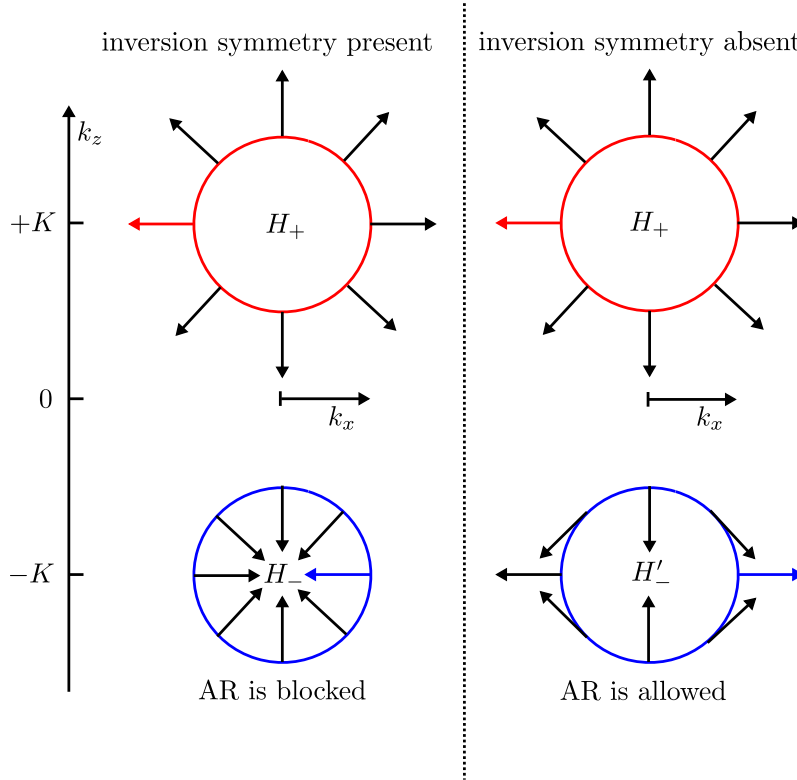


Figure 1.8: Spin-momentum locking for states at the Fermi energy for a pair of Weyl cones at momenta $\mathbf{k} = \{0, 0, \pm K\}^T$. The arrows indicate the spin-polarization direction as a function of k_x and k_z for states with $k_y = 0$. On the left/right-hand side inversion symmetry is present/absent, respectively. It can be seen that zero-momentum spin-singlet pairing, and thus Andreev reflection (AR), is only possible if inversion symmetry is absent: Only then do the red and blue arrows point in opposite direction as is required by the zero-momentum spin-singlet superconducting pairing. Figure adapted from Ref. [17].

how an inversion-symmetry breaking pseudo-scalar superconducting pair potential can also circumvent the chirality blockade we follow Ref. [17] and start from a multilayered heterostructure consisting of alternating layers of topological insulators

with magnetic doping (such as Bi_2Se_3) and normal insulators [33] as shown in Fig. 1.9. This model is very similar to the one studied later on in chapter 4. The

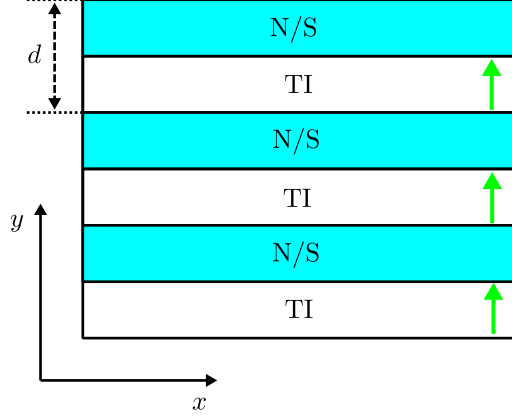


Figure 1.9: Cross section of the layered Weyl-semimetal/superconductor model used in Ref. [17], based on the model from [33]. It consists of alternating topological insulator (TI) and normal-conducting (N) or superconducting (S) spacer layers separated by d . Depending on the spacer layer (N/S) this model describes either a normal-conducting or superconducting Weyl semimetal. The τ degree of freedom of the model refers to the top and bottom surfaces of the TI layers. The magnetization of the TI layers is indicated by the green arrows. Figure adapted from Ref. [17].

four-band Hamiltonian is

$$H(\mathbf{k}) = v_F \tau_z (\sigma_x k_y - \sigma_y k_x) + \beta \tau_0 \sigma_z + (m_k \tau_x - \tau_y t_z \sin k_z d) \sigma_0, \quad (1.35)$$

$$m_k = t'_z + t_z \cos k_z d, \quad (1.36)$$

where d is the distance between TI layers and the Pauli matrices σ_i represent the spin of the surface electrons in these layers. The τ_i Pauli matrices distinguish between top and bottom surfaces of the TI layers which are coupled by hoppings within a layer (t'_z) and from one layer to the next (t_z), see Fig. 1.9. β is an exchange splitting produced by magnetic impurities in the TI layers. This Hamiltonian has inversion symmetry represented by τ_x

$$H(\mathbf{k}) = \tau_x H(-\mathbf{k}) \tau_x, \quad (1.37)$$

and it features two Weyl points located at momenta $\mathbf{k} = \{0, 0, \pi/d \pm K\}^T$, where

$$K^2 \approx \frac{\beta^2 - (t_z - t'_z)^2}{d^2 t_z t'_z}. \quad (1.38)$$

As shown by Meng and Balents [34] this model can be made superconducting by replacing the normal insulators with superconductors, see Fig. 1.9. There are two

possible choices for the symmetry of the superconducting order parameter, labeled “ S ” and “ P ”: A scalar s -wave spin-singlet pairing with Δ_S even under inversion and a pseudo-scalar spin-singlet pairing with Δ_P odd under inversion. The corresponding Bogoliubov-de Gennes (BdG) Hamiltonian \mathcal{H}_α , with $\alpha = S, P$, reads

$$\mathcal{H}_\alpha(\mathbf{k}) = v_F \nu_z \tau_z (\sigma_x k_y - \sigma_y k_x) + \beta \nu_0 \tau_0 \sigma_z + \nu_z (m_k \tau_x - \tau_y t_z \sin k_z d) \sigma_0 - \mu \nu_z \tau_0 \sigma_0 + \mathbf{\Delta}_\alpha, \quad \alpha = S, P, \quad (1.39)$$

$$\mathbf{\Delta}_S = \Delta \nu_x \tau_0 \sigma_0, \quad (1.40)$$

$$\mathbf{\Delta}_P = \Delta \nu_x \tau_z \sigma_0. \quad (1.41)$$

The electron-hole degree of freedom is represented by the ν_i Pauli matrices. To investigate the possibility of Andreev reflection, we perform a unitary transformation of the BdG Hamiltonian defined by

$$\tilde{\mathcal{H}}_\alpha = \tilde{U} \mathcal{H}_\alpha \tilde{U}^\dagger, \quad \mathcal{U} = \begin{pmatrix} \tau_y \sigma_z \Omega_\theta U_0 & 0 \\ 0 & \Omega_\theta U_0 \end{pmatrix}, \quad (1.42)$$

$$\Omega_\theta = \exp\left(-\frac{i}{2} \theta \tau_y \sigma_z\right), \quad U_0 = \exp\left[-i \frac{\pi}{4} (\tau_0 + \tau_x) \sigma_z\right], \quad (1.43)$$

with the angle θ given by

$$\cos \theta = (t_z \sin k_z d) / M_k, \quad \sin \theta = m_k / M_k, \quad (1.44)$$

$$M_k = \sqrt{m_k^2 + t_z^2 \sin^2 k_z d}. \quad (1.45)$$

The transformation shown in Eq. (1.42) does not mix the particle and hole blocks, as it is diagonal in the particle-hole degree of freedom. Assuming that the Weyl points are close together, i.e. when $|t_z - t'_z| \ll \beta \ll t_z d$, the angle θ may be approximated as $\sin \theta \approx 0$ and $|\cos \theta| \approx 1$. Performing this transformation gives

$$\tilde{\mathcal{H}}_\alpha(\mathbf{k}) = v_F \nu_z \tau_z (\sigma_x k_x + \sigma_y k_y) + M_k \nu_0 \tau_z \sigma_z + \beta \nu_0 \tau_0 \sigma_z - \mu \nu_z \tau_0 \sigma_0 + \tilde{\mathbf{\Delta}}_\alpha, \quad \alpha = S, P, \quad (1.46)$$

$$\tilde{\mathbf{\Delta}}_S = \Delta \nu_x \tau_y \sigma_z, \quad (1.47)$$

$$\tilde{\mathbf{\Delta}}_P = -\Delta \nu_x \tau_0 \sigma_0, \quad (1.48)$$

with the two transformed superconducting pairings $\tilde{\mathbf{\Delta}}_S$ and $\tilde{\mathbf{\Delta}}_P$. It is apparent that only the pseudo-scalar pair potential $\tilde{\mathbf{\Delta}}_P$ leads to a transformed Hamiltonian $\tilde{\mathcal{H}}_P$ block-diagonal in τ and thus does not feature the chirality blockade. For the scalar pair potential Andreev reflection remains blocked as explained above, see Fig. 1.8. This explains why in our previous work [32] did not feature the chirality blockade, as the model used there is essentially the same as the block-diagonalized Hamiltonian with a pseudo-scalar pair potential $\tilde{\mathcal{H}}_P$ as shown in Eq. (1.48).

In our research shown in chapter 4 we find a surface equilibrium current flowing parallel to the Weyl semimetal-superconductor interface in our heterostructure which results from the subtle interplay of the topological and trivial bands of the Weyl semimetal. We interpret this current as a signature of the chiral magnetic effect mentioned previously in this chapter. The chirality blockade explains why the bulk of the Weyl semimetal is mostly unaffected by the superconductor: As will be shown in chapter 4 the equilibrium current flows along the edge rather than through the bulk of the Weyl semimetal.

1.3.2 Disordered Weyl semimetals

Since the research in chapter 2 concerns a comparison of the effect of potential disorder on the density of states of disordered graphene (see the introduction in chapter 1.2) and of Weyl semimetals, a discussion of the effect of potential disorder on the density of states of Weyl nodes is necessary. In $3d$ noninteracting disordered electronic systems it is known that as disorder is increased past a critical value the electronic states at the Fermi energy become localized. This is the famous Anderson localization transition [35] between metallic and insulating phases. However, under certain conditions materials that have nodal points close to the Fermi energy in their bandstructure can feature a novel type of non-Anderson transition [12] from a semimetallic to a metallic phase. Here, the density of states at the nodal point is initially zero in the semimetallic phase up to a critical disorder strength and then becomes finite. This is in great contrast to the ordinary Anderson transition for which the density of states has no such feature when the disorder strength passes through its critical value. It remains an unresolved issue though whether this non-Anderson transition is a true quantum phase transition or not [12]. This transition takes place in $3d$ Weyl semimetals [12] but there still remain many open questions: While in Ref. [36] a high-precision numerical analysis of the conductance around the critical disorder strength provides strong evidence that it is indeed a true quantum phase transition, Ref. [12] argues that more research is required, e.g. studying more general types of disorder, and also taking into account rare-region effects. The consequences of these rare-region effects on the density of states of disordered Weyl semimetals remain unclear. In Refs. [37, 38, 39] evidence is provided that nonperturbative effects from rare regions give rise to a nonzero density of states for any nonzero disorder and thus there is no quantum phase transition between semimetallic and metallic phases. On the other hand, Refs. [40, 41] argue that even if these rare-region effects are taken into account the Weyl nodes remain intact since the contributions of the rare-region effects to the density of states at zero energy vanish and thus the density of states does remain zero up to the critical disorder strength where it undergoes the aforementioned quantum phase transition. As we

will see, the high-precision numerical KPM results we have obtained in chapter 2 also support the existence of this quantum phase transition but cannot fully resolve this open question.

2 Calculation of the density of states of disordered nodal points in $d = 2$ and $d = 3$

In this chapter the contributions by the author that led to the publication of the article [42] will be detailed.

2.1 Introduction

Two dimensional graphene [43] and three dimensional Weyl materials [44] are important examples of Dirac-type semimetals. Their electronic structure features a nodal degeneracy point where two linearly dispersing Bloch bands meet. Due to the vanishing density of states (DOS), disorder effects can be expected to be particularly pronounced in these materials and have been actively studied, for reviews see Refs. [2, 12]. Despite all this effort on the disorder problem for nodal points, analytical results, even for a quantity as simple as the DOS, are at best qualitatively correct but fail widely in their quantitative predictions, even for weak disorder. This is surprising insofar as exact answers can be obtained with ease from numerical simulations of non-interacting lattice Hamiltonians. The aim of this chapter is to efficiently calculate the DOS of both two and three dimensional disordered Dirac semimetals on a lattice numerically, using the Kernel Polynomial Method (KPM), and to compare the results with what is obtained analytically from first- and second-order self-consistent perturbation theory, called SCBA (self-consistent Born approximation) and SCPT2, respectively.

To this end, we first describe the models used in chapter 2.2 and how the KPM is used to numerically obtain the DOS for our lattice models in chapter 2.3. In chapter 2.4 we show how disorder is modeled, and in chapter 2.5 how self-consistent perturbation theory is applied to obtain results for a comparison with the numerical data from the KPM that is presented in chapter 2.6. We conclude in chapter 2.7.

2.2 Setup

We consider the minimal continuum model of a single disordered node in $d = 2, 3$ dimensions,

$$H_d = H_{0,d} + U_d, \quad (2.1)$$

where

$$H_{0,2} = \hbar v(\sigma_x k_x + \sigma_y k_y), \quad (2.2)$$

is a $d=2$ Dirac Hamiltonian and

$$H_{0,3} = \hbar v(\sigma_x k_x + \sigma_y k_y + \sigma_z k_z), \quad (2.3)$$

a $d = 3$ Weyl Hamiltonian written with the standard Pauli matrices $\sigma_{i=x,y,z}$. The disorder potential $U_d(\mathbf{r})$, taken to be proportional to the unit matrix, is commonly assumed to have Gaussian correlations and zero mean. In chapter 2.4 we will show how such correlated disorder is generated. Explicitly, we assume a smooth form of the correlator

$$\mathcal{K}_d(\mathbf{r} - \mathbf{r}') = \langle U_d(\mathbf{r})U_d(\mathbf{r}') \rangle = K \frac{(\hbar v)^2}{(2\pi)^{d/2} \xi^2} e^{-|\mathbf{r}-\mathbf{r}'|^2/2\xi^2}, \quad (2.4)$$

where $\langle \dots \rangle$ denotes the disorder average. As $H_{0,d}$ is lacking any scale, the disorder correlation length ξ serves as the fundamental scale in the problem. The dimensionless parameter K measures the disorder strength. In the Brillouin zone of real materials, nodal points usually come in pairs. This is enforced by symmetry (graphene) or topology (Weyl). However, these pairs can have a sizable k-space separation Δk . If $\xi \Delta k \gg 1$ the intra-node scattering dominates over inter-node scattering and the model (2.1) is a reasonable low-energy approximation for realistic materials.

While Eq. (2.1) with the correlator shown in Eq. (2.4) has the advantage that it can be easily approximated in tight-binding models if $\xi \gg a$ (a being the lattice scale) another common choice for \mathcal{K}_d more convenient for analytical calculations is the white noise limit $\xi \rightarrow 0$,

$$\mathcal{K}_d^{GWN}(\mathbf{r}) = K(\hbar v)^2 \xi^{d-2} \delta(\mathbf{r}), \quad (2.5)$$

along with the prescription that $1/\xi$ serves as an ultraviolet cutoff for the clean dispersion $H_{0,d}$. We will use the white noise approximation to make contact with known results.

The clean nodal Hamiltonian $H_{0,d}$ is approximated as the low energy theory of the following tight-binding models on a square/cubic lattice (with constant a , size L^d)

$$H_{0,d}^L = \frac{\hbar v}{a} \begin{cases} \sigma_x \cos ak_x + \sigma_y \cos ak_y & (d=2), \\ \sigma_x \sin ak_x + \sigma_y \sin ak_y - \sigma_z \cos ak_z & (d=3), \end{cases} \quad (2.6)$$

which feature four/eight nodal points for $d = 2$ and $d = 3$, respectively, with minimal mutual distance $\Delta k = \frac{\pi}{a}$. We apply periodic boundary conditions and add a correlated disorder potential as in Eq. (2.4).

2.3 Density of states from the Kernel Polynomial Method

To gauge the quality of analytical perturbation theory approaches discussed in the remaining chapters, let us start by obtaining numerically exact DOS data for the Dirac and Weyl systems with smooth disorder, described by Eqs. (2.1) and (2.4).

The bulk DOS can be calculated as

$$\nu(E) = -\frac{1}{\pi} \text{Im Tr} \int_{\mathbf{k}} G_{\mathbf{k}}^R(E), \quad (2.7)$$

where $\int_{\mathbf{k}} = (2\pi)^{-d} \int d\mathbf{k}$ and $G_{\mathbf{k}}^R(E)$ is the retarded (matrix-valued) Green function. For the clean Hamiltonian $H_{0,d}$, one has

$$\nu_{0,d}(E) = |E|^{d-1} / (2\pi)^{d-1} (\hbar v)^d, \quad (2.8)$$

vanishing at the degeneracy point. If disorder is thought of as a local chemical potential creating carriers from conduction or valence bands, a finite $\nu_d(E=0)$ can be expected (since disorder is a self-averaging quantity, we omit $\langle \dots \rangle$). In the following, we distinguish between the “numerical” approach discussed in this chapter based on explicit generation of a large number of random disorder realizations $U_d(\mathbf{r})$ in Eq. (2.1), and “analytical” methods (perturbation theory) starting from Eq. (2.4), which are discussed in the chapter 2.5.

Starting point is a system of finite size in two or three dimensions with correlated potential disorder, represented as a tight-binding matrix, see Eq. (2.6). The spectral density of said matrix corresponds to the DOS that we want to calculate. The Kernel Polynomial Method (KPM) developed by Weiße et al. in [45] gives us the tools to efficiently calculate the DOS of such a large tight-binding Hamiltonian matrix numerically. We will now give a brief overview of how the DOS is calculated using this method, taken from [45]. See the original work by Weiße et al. [45] for more technical details.

First, the tight-binding Hamiltonian matrix must be rescaled such that its eigenvalues lie inside the interval $[-1, 1]$. Since this matrix contains mostly zeros it can be represented as a sparse matrix, speeding up the calculations. The DOS $\nu(E)$ as a function of energy E is expanded in Chebyshev polynomials and the expansion coefficients $\mu^{(n)}$ are expressed as a trace over a polynomial in H . Using recursion properties of Chebyshev polynomials, the $\mu^{(n)}$ can be efficiently computed (up to order N , usually several thousand) involving only sparse matrix-vector products and a stochastic evaluation of the trace, which can be shown to converge using only a few random vectors (a number of the order 10 can already be enough). Additionally, the Gibbs oscillations present in the DOS are smoothed using the Jackson Kernel. A final undoing of the previous rescaling of the Hamiltonian gives the desired result.

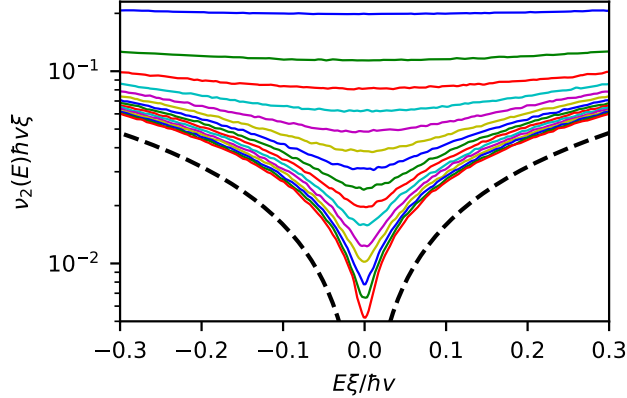


Figure 2.1: Density of states ν_2 for a two-dimensional disordered Dirac node as a function of energy E as calculated by the KPM for various values of the disorder strength K . The colored lines from top to bottom correspond to the green dots shown in Fig. 2.6 from left to right for $1/K = 0.1, 0.2, \dots, 1.5$. The dashed line denotes the analytic result for the clean case, Eq. (2.8). The parameters for the KPM simulation are $\xi = 3a$ (except for the two largest K , where $\xi = 4a$), linear system size $L = 2000\xi$, 20 random vectors for calculating the trace and an expansion order of up to 15000 moments. The data represents an average over 20 disorder realizations and is normalized to a single node.

The DOS results obtained from the KPM are shown in Fig. 2.1 for the two dimensional case (graphene) and in Fig. 2.2 (Weyl semimetal) for several values of the disorder strength K . If our disordered lattice model would faithfully emulate the continuum Hamiltonian (2.1), the DOS at zero energy must be of the scaling form $\nu_d(E = 0) = (\hbar v)^{-1} \xi^{1-d} f(K)$ with $f(K)$ a dimensionless function. We have checked that the KPM data based on the lattice Hamiltonian Eq. (2.6) fulfills this scaling condition once $\xi \gg a$ so that (i) the smooth disorder correlations are well represented on the discrete lattice, (ii) the disorder-induced energy scale is well below the scale of order $\hbar v/a$ where $H_{0,d}^L$ deviates from $H_{0,d}$ and (iii) the inter-node scattering rate is sufficiently suppressed compared to the intra-node rate (the factor is $\exp[-(\Delta k)^2 \xi^2 / 2]$). Moreover, we require $L \gg \xi$ to suppress finite-size effects. Thus, the KPM data (normalized to a single node) shown as dots in Fig. 2.6 ($d = 2$) and Fig. 2.7 ($d = 3$) can be regarded as the exact zero energy DOS of the continuum model Eq. (2.1). Simulation parameters are given in the figure captions. In spite of the abundant literature on similar numerical studies for the DOS of disordered 2d Dirac (see Refs. [46, 47, 48, 49]) and 3d Weyl systems (see Refs. [50, 51, 52]), we are not aware of existing high-precision data obtained for a smooth disorder correlator and with the required scaling properties fulfilled.

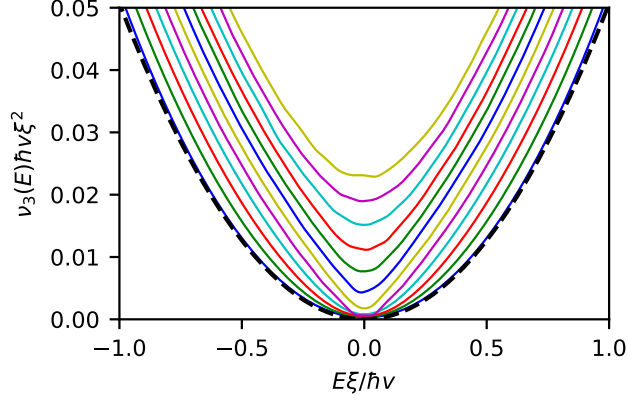


Figure 2.2: Density of states ν_3 for a three-dimensional disordered Weyl node as a function of energy E as calculated by the KPM for disorder strengths $K = 0, 1, 2, \dots, 11$ (bottom to top), corresponding to the green dots shown in Fig. 2.7 (left to right). The dashed line denotes the analytic result for the clean case, Eq. (2.8). The parameters for the KPM simulation are $\xi = 4a$, linear system size $L = 180\xi$, 20 random vectors for calculating the trace and an expansion order of up to 2000 moments. The data represents an average over 40 disorder realizations and is normalized to a single node.

2.4 Generating correlated disorder realizations

Before we discuss perturbation theory and compare our results we will now briefly discuss how the correlated disorder realizations $U_d\mathbf{r}$ are generated. In order to

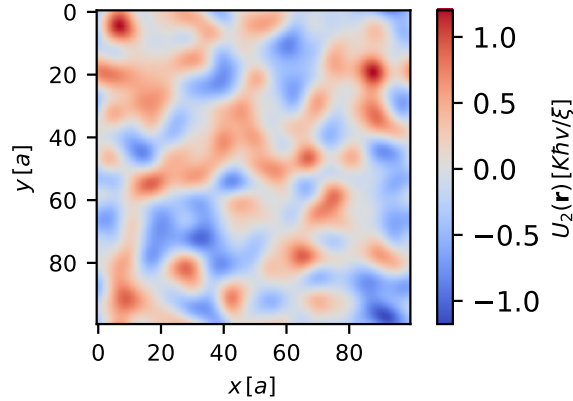


Figure 2.3: Example of a disorder realization $U_2(\mathbf{r})$ in two dimensions with the parameters $\xi = 5a$, $L = 100a$ and $K = 1$.

obtain disorder realizations that are correlated as in Eq. (2.4), we start by generating

disorder realizations $\bar{U}_d(\mathbf{q})$ in momentum space

$$\bar{U}_d(\mathbf{q}) = \frac{\hbar v \sqrt{K}}{\sqrt{2L^d}} \xi^{(d-2)/2} R_{\mathbf{q}} e^{-\mathbf{q}^2 \xi^2/4}, \quad (2.9)$$

$$R_{\mathbf{q}} = b_{\mathbf{q}} + i c_{\mathbf{q}}, \quad (2.10)$$

where the $b_{\mathbf{q}}$ and $c_{\mathbf{q}}$ are drawn from a normal distribution of width σ ($\sigma = 1$ throughout). The $R_{\mathbf{q}}$ are constrained by the requirement that we want $U_d(\mathbf{r})$ to be real, i.e. $R_{\mathbf{q}} = R_{-\mathbf{q}}^*$, and also by periodic boundary conditions. The value $R_{\mathbf{q}=\mathbf{0}}$ is set to zero, as $\bar{U}_d(\mathbf{q} = \mathbf{0})$ corresponds to a uniform offset to $U_d(\mathbf{r})$. The disorder realization in real space $U_d(\mathbf{r})$ is then obtained by discrete Fourier transformation of $\bar{U}_d(\mathbf{q})$. Figure 2.3 shows one such realization in two dimensions.

This disorder model thus generates smooth potential landscapes, as would be by depositing charged impurities or the presence of defects on a (two-dimensional, in the example shown) sample. Averaging the correlators of many such disorder realizations matches the correlation function given in Eq. (2.4), see Fig. 2.4.

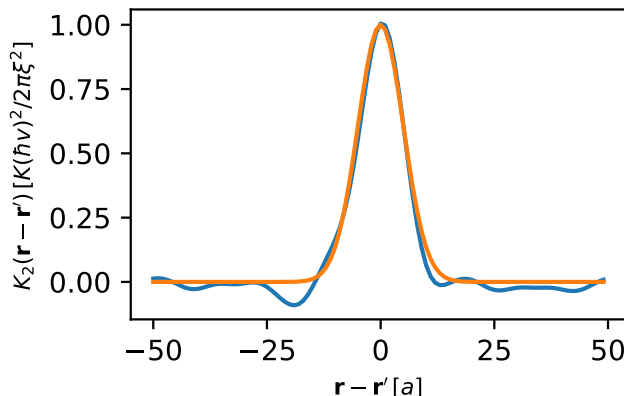


Figure 2.4: Exact correlator from Eq. (2.4) in orange for $\xi = 5a$, $L = 100a$, plotted along the x direction for $\mathbf{r} = \{x, y\}^T$ and $\mathbf{r}' = \{x_0, y\}^T$, at fixed y -coordinate, where $y = x_0 = 50a$. The numerical correlator in blue has been averaged over 400 disorder realizations $U_2(\mathbf{r})$.

2.5 Self-consistent perturbation theory

For the purpose of comparison with the numerical data, which can be considered exact, we calculate the DOS from self-consistent perturbation theory up to order K^2 . The diagrammatic expansion [53] of the self-energy Σ is shown in Fig. 2.5. This

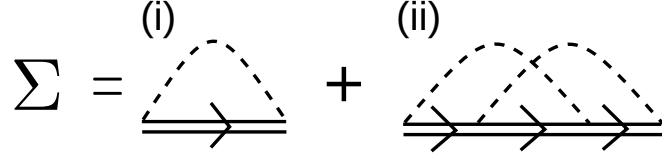


Figure 2.5: Diagrammatic representation of the self-consistency equation (2.11) for the disorder induced self-energy Σ as obtained from perturbation theory. Diagram (i) is the first order term equivalent to SCBA while (ii) is of second order in K . Taking both diagrams together corresponds to SCPT2. Dashed lines denote disorder correlators and double lines self-energy dressed Green functions.

expansion is a self-consistency equation (the dressed Green function depends on Σ) for Σ and reads

$$\begin{aligned} \Sigma(\mathbf{k}) &= K(\hbar v)^2 \int_{\mathbf{q}} G(\mathbf{q}) e^{-\frac{1}{2}\xi^2|\mathbf{q}-\mathbf{k}|^2} \\ &+ K^2(\hbar v)^4 \int_{\mathbf{q}, \mathbf{p}} e^{-\frac{1}{2}\xi^2(|\mathbf{k}-\mathbf{p}|^2+|\mathbf{q}-\mathbf{p}|^2)} G(\mathbf{p}) \cdot G(\mathbf{q}) \cdot G(\mathbf{k} + \mathbf{q} - \mathbf{p}). \end{aligned} \quad (2.11)$$

It is displayed in Fig. 2.5 diagrammatically: The term of order K represents the SCBA, c.f. diagram (i), the second order term is shown in diagram (ii). Taking diagrams (i) and (ii) together corresponds to SCPT2.

To solve Eq. (2.11), we parametrize the self-energy using polar ($d=2$) or spherical ($d=3$) coordinates and proceed by iteration. We compute the DOS from Eq. (2.7).

We use dimensionless units (measuring momenta in $1/\xi$ and energies in $\hbar v/\xi$) and the dimensionless self-energy in $d=2$ (at the nodal point) can be parametrized as

$$\frac{\Sigma_{d=2}(\mathbf{x} = \mathbf{k}\xi)}{\hbar v/\xi} = m_2(x) \{ \sigma_x \cos[\phi] + \sigma_y \sin[\phi] \} + iM_2(x), \quad (2.12)$$

with x, ϕ polar coordinates. The term $M_2(x)$ has to be purely real (to avoid a spontaneous creation of chemical potential) and > 0 for the retarded self energy. As a result, on the rhs of Eq. (2.11), we can chose \mathbf{k} in say, the k_x direction and also take only the σ_x component of the product of Green functions (it can be checked that all other components vanish). The final self-consistency loop is then only for the functions $m_2(x)$ and $M_2(x)$, which turn out to be rather smooth. They can be discretized on a geometric grid for the variable x , the angular integrations can be done using a linearly-spaced integration grid for the angles. We made sure that our results are converged with respect to the resolution of the discretization grids. Once m_2, M_2 do not change any more under insertion on the rhs of Eq. (2.11), the DOS is computed from Eq. (2.7) using interpolation of the integrand and quadrature integration. Likewise, in $d=3$, the same strategy is applied using a parametrization

in spherical coordinates x, ϕ, θ :

$$\frac{\Sigma_{d=3}(\mathbf{x} = \mathbf{k}\xi)}{\hbar v/\xi} = m_3(x) (\sin[\theta] \{\sigma_x \cos[\phi] + \sigma_y \sin[\phi]\} + \sigma_z \cos[\theta]) + iM_3(x). \quad (2.13)$$

2.6 Comparison of results

We proceed by discussing existing analytical approaches to the disorder problem in the $d = 2$ Dirac case. The self-consistent Born approximation (SCBA) determines

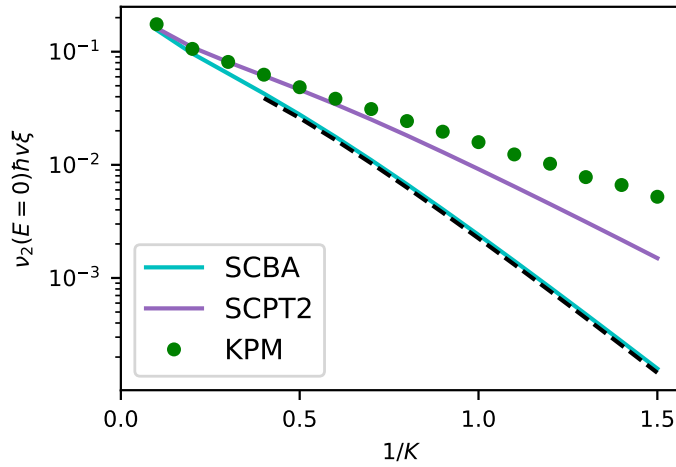


Figure 2.6: The zero energy density of states $\nu_2(E = 0)$ from KPM (dots) compared to the SCBA (blue line) and SCPT2 (purple line). The parameters for the KPM simulation are the same as in Fig. 2.1. The dashed line denote fits to the white noise forms of the density of states from SCBA, see Eq. (2.14).

the disorder induced self-energy $\Sigma \equiv G^{-1} - G_0^{-1}$ (where G_0 is the Green function of the clean system) according to the diagram (i) in Fig. 2.5 [54, 55, 56]. The corresponding self-consistent equation can be solved in closed form for the white noise correlator Eq. (2.5) and yields a disorder induced scale $\Gamma = \frac{\hbar v}{\xi} e^{-2\pi/K}$ (for $K \lesssim 1$) exponentially small in K appearing in the imaginary self-energy $\Sigma = \pm i\Gamma$ and a DOS [55]

$$\nu_2(E = 0) \hbar v \xi \propto e^{-2\pi/K} / K. \quad (2.14)$$

In Fig. 2.6, this result (black-dashed line) compares well to the DOS obtained from the SCBA with smooth disorder correlator from Eq. (2.4) (light-blue line). However, comparing to the exact KPM-DOS in Fig. 2.6 (green dots), we find that albeit the exponential form is correctly predicted by the SCBA, the slope (prefactor

in the exponent) is roughly a factor 2 off. The SCPT2 result (purple line) further improves upon the SCBA with the slope now closer to the exact KPM result.

The failure of the SCBA and SCPT2 can be attributed to interference corrections from multiple disorder scattering events [57], see diagram (ii) in Fig. 2.5 for the lowest order correction to the SCBA (third order in K corrections to SCPT2 are not shown). While unimportant in ordinary metals (where $1/k_{\text{F}}l \ll 1$ with k_{F} Fermi wavevector and l the mean free path serves as a small parameter), for Dirac materials these diagrams provide corrections of order $\ln[\hbar v/\xi\Gamma]$. Accordingly, their contribution vanishes for strong disorder where the SCBA becomes reliable, c.f. Fig. 2.6.

We now turn to the disorder induced DOS for a $d = 3$ Weyl node. Here, weak

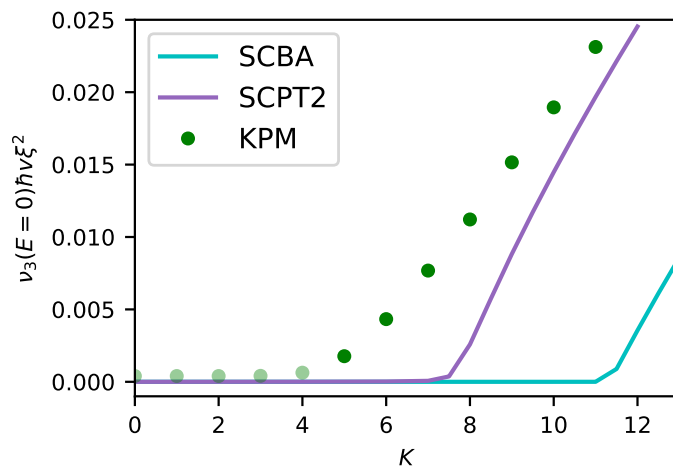


Figure 2.7: The zero energy density of states $\nu_3(E = 0)$ from KPM (dots) compared to the SCBA (blue line) and SCPT2 (purple line). The parameters for the KPM simulation are the same as in Fig. 2.2 The semi-transparent data points for $K \leq 4$ suffer from finite- L effects and overestimate the true bulk DOS.

disorder is irrelevant so that the DOS is maintained at zero. Only for $K > K_c$, disorder induces a finite DOS, see Fig. 2.7 for the KPM data (green dots). These qualitative features were correctly predicted by the SCBA (light blue line, see Refs. [58, 59, 60, 61]). From the KPM, we find $K_c^{KPM} = 4 \pm 0.5$ (the precision is limited by finite-size effects) while $K_c^{SCBA} \simeq 11$ (blue line) is off by more than a factor two. SCPT2 (purple line) improves upon the SCBA result as it should and gives $K_c^{SCPT2} \simeq 7.5$.

2.7 Conclusion

We numerically calculated the DOS of disordered nodal points in two and three dimensions. Comparisons with results from first- and second-order perturbation theory show the correct qualitative behavior but fail to give good quantitative agreement with the exact numerical results. However, our high-precision density of states results from KPM do provide strong evidence in favor of interpreting the transition from semimetallic to metallic phases occurring in Weyl semimetals as a true quantum phase transition, although a final confirmation is yet to be achieved. A nonperturbative approach [62] has recently been developed, improving upon the analytical side of the problem.

The comparisons shown in the above chapters demonstrate the capabilities of the KPM as an efficient numerical tool, see also [45] for further possible applications of this method.

More complicated disorder models, in particular vector disorder in two dimensions and its characteristic $\nu(E)$ behavior or scattering between multiple nodal points, as present in realistic materials, could also be studied in the future.

3 Interference effects induced by a precessing easy-plane magnet coupled to a helical edge state

This chapter consists of the details of the work that led to the publication of the article [63].

3.1 Introduction

Since backscattering of electrons in the helical edge of a two-dimensional topological insulator is forbidden by time-reversal symmetry, breaking time-reversal symmetry by an applied magnetic field or by coupling of the helical edge to the exchange field of a magnet or a magnetic impurity is the only mechanism by which electrons in a helical edge can be backscattered [64, 65, 66, 67, 68, 69]. The purposeful coupling of the helical edge to magnetic insulators has been shown to result in fascinating properties, such as the appearance of Majorana zero modes at the boundary between segments with a magnet-induced gap and with proximity-induced superconductivity [70], various thermoelectric effects [71, 72], or the possibility to convert electrical energy to mechanical motion in an adiabatic quantum motor [73, 21]. Magnetic impurities exchange-coupled to the helical edge states exhibit characteristic Kondo effects [74, 75, 76, 77] and electrically controlled dynamics of the impurity spin due to backscattering of helical edge state electrons [78, 79].

The application of a magnetic field or the exchange coupling of a helical edge to a magnetic insulator opens a gap in the spectrum of the helical edge if the direction of the (exchange) field is not collinear with the spin quantization axis of the helical edge states. In this context, it can be seen as a surprise that an electric current carried by a helical edge is transmitted perfectly across a region coupled to a magnetic insulator, if the magnet has an easy-plane anisotropy with easy plane perpendicular to the quantization axis of the helical edge states [14, 13]. The electrical current flows despite the presence of an excitation gap in the spectrum of the helical edge, in such a way that the electrical current “lost” by the backscattering of electronic quasiparticles at the gapped region is compensated by the flow of a dissipationless spin current carried by the precessing magnetization and facilitated by charge-to-

spin and spin-to-charge conversion at the magnet interface. The charge-to-spin conversion at the magnet interface is perfect because of the helical nature of the edge [80]; the absence of losses for the spin transport through the magnet is a manifestation of “superfluid” spin transport in easy-plane magnets [81, 82, 83, 84, 85, 86]. Since the electrical current is carried by a collective mode of the magnetization, it takes place without shot noise and with strongly suppressed thermal noise at finite frequencies [13]. The coupling of a helical edge to a magnetic insulator has also been proposed as a method for nondissipative current-driven magnetization precession [73, 87].

The perfect compensation of the current backscattered from the magnet-induced gap leaves the open question: How can the presence of the easy-plane magnet be detected, if the current through the edge is not influenced by it? In order to answer this question we theoretically consider an Aharonov-Bohm interferometer [25] consisting of two tunnel-coupled helical edge modes, one of which is covered by an easy-plane magnet like in Refs. [14, 13].

We predict the two main characteristic features: First, we show that this interferometer setup, if subjected to a constant (DC) voltage bias, responds with a time-dependent (AC) current component (in addition to a large DC response), due to the coupling to the precessing magnetization. Depending on system parameters, the AC currents occur at the precession frequency ω_M of the magnet or, additionally, at twice that frequency. For comparison: No AC current response exists in the setup analyzed in Refs. [14, 13]. Second, the Aharonov-Bohm oscillations in the DC current, usually seen as a signature of coherent quasiparticle transport, are exponentially suppressed for small bias voltages and temperatures if the Fermi level is in the magnet-induced gap. The suppression of Aharonov-Bohm oscillations is consistent with the existence of an excitation gap in the spectrum where the helical edge is in contact to the magnet. Despite the absence of a conventional Aharonov-Bohm effect, in our geometry the AC currents can be seen as a manifestation of coherence: They result from the interference of electrons scattered at the tunnel contacts and electrons backscattered from the magnet interface, where they change their energy by the amount $\hbar\omega_M$.

The appearance of AC currents in response to a DC voltage bias is remotely reminiscent of the Josephson effect, where applying a constant voltage bias to a superconducting tunnel junction leads to time-dependent currents [8]. It may be seen as another manifestation of “spin superfluidity” in easy-plane ferromagnets [81, 82, 83, 84, 85, 86].

Electron interferometers with helical edge states, but without exchange coupling to a magnetic insulator, have been investigated theoretically in the literature. The characteristic temperature and interaction-induced dephasing [88] of charge and spin excitations were identified, as well as controllable spin properties [89, 90, 91]. On

the experimental side, quantum point contacts between two helical edge channels have been realized recently in HgTe-based quantum wells and DC transport through the constriction has been measured [92]. The possibility to produce AC currents if these systems are exchange-coupled to magnetic insulators provides a promising novel route for interference-based quantum devices.

This part of the thesis is organized as follows: In chapter 3.2 the interferometer setup is described in detail and the scattering-matrix approach is introduced, extending the method of Ref. [13]. In chapters 3.3, 3.4, and 3.5 we present calculations of the current in response to a DC bias in one of the interferometer arms. Chapter 3.3.1 addresses a simplified setup in which one of the two tunnel contacts is “open”, which has AC currents at frequency ω_M only, but allows all calculations to be performed analytically. This analytical result allows us to elucidate the difference between the DC current pumped through the magnet and the interference AC current created upon reflection from the rotating magnetization vector. Chapter 3.3.2 provides additional details on the interpretation of these results. Chapter 3.4 considers the special case that one of the two tunnel contacts is “closed”, which shows the full phenomenology of AC currents at frequencies ω_M and $2\omega_M$ and still admits a partially analytical treatment. Chapter 3.5 contains our results for an interferometer with a generic choice of parameters. In chapter 3.6 the anomalous temperature dependence of DC Aharonov-Bohm current contributions is discussed. We conclude in chapter 3.7.

3.2 Model

We consider an interferometer built from two opposing helical edge modes of a quantum spin Hall insulator. One of the arms of the interferometer is partially covered by an insulating magnet. Following Refs. [14, 13] we consider a magnet with an easy-plane anisotropy, such that the easy plane is oriented perpendicular to the spin quantization axis of the helical edge mode. Establishing contact between the two edge channels on both sides of the magnet then results in the typical interferometer geometry, see Fig. 3.1. The interferometer is connected to four ideal leads, as shown schematically in the figure.

In practice, such a geometry may be realized by taking the helical edge modes on the two sides of the same quantum spin Hall insulator, see Fig. 3.1 (left). In this case, only part of the insulator is covered by the magnetic insulator. In this geometry, a “point contact” between the two sets of edge modes can be achieved, e.g., by locally reducing the insulator width by lithographic methods or by electrostatic gating of the device. Alternatively, the helical states can be edges of different spin Hall insulators, and contacting the two edge modes is achieved by bringing the edges

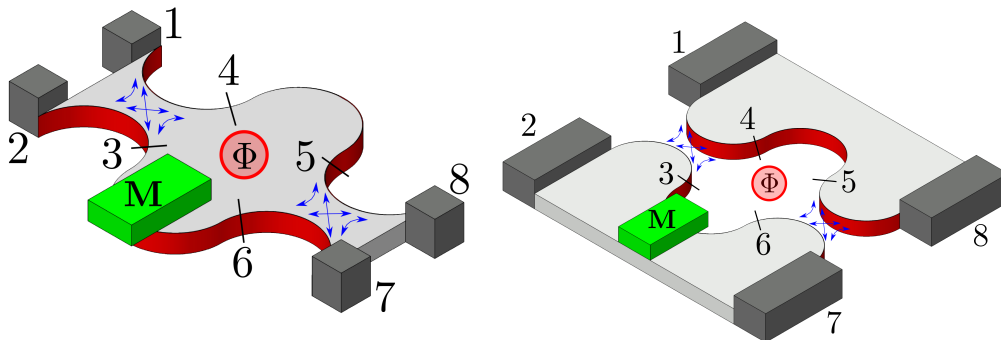


Figure 3.1: Schematic picture of the interferometer considered here. The interferometer can be realized by bringing helical edge channels of the same quantum spin Hall insulator sufficiently close together that they can make electrical contact (left), or by bringing the edge channels of different quantum spin Hall insulators into contact (right). Both panels show the location of eight reference points $i = 1, 2, \dots, 8$ used for the calculations in the main text. The “positive” current direction for $i = 1, 2, 3, 4$ and for $i = 5, 6, 7, 8$ is to the right and to the left, respectively. The interferometer is threaded by a magnetic flux Φ .

close together, see Fig. 3.1 (right).

A magnetic flux Φ is threaded through the area enclosed by the interfering edge modes. Apart from the magnetic flux and the coupling to the magnetic insulator, time reversal symmetry is unbroken, so that backscattering into the same edge mode is forbidden everywhere in the device (except in the vicinity of the magnetic insulator).

The magnet is assumed to be small enough, that it may be described by a single moment \mathbf{M} . We choose the (spin) coordinate axes such, that the easy plane is the xy plane and the quantization axis for the spin in the helical edge mode is the z axis. With this choice, the magnet and its interaction with the helical edge state are described by the second-quantized Hamiltonian [14, 13]

$$\hat{H} = \int dx \hat{\psi}(x)^\dagger [-i\hbar v_F \partial_x \sigma_z + h(x) \boldsymbol{\sigma} \cdot \mathbf{M}] \hat{\psi}(x) + \frac{D}{2} M_z^2, \quad (3.1)$$

where v_F is the Fermi velocity, D the strength of the easy-plane anisotropy, $\sigma_{x,y,z}$ are the Pauli matrices, $h(x)$ is a function that describes the exchange coupling between the magnetic moment \mathbf{M} and the spin of electrons at the helical edge state, and $\hat{\psi}(x) = \{\hat{\psi}_\uparrow(x), \hat{\psi}_\downarrow(x)\}^T$ is a two-component spinor describing electrons in the helical edge. Away from the magnet, the exchange coupling $h(x) \rightarrow 0$. The assumption that the easy plane is perpendicular to the spin quantization axis is generic for a thin magnetic film [93] exchange coupled to the helical edge modes of a quantum spin Hall material, such as a HgTe quantum well [94]. The application of a finite

bias across the magnet causes the magnetization to cant out of the xy plane [14, 13], which sets the magnet in a precessional motion with frequency

$$\omega_M = DM_z. \quad (3.2)$$

We describe coherent transport through the interferometer using scattering theory. To this end, we mark eight reference positions labeled $i = 1, 2, \dots, 8$ in the device, see Fig. 3.1. The reference positions are chosen in close proximity to the point contact region, where scattering between the helical edge states is possible. At each reference position i we consider creation and annihilation operators $\hat{a}_{i,\pm}^\dagger(\varepsilon)$ and $\hat{a}_{i,\pm}(\varepsilon)$ for an electron in a (particle-flux normalized) scattering state at energy ε , moving in the same (+) or opposite (-) direction as the reference arrows in Fig. 3.2. The operators $\hat{a}_{i\pm}(\varepsilon)$ and the corresponding creation operators $\hat{a}_{i\pm}^\dagger(\varepsilon)$ are related to the current $\mathcal{I}_i(\omega)$ at reference position i and at frequency ω as [26, 27]

$$\mathcal{I}_i(\omega) = \frac{e}{h} \int d\varepsilon \left[\overline{\hat{a}_{i+}^\dagger(\varepsilon)\hat{a}_{i+}(\varepsilon + \hbar\omega)} - \overline{\hat{a}_{i-}^\dagger(\varepsilon)\hat{a}_{i-}(\varepsilon + \hbar\omega)} \right]. \quad (3.3)$$

Here, $\overline{\dots}$ denotes the expectation value. Electrons coming in from the four ideal leads (corresponding to the reference positions $i = 1, 2, 7, 8$) are in thermal equilibrium at temperature T_i and chemical potential eV_i ,

$$\overline{\hat{a}_{i+}^\dagger(\varepsilon)\hat{a}_{i+}(\varepsilon')} = f_i(\varepsilon)\delta(\varepsilon - \varepsilon'), \quad i = 1, 2, 7, 8, \quad (3.4)$$

where $f_i(\varepsilon) = [1 + e^{(\varepsilon - eV_i)/k_B T_i}]^{-1}$ is the Fermi-Dirac distribution function.

Scattering is elastic everywhere in the device, except at the magnet, where electrons can absorb or emit an energy quantum $\hbar\omega_M$ upon reflection [13]. Elastic scattering from the two point contact regions is described by 4×4 scattering matrices $S^{(C1)}$ and $S^{(C2)}$. We assume that the point contact regions are small enough that $S^{(C1)}$ and $S^{(C2)}$ may be taken independent of the energy ε ,

$$\begin{aligned} \begin{pmatrix} \hat{a}_{1-}(\varepsilon) \\ \hat{a}_{2-}(\varepsilon) \\ \hat{a}_{3+}(\varepsilon) \\ \hat{a}_{4+}(\varepsilon) \end{pmatrix} &= S^{(C1)} \begin{pmatrix} \hat{a}_{1+}(\varepsilon) \\ \hat{a}_{2+}(\varepsilon) \\ \hat{a}_{3-}(\varepsilon) \\ \hat{a}_{4-}(\varepsilon) \end{pmatrix}, \\ \begin{pmatrix} \hat{a}_{5+}(\varepsilon) \\ \hat{a}_{6+}(\varepsilon) \\ \hat{a}_{7-}(\varepsilon) \\ \hat{a}_{8-}(\varepsilon) \end{pmatrix} &= S^{(C2)} \begin{pmatrix} \hat{a}_{5-}(\varepsilon) \\ \hat{a}_{6-}(\varepsilon) \\ \hat{a}_{7+}(\varepsilon) \\ \hat{a}_{8+}(\varepsilon) \end{pmatrix}. \end{aligned} \quad (3.5)$$

Time-reversal symmetry imposes the antisymmetry constraints

$$S^{(Cj)} = -(S^{(Cj)})^T. \quad (3.6)$$

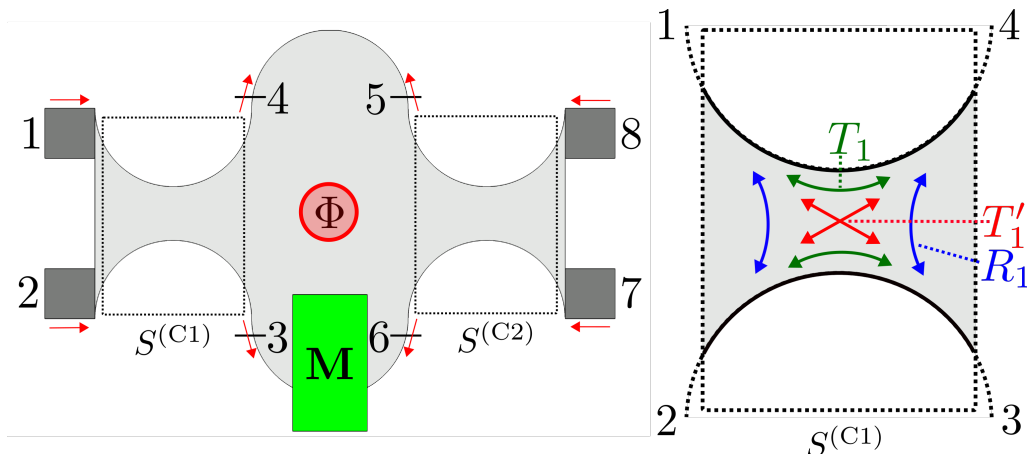


Figure 3.2: In the theoretical description, currents are calculated for eight reference points $i = 1, 2, \dots, 8$, as shown in the left panel. The “positive” current direction for $i = 1, 2, 3, 4$ and for $i = 5, 6, 7, 8$ is to the right and to the left, respectively. The two tunneling point contacts between the opposing helical edge states are described by scattering matrices $S^{(C1)}$ and $S^{(C2)}$. The definitions of the transmission coefficients T_1 and T'_1 and the reflection coefficient R_1 for the left tunneling point contact are shown in the right panel.

Absorbing eventual phase factors in the definitions of the operators $\hat{a}_{i\pm}$, this implies that without loss of generality these matrices can be parametrized as

$$S^{(Cj)} = \begin{pmatrix} 0 & \sqrt{R_j} & -i\sqrt{T'_j} & -\sqrt{T_j} \\ -\sqrt{R_j} & 0 & -\sqrt{T_j} & -i\sqrt{T'_j} \\ i\sqrt{T'_j} & \sqrt{T_j} & 0 & \sqrt{R_j} \\ \sqrt{T_j} & i\sqrt{T'_j} & -\sqrt{R_j} & 0 \end{pmatrix}, \quad (3.7)$$

with $R_j + T_j + T'_j = 1$ and $j = 1, 2$. As can be seen in Fig. 3.2, R_j , T_j and T'_j are the probabilities for reflection via point contact j (changing the edge), transmission along the same edge and transmission through the point contact j (changing the edge), respectively. Note that R_j and T_j describe both spin-conserving processes, whereas the process due to T'_j flips the electron spin. The latter process is possible even if time-reversal symmetry is conserved but needs a breaking of inversion symmetry [95, 96, 97]. Tunable spin-flip processes due to Rashba spin-orbit coupling become possible by an electric field [96, 98, 97] that could be induced locally by gates. We will see in the upcoming chapters that a characteristic AC-part of the current becomes possible due to interference between two scattering paths — one that includes reflection at the magnet, and another that does not. These interference contributions necessarily involve processes with amplitude $\sqrt{T'_j}$.

Since there is no backscattering for propagation along the helical edge, the operators at the two ends of the upper interferometer arm at reference positions “4” and

“5” are simply related by a phase factor,

$$\begin{aligned}\hat{a}_{5-}(\varepsilon) &= e^{ik(\varepsilon)L+i\phi}\hat{a}_{4+}(\varepsilon), \\ \hat{a}_{4-}(\varepsilon) &= e^{ik(\varepsilon)L-i\phi}\hat{a}_{5+}(\varepsilon).\end{aligned}\quad (3.8)$$

Here we have chosen a gauge such that the AB phase shift $\phi = e\Phi/\hbar$ from the magnetic flux Φ is accumulated for the propagation between reference positions “4” and “5”. Further, L is the length of the interferometer arm and $k(\varepsilon) = k_F + \varepsilon/\hbar v_F$, with k_F the Fermi wavenumber and v_F the Fermi velocity. The energy ε is measured with respect to the Fermi level.

Because of the spin-momentum locking in the helical edge modes, a reflection from the magnetic insulator necessarily comes with a spin flip of the edge electrons. As a result, reflection from the magnetic insulator involves an increase or decrease of M_z by one and, hence, the absorption or emission of an energy quantum $\hbar\omega_M$ by the reflected electron [14, 13]. These processes are described by the relation [13]

$$\begin{pmatrix} \hat{a}_{3-}(\varepsilon_-) \\ \hat{a}_{6-}(\varepsilon_+) \end{pmatrix} = S^{(M)}(\varepsilon) \begin{pmatrix} \hat{a}_{3+}(\varepsilon_+) \\ \hat{a}_{6+}(\varepsilon_-) \end{pmatrix}, \quad (3.9)$$

where $\varepsilon_{\pm} = \varepsilon \pm \hbar\omega_M/2$ and the 2×2 matrix $S^{(M)}(\varepsilon)$ reads

$$S^{(M)}(\varepsilon) = \begin{pmatrix} r_M(\varepsilon)\hat{m}_+ & t'_M(\varepsilon) \\ t_M(\varepsilon) & r'_M(\varepsilon)\hat{m}_- \end{pmatrix}. \quad (3.10)$$

Here r_M , r'_M , t_M , and t'_M are reflection and transmission amplitudes with a “frozen” magnetization of the magnet [13], and \hat{m}_{\pm} are ladder operators that change M_z by $\pm\hbar$ normalized as $\hat{m}_-\hat{m}_+ = \mathbb{1}$. The amplitudes r_M , r'_M , t_M , and t'_M also include phase shifts accumulated during the propagation between the point contacts and the insulating magnet. Unitarity gives the conditions $|r_M(\varepsilon)|^2 = |r'_M(\varepsilon)|^2 = 1 - |t_M(\varepsilon)|^2 = 1 - |t'_M(\varepsilon)|^2$. We will assume that $|r_M(\varepsilon)| \rightarrow 0$ for energies ε far above and below the Fermi level. This is consistent with the model of Eq. (3.1), which has $|r_M(\varepsilon)| \rightarrow 0$ for $|\varepsilon| \gg \max_x |h(x)||M|$.

Upon reflection off of the magnet, an electron changes its energy by the amount $\pm\hbar\omega_M$, where the sign of the change is opposite for reflection from the left and from the right, see Eq. (3.9). Since backscattering in the helical channels away from the magnet is forbidden, the difference of the total numbers of reflections of an electron from the left and from the right sides of the magnet cannot be larger than one, so that an electron can not change its energy by more than $\hbar\omega_M$ upon moving through the interferometer.

Taken together, Eqs. (3.5), (3.8), and (3.9) give a set of twelve linear equations, which allow one to express all operators $\hat{a}_{i\pm}$ at the reference positions $i = 1, 2, \dots, 8$ in terms of the four operators \hat{a}_{1+} , \hat{a}_{2+} , \hat{a}_{7+} , and \hat{a}_{8+} describing electrons incident

from the reservoirs. Since the energy ε can not change by more than one discrete quantum $\hbar\omega_M$, the solution of the set of linear equations (3.5), (3.8), and (3.9) can be cast in the form

$$\hat{a}_{j-}(\varepsilon) = \sum_{n=-1}^1 \sum_{k=1,2,7,8} S_{j;k}^{(n)}(\varepsilon) \hat{a}_{k+}(\varepsilon + n\hbar\omega_M), \quad (3.11)$$

where $S_{j;k}^{(n)}(\varepsilon)$ is the “scattering matrix” of the device. Since the current $\mathcal{I}(\omega)$ is bilinear in the creation and annihilation operators, see Eq. (3.3), it then follows that at any position in the device the current $\mathcal{I}_j(\omega)$ can be nonzero for $\omega = 0$, $\omega = \pm\omega_M$, or $\pm 2\omega_M$ only. This allows us to write

$$\mathcal{I}_j(\omega) = \sum_{n=-2}^2 I_j(n\omega_M) \delta(\omega - n\omega_M). \quad (3.12)$$

Higher harmonics than $|n| = 2$ are not possible, as electrons cannot change their energy by more than $\hbar\omega_M$ upon passing through the interferometer device. It follows that the DC current in lead j ($j = 1, 2, 7, 8$) is

$$I_j(0) = \frac{e}{h} \int d\varepsilon \sum_{k=1,2,7,8} \sum_{n=-1}^1 |S_{j;k}^{(n)}(\varepsilon)|^2 [f_j(\varepsilon) - f_k(\varepsilon + n\hbar\omega_M)], \quad (3.13)$$

where we used that $\sum_{k,n} |S_{j;k}^{(n)}(\varepsilon)|^2 = 1$. Similarly, the AC currents at frequency ω_M and $2\omega_M$ read

$$I_j(\omega_M) = -\frac{e}{h} \int d\varepsilon \sum_{k=1,2,7,8} \sum_{n=0}^1 S_{j;k}^{(n)}(\varepsilon)^* S_{j;k}^{(n-1)}(\varepsilon + \hbar\omega_M) f_k(\varepsilon + n\hbar\omega_M), \quad (3.14)$$

$$I_j(2\omega_M) = -\frac{e}{h} \int d\varepsilon \sum_{k=1,2,7,8} S_{j;k}^{(1)}(\varepsilon)^* S_{j;k}^{(-1)}(\varepsilon + 2\hbar\omega_M) f_k(\varepsilon + \hbar\omega_M). \quad (3.15)$$

The steady-state precession frequency ω_M is an unknown in this procedure and must be determined self-consistently using Eq. (3.2) and the steady-state condition

$$\dot{M}_z(t) = 0. \quad (3.16)$$

The net rate of change of M_z is proportional to the net current reflected from the magnet \mathcal{I}_r ¹ [14, 13],

$$\dot{M}_z(t) = \frac{\mathcal{I}_r(t)}{e}. \quad (3.17)$$

¹We do not consider the case that the magnetization precession is driven by a source different from the applied voltage bias, such as an alternating magnetic field. In that case the magnet may function as a “charge pump” even in the absence of an applied bias voltage [80]. We also do neglect the effect of Gilbert damping, although both damping and external driving can be included relatively straightforwardly by adding additional terms to the right-hand side of Eq. (3.17).

The Fourier transform $\mathcal{I}_r(\omega)$ of the current reflected from the magnet is given by

$$\mathcal{I}_r(\omega) = \frac{e}{h} \int d\varepsilon \left[\hat{a}_{3+}^\dagger(\varepsilon_+) \hat{a}_{3+}(\varepsilon_+ + \hbar\omega) - \hat{a}_{6+}^\dagger(\varepsilon_-) \hat{a}_{6+}(\varepsilon_- + \hbar\omega) \right]. \quad (3.18)$$

Electron paths contributing to $\mathcal{I}_r(\omega)$ can differ by at most one reflection from the magnet, so that only Fourier components at $\omega = n\omega_M$ with $n = -1, 0, 1$ contribute to $\mathcal{I}_r(\omega)$,

$$\mathcal{I}_r(\omega) = \sum_{n=-1}^1 I_r(n\omega_M) \delta(\omega - n\omega_M). \quad (3.19)$$

The Fourier components $I_r(n\omega_M)$ depend on the precession frequency ω_M . They can be calculated using the scattering formalism outlined above. The Fourier components $I_r(n\omega_M)$ with $n = \pm 1$ give rise to small oscillations of M_z , which do not affect the precession frequency ω_M for a macroscopic magnet. Keeping the zero-frequency component only, we find that the steady-state condition for M_z , from which the precession frequency ω_M can be determined, reads

$$I_r(0) = 0. \quad (3.20)$$

In the remaining chapters we present explicit analytical and numerical results of this procedure for several representative choices of the scattering matrices $S^{(C1)}$ and $S^{(C2)}$ of the point contact regions.

3.3 Right point contact “open”

3.3.1 Calculation of DC and AC currents

As an analytically tractable geometry, we first consider a setup in which the right point contact in Fig. 3.1 is fully “open”, so that effectively there is a single point contact region only, see Fig. 3.5. In this geometry, electrons incident from reservoirs “1”, “2”, and “8” can only reflect off the left end of the magnet, whereas electrons incident from the reservoir “7” can only reflect off the right end of the magnet. This rules out interference processes with a total energy difference of $2\hbar\omega_M$, so that the only harmonics $I_j(n\omega_M)$ with $n = 0, \pm 1$ need to be considered.

For the scattering matrix $S^{(C2)}$ the condition that the right point contact is “open” implies $R_2 = T'_2 = 0$, so that $\hat{a}_{5\pm}(\varepsilon) = \mp \hat{a}_{8\pm}(\varepsilon)$ and $\hat{a}_{6\pm}(\varepsilon) = \mp \hat{a}_{7\pm}(\varepsilon)$. We can express the remaining operators $\hat{a}_{j\pm}(\varepsilon)$ in terms of the operators $\hat{a}_{1+}(\varepsilon)$, $\hat{a}_{2+}(\varepsilon)$, $\hat{a}_{7+}(\varepsilon)$, and $\hat{a}_{8+}(\varepsilon)$ describing electrons coming in from the reservoirs by solving Eqs. (3.5) and (3.9) for this case.

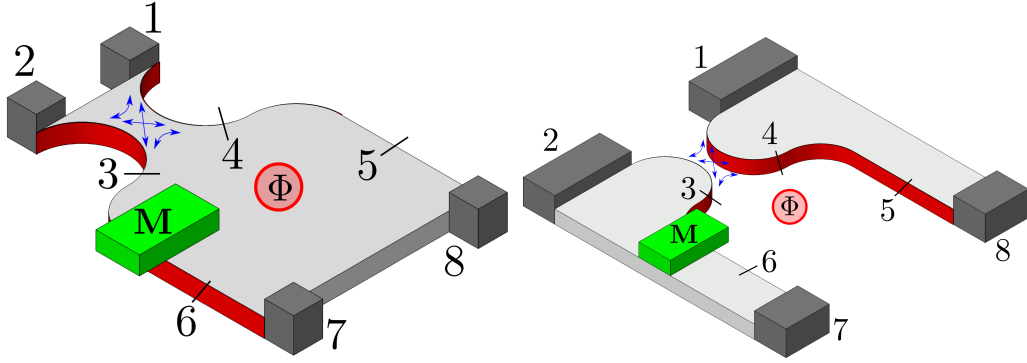


Figure 3.3: Schematic picture of the “right point contact open” geometry for a realization in which the interfering edge channels are on the same quantum spin Hall insulator (left) and on different quantum spin Hall insulators (right). The positions labeled $i = 1, 2, \dots, 8$ refer to the reference positions used for the calculations in the main text.

We first calculate the operators $\hat{a}_{3+}(\varepsilon)$ and $\hat{a}_{6+}(\varepsilon)$ describing electrons incident on the magnet, because these determine the precession frequency ω_M ,

$$\hat{a}_{3+}(\varepsilon) = i\hat{a}_{1+}(\varepsilon)\sqrt{T_1'} + \hat{a}_{2+}(\varepsilon)\sqrt{T_1} - \hat{a}_{8+}(\varepsilon)\sqrt{R_1}e^{ik(\varepsilon)L-i\phi}, \quad (3.21)$$

$$\hat{a}_{6+}(\varepsilon) = -\hat{a}_{7+}(\varepsilon). \quad (3.22)$$

The steady-state precession frequency ω_M can be calculated from Eq. (3.20) upon setting $\dot{M}_z = 0$,

$$0 = \int d\varepsilon |r_M(\varepsilon)|^2 [f_{3+}(\varepsilon_+) - f_7(\varepsilon_-)], \quad (3.23)$$

where we abbreviated

$$f_{3+}(\varepsilon) = R_1 f_8(\varepsilon) + T_1 f_2(\varepsilon) + T_1' f_1(\varepsilon). \quad (3.24)$$

The results for the operators $\hat{a}_{j-}(\varepsilon)$ in the leads ($j = 1, 2, 7, 8$) are then expressed

in terms of the matrices of coefficients $S_{j;k}^{(n)}(\varepsilon)$, see Eq. (3.11), which read

$$S^{(-)}(\varepsilon) = r_M(\varepsilon_-)\hat{m}_- \begin{pmatrix} 0 & 0 & 0 & 0 \\ 0 & 0 & 0 & 0 \\ 0 & 0 & -1 & 0 \\ 0 & 0 & 0 & 0 \end{pmatrix},$$

$$S^{(0)}(\varepsilon) = \begin{pmatrix} 0 & \sqrt{R_1} & it'_M(\varepsilon_+)\sqrt{T'_1} & e^{ikL-i\phi}\sqrt{T_1} \\ -\sqrt{R_1} & 0 & t'_M(\varepsilon_+)\sqrt{T_1} & ie^{ikL-i\phi}\sqrt{T'_1} \\ it_M(\varepsilon_-)\sqrt{T'_1} & t_M(\varepsilon_-)\sqrt{T_1} & 0 & t_M(\varepsilon_-)e^{ikL-i\phi}\sqrt{R_1} \\ e^{ikL+i\phi}\sqrt{T_1} & ie^{ikL+i\phi}\sqrt{T'_1} & -t'_M(\varepsilon_+)e^{ikL+i\phi}\sqrt{R_1} & 0 \end{pmatrix}, \quad (3.25)$$

$$S^{(+)}(\varepsilon) = r_M(\varepsilon_+)\hat{m}_+ \begin{pmatrix} T'_1 & -i\sqrt{T_1T'_1} & 0 & ie^{ik_+L-i\phi}\sqrt{T'_1R_1} \\ -i\sqrt{T_1T'_1} & -T_1 & 0 & e^{ik_+L-i\phi}\sqrt{T_1R_1} \\ 0 & 0 & 0 & 0 \\ -ie^{ik_++i\phi}\sqrt{T'_1R_1} & -e^{ik_++i\phi}\sqrt{T_1R_1} & 0 & e^{i(k_++k_+)L}R_1 \end{pmatrix},$$

where we abbreviated $\varepsilon_{\pm} = \varepsilon \pm (1/2)\hbar\omega_M$, $k = k(\varepsilon)$, and $k_{\pm} = k(\varepsilon \pm \hbar\omega_M)$.

For the currents in the four leads we then obtain the DC components from Eq. (3.13)

$$\begin{aligned} I_1(0) &= \frac{e}{h} \int d\varepsilon [f_1(\varepsilon) - R_1f_2(\varepsilon) - T_1f_8(\varepsilon) - T'_1f_7(\varepsilon)], \\ I_2(0) &= \frac{e}{h} \int d\varepsilon [f_2(\varepsilon) - R_1f_1(\varepsilon) - T_1f_7(\varepsilon) - T'_1f_8(\varepsilon)], \\ I_7(0) &= \frac{e}{h} \int d\varepsilon [f_7(\varepsilon) - f_{3+}(\varepsilon)], \\ I_8(0) &= \frac{e}{h} \int d\varepsilon [f_8(\varepsilon) - R_1f_7(\varepsilon) - T_1f_1(\varepsilon) - T'_1f_2(\varepsilon)], \end{aligned} \quad (3.26)$$

where $f_{3+}(\varepsilon)$ is given in Eq. (3.24). Since the DC current components do not depend on the reflection amplitude r_M of the magnet — which is consistent with the observation that the magnet does not reflect current in the steady-state regime [14, 13] — the integrations over energy can be carried out explicitly and one finds the simple result

$$\begin{aligned} I_1(0) &= \frac{e^2}{h}(V_1 - R_1V_2 - T_1V_8 - T'_1V_7), \\ I_2(0) &= \frac{e^2}{h}(V_2 - R_1V_1 - T_1V_7 - T'_1V_8), \\ I_7(0) &= \frac{e^2}{h}(V_7 - R_1V_8 - T_1V_2 - T'_1V_1), \\ I_8(0) &= \frac{e^2}{h}(V_8 - R_1V_7 - T_1V_1 - T'_1V_2). \end{aligned} \quad (3.27)$$

Interference between transmission paths that reflect from the magnet and paths that do not reflect from the magnet gives an AC contribution to the current at frequency $\omega = \pm\omega_M$. For the AC components at frequency $\omega = \omega_M$ we find

$$\begin{aligned}
 I_1(\omega_M) &= -i\hat{m}_- \frac{e}{h} \sqrt{T_1 T_1' R_1} \int d\varepsilon r_M(\varepsilon)^* [f_2(\varepsilon_+) - f_8(\varepsilon_+)], \\
 I_2(\omega_M) &= -i\hat{m}_- \frac{e}{h} \sqrt{T_1 T_1' R_1} \int d\varepsilon r_M(\varepsilon)^* [f_8(\varepsilon_+) - f_1(\varepsilon_+)], \\
 I_7(\omega_M) &= 0, \\
 I_8(\omega_M) &= -i\hat{m}_- \frac{e}{h} \sqrt{T_1 T_1' R_1} \int d\varepsilon r_M(\varepsilon)^* e^{ik(\varepsilon_+)L - ik(\varepsilon_-)L} [f_1(\varepsilon_+) - f_2(\varepsilon_+)].
 \end{aligned} \tag{3.28}$$

[The components at $\omega = -\omega_M$ are obtained by complex conjugation, $I_j(-\omega_M) = I_j(\omega_M)^*$.] One verifies that the DC currents sum to zero. Current conservation also applies to the AC current components, if one corrects $I_8(\omega_M)$ for the time delay accumulated during the propagation along the upper interferometer arm.

To make the results for the AC current component more explicit, we now consider a simple model for the reflection from the magnetic insulator,

$$r_M(\varepsilon) = e^{2ik(\varepsilon)L_3} \theta(\Delta - |\varepsilon|), \tag{3.29}$$

where Δ is the magnitude of the magnet-induced exchange gap in the helical edge, L_3 is the length of the interferometer arm between the left point contact and the magnet, and the Heaviside function $\theta(x) = 1$ if $x > 0$ and 0 otherwise. We further set the temperatures T_i to zero, choose $V_1 = V > 0$, $V_2 = V_7 = V_8 = 0$, and approximate $k(\varepsilon) = k_F + \varepsilon/\hbar v_F$. Solving Eq. (3.23) for the precession frequency ω_M then gives

$$\hbar\omega_M = T_1' \min\left(eV, \frac{2\Delta}{2 - T_1'}\right). \tag{3.30}$$

Schematic pictures of the distribution functions $f_{3+}(\varepsilon_+)$ and $f_7(\varepsilon_-)$ for $eV < 2\Delta/(2 - T_1')$ and $eV > 2\Delta/(2 - T_1')$ are shown in Fig. 3.4.

In the limit $T_1' \rightarrow 1$ the right point contact “open” geometry studied in this chapter corresponds to the two-terminal setup studied in Ref. [13]. However, in that work the precession frequency is found to be $\hbar\omega_M = eV$ and does not saturate for $eV > 2\Delta$, as it does here, see Eq. (3.30). This difference can be understood as follows: In the two-terminal geometry of Ref. [13], when a stationary state of the magnet is reached, the current reflected by the magnet that adds angular momentum to the magnet is balanced by the current that removes angular momentum from the magnet. Both reflected currents are proportional to $|r_M(\varepsilon)|^2$. Since it is assumed that the reflection amplitude $r_M(\varepsilon)$ is nonzero for all energies, $r_M(\varepsilon)$ drops out from the stationarity condition, giving the result $\hbar\omega_M = eV$. In the four-terminal geometry

studied in the present work, the magnet has additional channels available, through which it can “lose” angular momentum. These loss-channels dominate over the gain-channel in our simple model, Eq. (3.29), where $|r_M(\varepsilon)|^2 \rightarrow 0$ for $\varepsilon > \Delta$. Hence, ω_M saturates for sufficiently large eV . If we were to take the limit $T'_1 \rightarrow 1$ in the beginning of the calculation, thereby *a priori* reducing the four-terminal geometry to the two-terminal geometry of Ref. [13], before making any additional assumptions about the reflection amplitude $r_M(\varepsilon)$, we would find the same result $\hbar\omega_M = eV$ as in Ref. [13].

For the AC current components we then find $I_1(\omega_M) = I_7(\omega_M) = 0$ and

$$\begin{aligned} I_2(\omega_M) &= -I_8(\omega_M)e^{-i\omega_M L/v_F} \\ &= \frac{eiv_F}{2\pi L_3} \hat{m}_- \sqrt{T_1 T'_1 R_1} \sin \frac{\omega_M L_3}{v_F T'_1} e^{-iL_3[2k_F + \omega_M(R_1 + T_1)/T'_1 v_F]}. \end{aligned} \quad (3.31)$$

For a small applied bias and/or for a small induced gap Δ , one may approximate $\omega_M L_3/v_F T'_1$, $\omega_M L/v_F \ll 1$ for typical device sizes, so that one has

$$\begin{aligned} I_2(\omega_M) &\approx -I_8(\omega_M) \\ &\approx \frac{eiv_F}{2\pi T'_1} \hat{m}_- \sqrt{T_1 T'_1 R_1} e^{-2ik_F L_3}. \end{aligned} \quad (3.32)$$

For a discussion of the physical origin of the alternating current contribution in this interferometer, we focus on I_2 and note that the transmission amplitude between contacts “1” and “2” is the sum of two interfering contributions: A direct contribution with amplitude $\propto \sqrt{R_1}$ and a contribution $\propto \hat{m}_- \sqrt{T_1 T'_1}$ with electrons reflected off the precessing magnet. Because the reflection phase depends on the magnetization direction (via the expectation value of \hat{m}_-), electrons that reflect from the magnet pick-up a time-dependent phase factor $\propto e^{-i\omega_M t}$. As a result, the interference contribution to the transmission probability between the reservoirs “1” (at which the voltage bias is applied) and “2” (at which the current is measured) oscillates with frequency ω_M . At a constant bias voltage, this periodic modulation of the (Landauer-Büttiker) transmission probability between reservoirs leads to an alternating contribution to the current I_2 at frequency ω_M .

That the alternating current component is a time-dependent interference-related modulation of the transmission between reservoirs and not the consequence of a periodic spin current pumped by a precessing magnetization [99] and then converted into a charge current by spin-dependent scattering, can be seen from the presence of the additional phase factor $e^{-2ik_F L_3}$ and the corresponding suppression of the alternating current component if $eV \gtrsim \hbar L_3/v_F$, see Eq. (3.31). Such phase factors are absent in the theory of spin pumping and related phenomena [100]. It can also be seen by comparing the magnitudes of the alternating current component $I_2(\omega_M)$

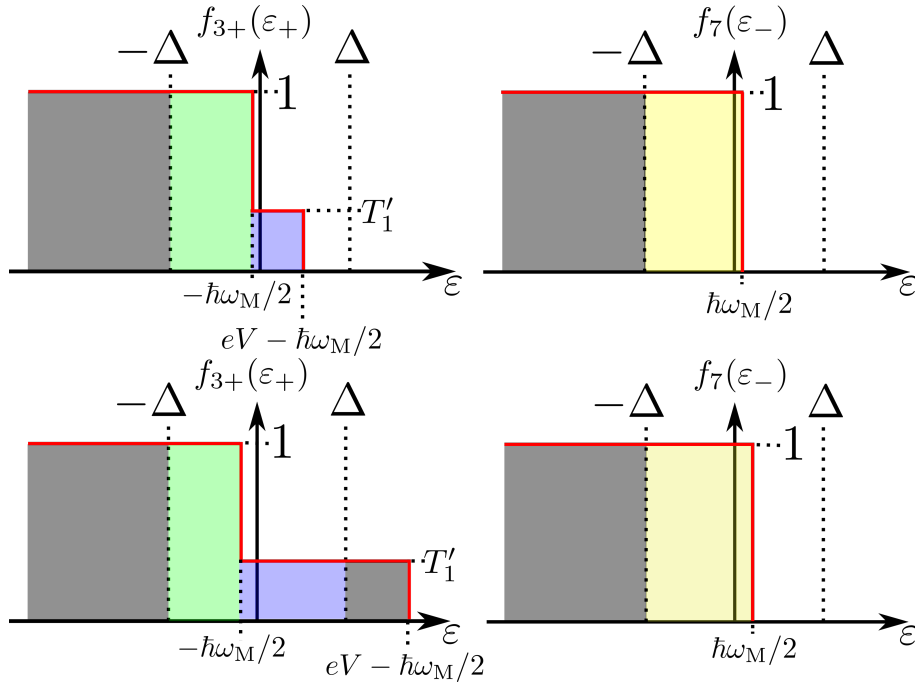


Figure 3.4: Distribution functions $f_{3+}(\epsilon_+)$ and $f_7(\epsilon_-)$ for bias voltage $eV < 2\Delta'/(2-T'_1)$ (top panel) and $eV > 2\Delta'/(2-T'_1)$ (bottom panel). The bias voltage V is applied to lead “1” only; the (electro)chemical potentials of leads “2”, “7”, and “8” are held constant at the value $\mu = 0$.

and the direct current $I_2(0)$. Unlike the AC contribution, the direct current may be interpreted in terms of pumping by the precessing magnetization [14]. For the two-terminal geometry of Refs. [14, 13], the precession frequency of the magnet equals the applied bias, $\hbar\omega_M = eV$, so that in the steady state there is exactly one electron transferred in a period of the precessing magnetization. (This places the throughput of this device in the same category as the electron current pumped through a Coulomb-blockaded quantum dot [20, 101, 102].) The same universal estimate, one electron per period, also holds for the DC currents in the interferometer devices considered in our paper, when applied to the contribution of the DC current $I_3(0) = I_6(0) = I_7(0)$ transmitted through the magnet for bias voltage $|eV| < \Delta$ below the magnet-induced gap. The AC current component $I_2(\omega_M)$, however, may be much larger than this, depending on the values of the transmission coefficients T_1 , T'_1 , and R_1 : From Eq. (3.32) one sees that $I_2(\omega_M)$ may be as large as a charge $\sim e\sqrt{R_1 T_1 / T'_1}$ per period of the precessing magnetization. This charge may be much larger than e in the limit $T'_1 \ll 1$, ruling out pumping as an origin of $I_2(\omega_M)$. (The AC current $I_2(\omega_M)$ is always smaller than the total DC current $I_1(0)$ injected in lead “1”.) We note that the limit $T'_1 \ll 1$ is a physically relevant limit, since, as discussed in chapter 3.2, for scattering between helical edges with equal spin polarization T'_1 is related to spin-flip processes. Such processes originate from the Rashba spin-orbit interaction, sensitive to the inversion-breaking electric field in the contact region. Since such a field is intrinsically weak compared to the crystal fields, one may expect the spin-flip processes to be suppressed, hence $T'_1 \ll 1$. On the other hand, T'_1 may be effectively tuned by external electric fields.

3.3.2 “Classical” vs. “quantum” magnet

The expressions for the AC contributions $I_2(\omega_M)$ given in Eq. (3.31) are proportional to the lowering operator \hat{m}_- . The proper interpretation of these equations requires a brief discussion how expressions for (expectation values of) current components $I_j(n\omega_M)$ that contain the operators \hat{m}_- and \hat{m}_+ should be understood. Hereto, we distinguish the “classical” case that \mathbf{M} is (effectively) a classical vector with a well-defined direction and the “quantum” case that \mathbf{M} must be considered an operator and the magnet is in a state with well-defined M_z , whereas the components M_x and M_y are maximally uncertain.

If the magnet is in a “classical” state $|C\rangle$ describing a macroscopic magnetization, then the magnetization has a well-defined direction at any time t , parametrized by the polar angle θ with the z axis and the azimuthal angle φ . In that case, although $|C\rangle$ is not an eigenstate of any component of the magnetization operator \mathbf{M} , all three components of \mathbf{M} have a finite expectation value. In particular, the expectation value $\langle C|\hat{m}_-|C\rangle \equiv \langle \hat{m}_- \rangle_C$ of the projection of \mathbf{M} on the xy plane takes

the nonzero value

$$\langle \hat{m}_- \rangle_C = e^{i\varphi}. \quad (3.33)$$

[Note that the ladder operators \hat{m}_\pm are defined as $\hat{m}_\pm = (m_x \pm im_y)/|m_x \pm im_y|$, which is why the expectation value from Eq. (3.33) does not depend on the polar angle θ .]

If the magnet is in a “quantum” state $|Q\rangle$ with a sharply-defined quantized value of M_z , the azimuthal angle φ of the magnetization is unknown. In this case one must average over all phase angles φ , so that the expectation value $\langle \hat{m}_- \rangle_Q = 0$. Then, the quantity that should be considered to characterize the AC currents is not the expectation value $\langle I_j(\omega) \rangle_Q$, but the current correlations

$$\langle I(\omega_M)I(-\omega_M) \rangle_Q = \langle I(\omega_M)I^\dagger(\omega_M) \rangle_Q. \quad (3.34)$$

The current correlations are proportional to $\langle \hat{m}_- \hat{m}_+ \rangle_Q = 1$. For example, from Eq. (3.31) one then obtains

$$\langle I_2(\omega_M)I_2^\dagger(\omega_M) \rangle_Q = \frac{e^2 v_F^2}{4\pi^2 L_3^2} T_1 T_1' R_1 \sin^2 \frac{\omega_M L_3}{v_F T_1'}. \quad (3.35)$$

In the same way, the other results for AC currents in chapter 3.3 and in the following chapters can be interpreted in terms of a current correlator. Note that the exchange of energy between the magnet and the helical edge state electrons upon reflection from the magnet is given by Eqs. (3.9)-(3.16), which are independent of the state of the magnet (“classical” vs. “quantum”). Therefore the analysis of the scattering problem works in both cases discussed in this chapter.

3.4 Right point contact “closed”

As a second example we consider a setup in which the point contact to the right of the magnet is fully “closed”, see Fig. 3.5. Although this is effectively a two-terminal geometry (in contrast to the four-terminal geometry of the previous chapter), it has a richer phenomenology, since it allows for AC current components at frequencies ω_M as well as $2\omega_M$. The current component at frequency $2\omega_M$ comes from interference of electrons reflecting off the left end of the magnet (where energy is decreased by $\hbar\omega_M$ upon reflection) and the right end of the magnet (where an energy quantum $\hbar\omega_M$ is absorbed upon reflection), so that the net energy difference in the interference process is $2\hbar\omega_M$.

For the scattering matrix $S^{(C2)}$ the condition that the right point contact is “closed” translates to $R_2 = 1$, $T_2 = T_2' = 0$, so that $\hat{a}_{5\pm}(\varepsilon) = \pm \hat{a}_{6\mp}(\varepsilon)$. As we will show below, in this setup the current has AC components at frequencies ω_M and $2\omega_M$. To keep the expressions simple, we will assume that the left point contact

is close to being “open”, $R_1, T_1' \ll 1$ and give final expressions to lowest nontrivial order in R_1, T_1' . The leads labeled “7” and “8” are disconnected from the magnet and will not be considered here.

By solving Eqs. (3.5) and (3.9), the operators $\hat{a}_{3+}(\varepsilon)$ and $\hat{a}_{6+}(\varepsilon)$ for electrons incident on the magnet can be expressed in terms of the operators $\hat{a}_{1+}(\varepsilon)$ and $\hat{a}_{2+}(\varepsilon)$ for electrons incoming from the reservoirs on the left side. To first order in $\sqrt{R_1}, \sqrt{T_1'}$ we find

$$\begin{aligned} \hat{a}_{3+}(\varepsilon_+) &= -\hat{a}_{1+}(\varepsilon_-)e^{ik(\varepsilon_-)L+ik(\varepsilon_+)L}\hat{m}_-r_M'(\varepsilon)\sqrt{R_1} \\ &\quad + \hat{a}_{2+}(\varepsilon_+) \left[1 + e^{-i\phi+ik(\varepsilon_+)L}t_M(\varepsilon)\sqrt{R_1} \right] \\ &\quad + i\hat{a}_{1+}(\varepsilon_+)\sqrt{T_1'}, \end{aligned} \quad (3.36)$$

$$\begin{aligned} \hat{a}_{6+}(\varepsilon_-) &= e^{i\phi+ik(\varepsilon_-)L} \left\{ i\hat{a}_{2+}(\varepsilon_-)\sqrt{T_1'} \right. \\ &\quad - \hat{a}_{1+}(\varepsilon_-) \left[1 + e^{i\phi+ik(\varepsilon_-)L}t_M'(\varepsilon)\sqrt{R_1} \right] \\ &\quad \left. - \hat{a}_{2+}(\varepsilon_+)\hat{m}_-r_M(\varepsilon)\sqrt{R} \right\}. \end{aligned} \quad (3.37)$$

The results for the operators $\hat{a}_{j-}(\varepsilon)$ for the outgoing modes in the leads $j = 1, 2$ are again expressed in terms of the matrices of coefficients $S_{j;k}^{(n)}(\varepsilon)$, which are effectively 2x2-matrices for the geometry we consider here. These matrices read

$$\begin{aligned} S^{(-)}(\varepsilon) &= r_M'(\varepsilon_-)\hat{m}_-e^{i(k+k_-)L} \\ &\quad \times \begin{pmatrix} 1 + \sqrt{R_1}[t_M(\varepsilon_-)e^{-i(\phi-kL)} + t_M'(\varepsilon_-)e^{i(\phi+k_-L)}] & i\sqrt{T_1'} \\ i\sqrt{T_1'} & -T_1' \end{pmatrix}, \\ S^{(0)}(\varepsilon) &= e^{ikL} \begin{pmatrix} i\sqrt{T_1'}[e^{i\phi}t_M'(\varepsilon_+) - e^{-i\phi}t_M(\varepsilon_-)] & -e^{-i\phi}t_M(\varepsilon_-) \\ e^{i\phi}t_M'(\varepsilon_+) & i\sqrt{T_1'}[e^{i\phi}t_M'(\varepsilon_+) - e^{-i\phi}t_M(\varepsilon_-)] \end{pmatrix} \\ &\quad + \sqrt{R_1} \begin{pmatrix} \sqrt{T_1'}\sum_{\pm}[\pm e^{i(k+k_{\pm})L}r_M(\varepsilon_{\pm})r_M'(\varepsilon_{\pm})] & i[e^{i(k+k_-)L}r_M(\varepsilon_-)r_M'(\varepsilon_-) - 1] \\ i[1 - e^{i(k+k_+)L}r_M(\varepsilon_+)r_M'(\varepsilon_+)] & \sqrt{T_1'}\sum_{\pm}[\pm e^{i(k+k_{\pm})L}r_M(\varepsilon_{\pm})r_M'(\varepsilon_{\pm})] \end{pmatrix}, \\ S^{(+)}(\varepsilon) &= r_M(\varepsilon_+)\hat{m}_+ \begin{pmatrix} T_1' & -i\sqrt{T_1'} \\ -i\sqrt{T_1'} & -1 - \sqrt{R_1}[t_M(\varepsilon_+)e^{-i(\phi-k_+L)} + t_M'(\varepsilon_+)e^{i(\phi+kL)}] \end{pmatrix}, \end{aligned} \quad (3.38)$$

where we again abbreviated $\varepsilon_{\pm} = \varepsilon \pm (1/2)\hbar\omega_M$, $k = k(\varepsilon)$, and $k_{\pm} = k(\varepsilon \pm \hbar\omega_M)$. We have kept contributions beyond the lowest order in $\sqrt{R_1}$ and $\sqrt{T_1'}$ as far as these are important for a consistent expansion of the currents for small $\sqrt{R_1}$ and $\sqrt{T_1'}$ and for small bias voltage.

We proceed to calculate the steady-state precession frequency ω_M and the currents I_1 and I_2 . The steady-state precession frequency ω_M is calculated from Eq. (3.20)

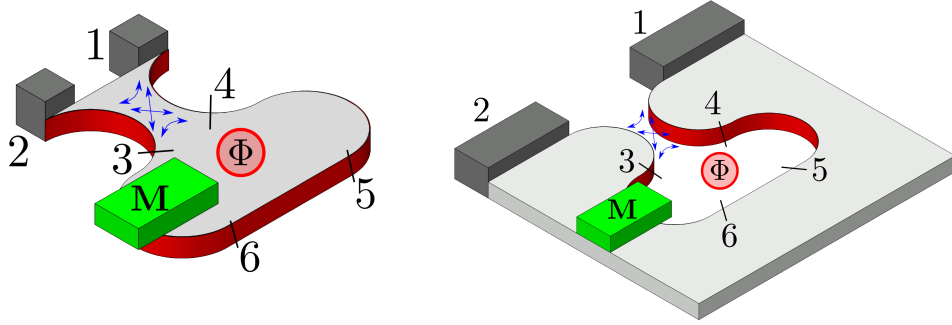


Figure 3.5: Schematic picture of the “right point contact closed” geometry for a realization in which the interfering edge channels are on the same quantum spin Hall insulator (left) and on different quantum spin Hall insulators (right). The positions labeled $i = 1, 2, \dots, 8$ refer to the reference positions used for the calculations in the main text.

upon setting $\dot{M}_z = 0$. In the limit $T'_1, R_1 \ll 1$ Eq. (3.20) gives

$$0 = \int d\varepsilon |r_M(\varepsilon)|^2 [f_2(\varepsilon_+) - f_1(\varepsilon_-)], \quad (3.39)$$

from which ω_M can be determined. (Explicit results for a simple model will be given below.) The DC current components $I_1(0)$ and $I_2(0)$ now acquire a weak dependence on the reflection amplitude r_M of the magnet,

$$\begin{aligned} I_1(0) &= -I_2(0) \\ &= \frac{e^2}{h}(V_1 - V_2) + \frac{e}{h}\sqrt{R_1} \int d\varepsilon |r_M(\varepsilon_-)|^2 [f_2(\varepsilon) - f_1(\varepsilon - \hbar\omega_M)] \\ &\quad \times \left\{ t'_M(\varepsilon_-) e^{i(\phi+k-L)} + t'^*_M(\varepsilon_-) e^{-i(\phi+k-L)} + t_M(\varepsilon_-) e^{-i(\phi-kL)} + t^*_M(\varepsilon_-) e^{i(\phi-kL)} \right\}, \end{aligned} \quad (3.40)$$

where we kept only those correction terms that depend on the Aharonov-Bohm phase ϕ . Note that $\omega_M = 0$ if $V_1 = V_2$, so that $I_j(0) = 0$, $j = 1, 2$ in the absence of

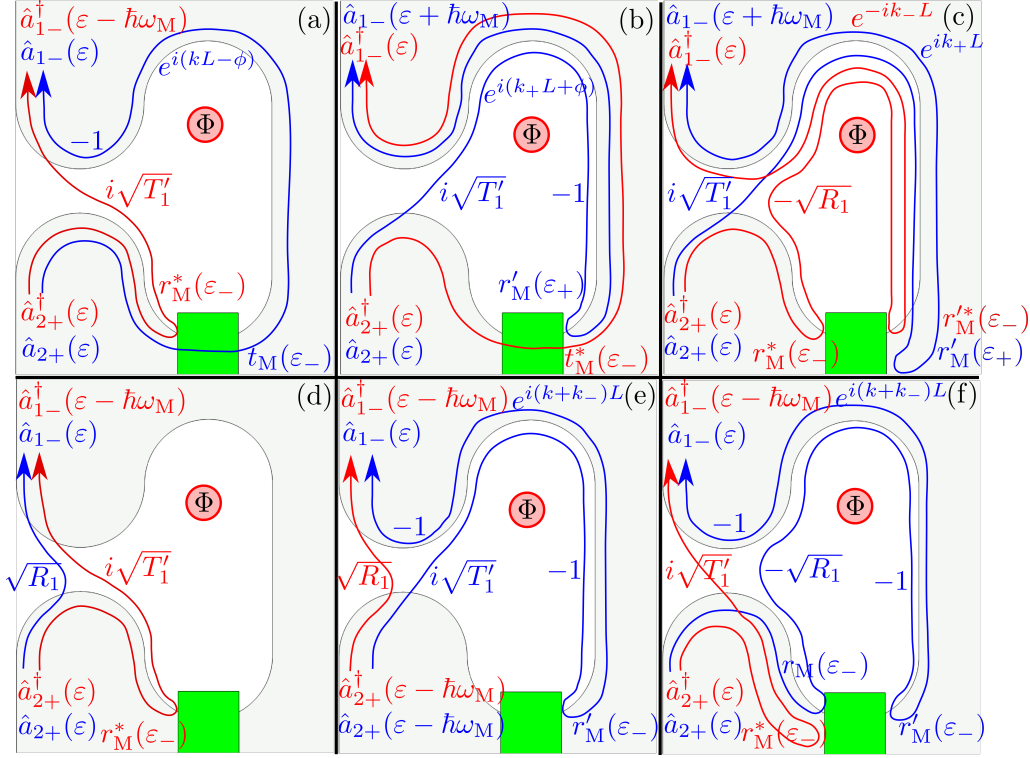


Figure 3.6: Contributions to the AC current amplitude $I_1(\omega_M)$ in lead “1” that depend on the distribution function $f_2(\varepsilon)$ in lead “2”. The panels (a)–(f) are in the same order as the terms of Eq. (3.41), but when attempting to match the expressions from the panels to Eq. (3.41) care must be taken as explained in the following. An overall minus sign that comes from the definition of the current $I_1(\omega)$ in Eq. (3.3) is not included. In panel (a) unitarity of $S^{(M)}$ must be used to make the replacement $-r_M^*(\varepsilon_-)t_M(\varepsilon_-) = r'_M(\varepsilon_-)t_M^*(\varepsilon_-)$ to arrive at the corresponding term in Eq. (3.41). In comparison to Eq. (3.41), the contribution from panel (f) contains an extra factor of $|r_M(\varepsilon_-)|^2$. This factor has been dropped in Eq. (3.41), as $\sqrt{T'_1 R_1} r'_M(\varepsilon_-) |r_M(\varepsilon_-)|^2 \approx \sqrt{T'_1 R_1} r'_M(\varepsilon_-)$ to the level of approximation made in Eq. (3.41). In panels (c) and (f) the property $\hat{m}_- \hat{m}_+ = \mathbb{1}$ is used, as the red or blue paths reflect off both sides of the magnet. The factors of -1 , $\sqrt{R_1}$ and $i\sqrt{T'_1}$ printed along the paths come from the scattering matrix elements of $S^{(C1)}$ and $S^{(C2)}$ related to the paths that are shown in the limits considered.

an applied bias. The AC components at frequency $\omega = \omega_M$ are

$$\begin{aligned}
I_1(\omega_M) &= i\hat{m}_- \sqrt{T'_1} \frac{e}{h} \int d\varepsilon \left\{ r'_M(\varepsilon_-) t'^*_M(\varepsilon_-) e^{-i\phi} e^{ikL} [f_1(\varepsilon - \hbar\omega_M) - f_2(\varepsilon)] \right. \\
&\quad \left. - r'_M(\varepsilon_+) e^{i\phi} e^{ik+L} t'^*_M(\varepsilon_-) [f_1(\varepsilon) - f_2(\varepsilon)] \right\} \\
&\quad + i\hat{m}_- \sqrt{T'_1 R_1} \frac{e}{h} \int d\varepsilon \left\{ -e^{i(k_+ - k_-)L} r'_M(\varepsilon_+) r'^*_M(\varepsilon_-) r^*_M(\varepsilon_-) [f_1(\varepsilon) - f_2(\varepsilon)] \right. \\
&\quad \left. + r^*_M(\varepsilon_-) [f_1(\varepsilon - \hbar\omega_M) - f_2(\varepsilon)] - e^{i(k_- + k)L} r'_M(\varepsilon_-) [f_2(\varepsilon - \hbar\omega_M) - f_2(\varepsilon)] \right\}, \\
I_2(\omega_M) &= i\hat{m}_- \sqrt{T'_1} \frac{e}{h} \int d\varepsilon \left\{ r^*_M(\varepsilon_-) t_M(\varepsilon_-) e^{-i\phi} e^{ikL} [f_1(\varepsilon - \hbar\omega_M) - f_2(\varepsilon)] \right. \\
&\quad \left. - r^*_M(\varepsilon_-) e^{i\phi} e^{ikL} t'_M(\varepsilon_+) [f_1(\varepsilon) - f_2(\varepsilon)] \right\} \\
&\quad + i\hat{m}_- \sqrt{T'_1 R_1} \frac{e}{h} \int d\varepsilon \left\{ -e^{i(k+k_+)L} r_M(\varepsilon_+) r'_M(\varepsilon_+) r^*_M(\varepsilon_-) [f_1(\varepsilon) - f_2(\varepsilon)] \right. \\
&\quad \left. + e^{i(k_- + k)L} r'_M(\varepsilon_-) [f_1(\varepsilon - \hbar\omega_M) - f_2(\varepsilon)] - r^*_M(\varepsilon_-) [f_1(\varepsilon - \hbar\omega_M) - f_1(\varepsilon)] \right\}, \tag{3.41}
\end{aligned}$$

where we have also included a sub-leading contribution in the expansion for $\sqrt{T'_1}$, $\sqrt{R_1}$, which we consider, because the leading contribution vanishes for small bias voltage if the Fermi energy is in the magnet-induced spectral gap. As an illustration, the six configurations of transmission paths that give the $f_2(\varepsilon)$ -dependent contributions to $I_1(\omega_M)$ are shown in Fig. 3.6. The AC components at frequency $\omega = 2\omega_M$ are

$$\begin{aligned}
I_1(2\omega_M) &= -I_2(2\omega_M) \\
&= i\hat{m}_-^2 T'_1 \frac{e}{h} \int d\varepsilon e^{i(k+k_+)L} r'_M(\varepsilon_+) r^*_M(\varepsilon_-) [f_2(\varepsilon) - f_1(\varepsilon)]. \tag{3.42}
\end{aligned}$$

These AC current components at frequency $2\omega_M$ can be understood just as in Fig. 3.6, the difference being that the red and blue paths must now be reflected from opposite sides of the magnet so that their total energy difference is $2\hbar\omega_M$ and not $\hbar\omega_M$, as it is for the interference partners shown in Fig. 3.6. To obtain explicit results, we again consider a simplified model for the reflection and transmission from the magnetic insulator,

$$\begin{aligned}
r_M(\varepsilon) &= e^{2ik_F L_3} \theta(\Delta - |\varepsilon|), \\
r'_M(\varepsilon) &= \theta(\Delta - |\varepsilon|), \\
t_M(\varepsilon) &= t'_M(\varepsilon) = ie^{ik_F L_3} \theta(|\varepsilon| - \Delta). \tag{3.43}
\end{aligned}$$

In comparison to the model, Eq. (3.29), used in the previous chapter, we have made the further simplification that $\omega_M L_3/v_F$, $\omega_M L/v_F \ll 1$ already at the beginning of the calculation, which allows us to replace $k(\varepsilon)$ by k_F in the expression for $r_M(\varepsilon)$

and in the phase factor $e^{ik(\varepsilon)L}$ for transmission through the interferometer arm. The phase shift associated with $r'_M(\varepsilon)$ is absorbed into the phase factor e^{ikL} , i.e. the length L of the upper arm is extended to include the distance between the (closed) right point contact and the magnet. The correction to the DC current, Eq. (3.40), vanishes in the simple model because the product $r_M(\varepsilon)t_M(\varepsilon) = r_M(\varepsilon)t'_M(\varepsilon) = 0$ at all energies ε . To keep the final expressions for the AC current components simple, we also set the temperature to zero, and choose $V_1 = V$ and $V_2 = V_7 = V_8 = 0$. Solving Eq. (3.39) for the precession frequency ω_M gives

$$\hbar\omega_M = -\min[eV, 2\Delta]. \quad (3.44)$$

The AC components at $\omega = \omega_M$ are then given by

$$\begin{aligned} I_1(\omega_M) &= \hat{m}_- \sqrt{T'_1} \frac{e}{h} e^{i\phi + ik_F(L-L_3)} \min[\Delta + 3\hbar\omega_M/2, 0] \\ &\quad - i\hat{m}_- \sqrt{T'_1 R_1} \frac{e}{h} \{ e^{-2ik_F L_3} \min[-\hbar\omega_M, \Delta + \hbar\omega_M/2] + e^{2ik_F L} \hbar\omega_M \}, \\ I_2(\omega_M) &= -i\hat{m}_- \sqrt{T'_1 R_1} \frac{e}{h} (e^{2ik_F L} - e^{-2ik_F L_3}) \min[-\hbar\omega_M, \Delta + \hbar\omega_M/2]. \end{aligned} \quad (3.45)$$

The AC components at $\omega = 2\omega_M$ are

$$\begin{aligned} I_1(2\omega_M) &= -I_2(2\omega_M) \\ &= -i\hat{m}_-^2 \frac{e}{h} T'_1 e^{-2ik_F(L-L_3)} \min[-\hbar\omega_M, \Delta + \hbar\omega_M/2]. \end{aligned} \quad (3.46)$$

The remarks from chapter 3.3.2 apply when interpreting these AC current contributions in the case of a “quantum” magnet with sharply defined M_z .

3.5 Full interferometer

In this chapter we will now present results for the full interferometer, see Fig. 3.1, for which all reflection and transmission coefficients R_j , T_j , and T'_j , $j = 1, 2$, are nonzero. To keep the expressions concise, we give analytical results to lowest nontrivial order in R_j , T'_j , $j = 1, 2$, only. These are compared with a numerical evaluation of the full expression in Fig. 3.7.

As before, the precession frequency of the magnet is obtained from the relation $\dot{M}_z = 0$. To first nonzero order on either side of the magnet we obtain

$$\begin{aligned} 0 &= \int d\varepsilon \{ |r_M(\varepsilon)|^2 [f_2(\varepsilon_+) - f_7(\varepsilon_-)] + T'_1 [f_1(\varepsilon_+) - f_2(\varepsilon_+)] + R_1 [f_8(\varepsilon_+) - f_2(\varepsilon_+)] \\ &\quad + T'_2 [f_7(\varepsilon_-) - f_8(\varepsilon_-)] + R_2 [f_7(\varepsilon_-) - f_1(\varepsilon_-)] \}, \end{aligned} \quad (3.47)$$

where we also kept sub-leading terms because the leading contribution may vanish if $V_2 = V_7$. The leading contribution to the DC currents in the four leads is then

$$\begin{aligned}
I_1(0) &= \frac{e}{h} \int d\varepsilon \{f_1(\varepsilon) - f_8(\varepsilon)\} + \frac{2e}{h} \operatorname{Re} \int d\varepsilon \left\{ \sqrt{R_1 R_2} t_M(\varepsilon_-) e^{-i(\phi-kL)} [f_2(\varepsilon) - f_8(\varepsilon)] \right. \\
&\quad \left. + \sqrt{T_1' T_2'} t_M'(\varepsilon_+) e^{i(\phi-kL)} [f_8(\varepsilon) - f_7(\varepsilon)] \right\}, \\
I_2(0) &= \frac{e}{h} \int d\varepsilon \{f_2(\varepsilon) - f_7(\varepsilon) + |r_M(\varepsilon_-)|^2 [f_7(\varepsilon - \hbar\omega_M) - f_2(\varepsilon)]\} \\
&\quad + \frac{2e}{h} \operatorname{Re} \int d\varepsilon \left\{ \sqrt{R_1 R_2} t_M'(\varepsilon_+) e^{i(\phi+kL)} [f_1(\varepsilon) - f_7(\varepsilon)] \right. \\
&\quad + \sqrt{T_1' T_2'} t_M'(\varepsilon_+) e^{i(\phi-kL)} [f_7(\varepsilon) - f_8(\varepsilon)] + \sqrt{R_1 R_2} |r_M(\varepsilon_-)|^2 [t_M(\varepsilon_-) e^{-i(\phi-kL)} \\
&\quad \left. + t_M'(\varepsilon_-) e^{i(\phi+k-L)}] [f_7(\varepsilon - \hbar\omega_M) - f_2(\varepsilon)] \right\}, \\
I_7(0) &= \frac{e}{h} \int d\varepsilon \{f_7(\varepsilon) - f_2(\varepsilon) - |r_M(\varepsilon_-)|^2 [f_7(\varepsilon - \hbar\omega_M) - f_2(\varepsilon)]\} \\
&\quad + \frac{2e}{h} \operatorname{Re} \int d\varepsilon \left\{ \sqrt{R_1 R_2} t_M(\varepsilon_-) e^{-i(\phi-kL)} [f_8(\varepsilon) - f_2(\varepsilon)] \right. \\
&\quad + \sqrt{T_1' T_2'} t_M(\varepsilon_-) e^{-i(\phi+kL)} [f_2(\varepsilon) - f_1(\varepsilon)] + \sqrt{R_1 R_2} |r_M(\varepsilon_-)|^2 [t_M(\varepsilon_-) e^{-i(\phi-kL)} \\
&\quad \left. + t_M'(\varepsilon_-) e^{i(\phi+k-L)}] [f_2(\varepsilon) - f_7(\varepsilon - \hbar\omega_M)] \right\}, \\
I_8(0) &= \frac{e}{h} \int d\varepsilon \{f_8(\varepsilon) - f_1(\varepsilon)\} + \frac{2e}{h} \operatorname{Re} \int d\varepsilon \left\{ \sqrt{R_1 R_2} t_M'(\varepsilon_+) e^{i(\phi+kL)} [f_7(\varepsilon) - f_1(\varepsilon)] \right. \\
&\quad \left. + \sqrt{T_1' T_2'} t_M(\varepsilon_-) e^{-i(\phi+kL)} [f_1(\varepsilon) - f_2(\varepsilon)] \right\}, \tag{3.48}
\end{aligned}$$

where the subleading terms contain the ϕ -dependent contribution to the DC current

only. Similarly, for the AC currents we find

$$\begin{aligned}
 I_1(\omega_M) &= i\hat{m}_- \frac{e}{h} \int d\varepsilon \left\{ \sqrt{R_2 T_2'} r_M'(\varepsilon_+) e^{-iL(k-k_+)} [f_7(\varepsilon) - f_8(\varepsilon)] \right. \\
 &\quad \left. + \sqrt{R_1 T_1'} r_M^*(\varepsilon_-) [f_8(\varepsilon) - f_2(\varepsilon)] \right\}, \\
 I_2(\omega_M) &= i\hat{m}_- \sqrt{R_1 T_1'} \frac{e}{h} \int d\varepsilon r_M^*(\varepsilon_-) [f_1(\varepsilon) - f_8(\varepsilon)], \\
 I_7(\omega_M) &= -i\hat{m}_- \sqrt{R_2 T_2'} \frac{e}{h} \int d\varepsilon r_M'(\varepsilon_+) [f_1(\varepsilon) - f_8(\varepsilon)], \\
 I_8(\omega_M) &= i\hat{m}_- \frac{e}{h} \int d\varepsilon \left\{ \sqrt{R_2 T_2'} r_M'(\varepsilon_+) [f_1(\varepsilon) - f_7(\varepsilon)] \right. \\
 &\quad \left. + \sqrt{R_1 T_1'} r_M^*(\varepsilon_-) e^{-iL(k_- - k)} [f_2(\varepsilon) - f_1(\varepsilon)] \right\}, \tag{3.49}
 \end{aligned}$$

$$\begin{aligned}
 I_1(2\omega_M) &= -I_2(2\omega_M) \\
 &= -\hat{m}_-^2 \frac{e}{h} \int d\varepsilon e^{-iL(k-k_+)} r_M'(\varepsilon_+) r_M^*(\varepsilon_-) \left\{ R_2 T_1' e^{2iLk} [f_1(\varepsilon) - f_2(\varepsilon)] \right. \\
 &\quad \left. + \sqrt{R_1 R_2 T_1' T_2'} [f_8(\varepsilon) - f_7(\varepsilon)] \right\}, \\
 I_7(2\omega_M) &= -I_8(2\omega_M) \\
 &= \hat{m}_-^2 \frac{e}{h} \int d\varepsilon e^{-iL(k_- + k)} r_M'(\varepsilon_+) r_M^*(\varepsilon_-) \left\{ \sqrt{R_1 R_2 T_1' T_2'} e^{2iLk} [f_1(\varepsilon) - f_2(\varepsilon)] \right. \\
 &\quad \left. + R_1 T_2' [f_8(\varepsilon) - f_7(\varepsilon)] \right\}. \tag{3.50}
 \end{aligned}$$

For the simplified model defined by Eq. (3.43) and the subsequent discussion we compare the expressions shown in Eqs. (3.47)–(3.50) for small T_j' , R_j , $j = 1, 2$, with a numerical evaluation of the full solution of the scattering problem. Figure 3.7 shows the result of this comparison for the bias voltages $V_1 = V > 0$, $V_2 = V_7 = V_8 = 0$. The ϕ -dependent contribution to the DC current in lead “2” shown in Fig. 3.7 is calculated as

$$I_{2,AB}(0) \equiv \frac{1}{2\pi} \left\{ \int_0^{2\pi} d\phi (I_2(0)^2 - \langle I_2(0) \rangle^2) \right\}^{1/2}, \tag{3.51}$$

where

$$\langle I_2(0) \rangle = \frac{1}{2\pi} \int_0^{2\pi} d\phi I_2(0). \tag{3.52}$$

3.6 Finite- T enhancement of DC Aharonov-Bohm currents

All previous explicit results for the simple model, Eq. (3.43), were calculated at zero temperature ($T = 0$). In this chapter we consider the effect of the Aharonov-

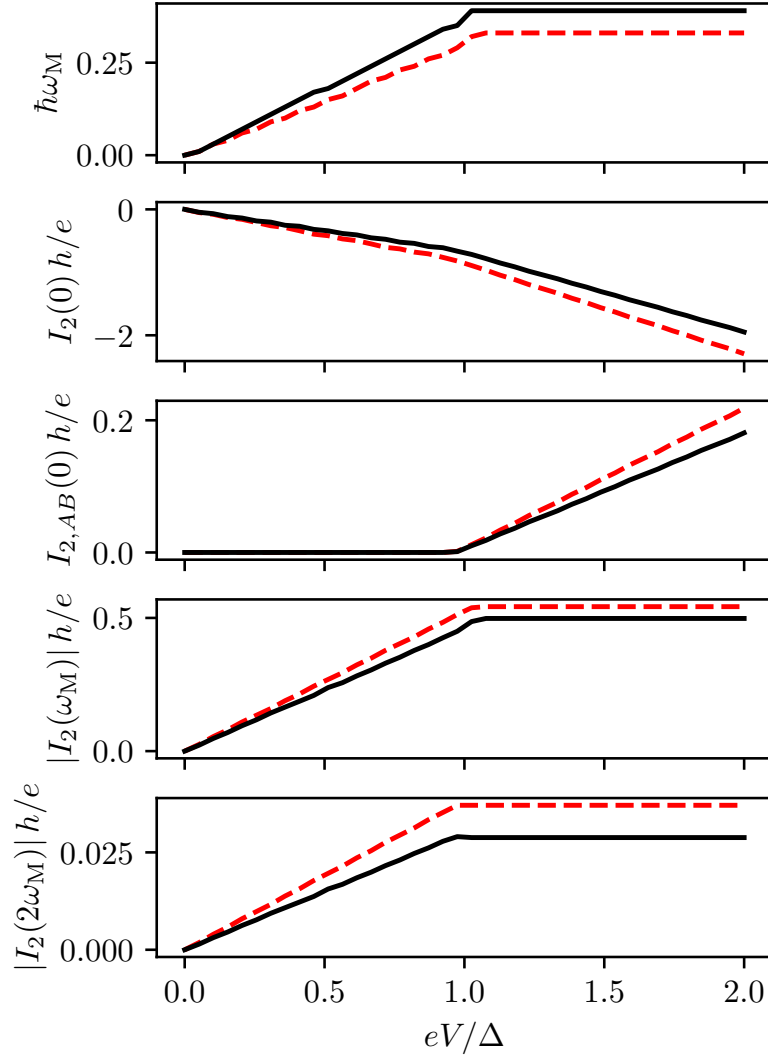


Figure 3.7: From top to bottom: Precession frequency ω_M , DC current $I_2(0)$ at zero Aharonov-Bohm phase ϕ , ϕ -dependent contribution to DC current defined in Eq. (3.51) and the magnitude $|I_2(\omega_M)|$ and $|I_2(2\omega_M)|$ of the AC current components at frequency ω_M and $2\omega_M$, as a function of the bias voltage V at lead “1”. All currents are evaluated in lead “2”. The solid curves show the numerical evaluation of the full solution without the approximation of small R_j , T'_j , $j = 1, 2$. The dashed curves are obtained using the analytical expressions of Eqs. (3.47)–(3.50), with the exception of the second panel, where we have included all ϕ -independent terms up to second order in $(R_j)^{1/2}$, $(T'_j)^{1/2}$, not only those of lowest non-trivial order given in $I_2(0)$ in Eqs. (3.48). The parameters are chosen as $T_1 = 0.79$, $R_1 = 0.09$, $T'_1 = 0.12$, $T_2 = 0.78$, $R_2 = 0.06$, $T'_1 = 0.16$, $k_F L = 1$ and $k_F L_3 = 0.1$.

Bohm phase ϕ on the DC current at finite temperature. We find that, if the Fermi energy is in the magnet-induced gap, increasing T leads to an increase of the ϕ -dependent Aharonov-Bohm contributions to the DC current. The reason is that coherent transmission through the magnet, which is required for a dependence on the Aharonov-Bohm phase ϕ , exists for above-gap energies only. The population of the above-gap states increases with temperature, which causes the ϕ -dependent current contribution to increase. The visibility of the Aharonov-Bohm oscillations decreases again at higher temperatures, when thermal smearing effects start to dominate.

As before, we choose the biases $V_1 = V > 0$ and $V_2 = V_7 = V_8 = 0$ and use the simple model given in Eq. (3.43) to calculate the ϕ -dependent contributions to the DC current. At finite temperature, the distribution functions are $f_j(\varepsilon) = [1 + e^{(\varepsilon - eV_j)/k_B T}]^{-1}$ with equal temperature T applied to all four leads $j = 1, 2, 7, 8$.

Flux-dependent contributions to the DC current do not appear in the “open” geometry of chapter 3.3. They do appear in principle for the “closed” geometry of chapter 3.4, but not for the simple model given in Eq. (3.43), since all the ϕ -dependent terms of Eq. (3.40) are proportional to $r_M(\varepsilon_-)t_M(\varepsilon_-)$, which is zero for that model. Hence, the discussion here focuses on the full interferometer geometry of chapter 3.5. Starting point of our analysis is Eq. (3.48), which gives the DC currents $I_j(0)$ for general distribution functions $f_j(\varepsilon)$. Specializing to the simple model, Eq. (3.43), and restricting to the flux dependent part $\delta I_j(0, \phi)$ of the DC current, we find

$$\begin{aligned}
 \delta I_1(0, \phi) &= 0, \\
 \delta I_2(0, \phi) &= -\frac{2e}{h} \sqrt{R_1 R_2} \sin[k_F(L_3 + L) + \phi] \\
 &\quad \times \left\{ \int_{-\infty}^{-\Delta - \hbar\omega_M/2} d\varepsilon [f_1(\varepsilon) - f_7(\varepsilon)] + \int_{\Delta - \hbar\omega_M/2}^{\infty} d\varepsilon [f_1(\varepsilon) - f_7(\varepsilon)] \right\}, \\
 \delta I_7(0, \phi) &= -\frac{2e}{h} \sqrt{T'_1 T'_2} \sin[k_F(L_3 - L) - \phi] \\
 &\quad \times \left\{ \int_{-\infty}^{-\Delta + \hbar\omega_M/2} d\varepsilon [f_2(\varepsilon) - f_1(\varepsilon)] + \int_{\Delta + \hbar\omega_M/2}^{\infty} d\varepsilon [f_2(\varepsilon) - f_1(\varepsilon)] \right\}, \\
 \delta I_8(0, \phi) &= -I_2(0, \phi) - I_7(0, \phi). \tag{3.53}
 \end{aligned}$$

The integrals can be performed analytically and for our choice of biases they are

$$\begin{aligned}
\delta I_2(0, \phi) &= -\frac{2ek_{\text{B}}T}{h} \sqrt{R_1 R_2} \sin [k_{\text{F}}(L_3 + L) + \phi] \\
&\times \left[\frac{eV}{k_{\text{B}}T} + \ln \cosh \frac{\Delta + \hbar\omega_{\text{M}}/2}{2k_{\text{B}}T} - \ln \cosh \frac{eV + \Delta + \hbar\omega_{\text{M}}/2}{2k_{\text{B}}T} \right. \\
&\quad \left. - \ln \cosh \frac{\Delta - \hbar\omega_{\text{M}}/2}{2k_{\text{B}}T} + \ln \cosh \frac{eV - \Delta + \hbar\omega_{\text{M}}/2}{2k_{\text{B}}T} \right], \\
\delta I_7(0, \phi) &= \frac{2ek_{\text{B}}T}{h} \sqrt{T'_1 T'_2} \sin [k_{\text{F}}(L_3 - L) - \phi] \\
&\times \left[\frac{eV}{k_{\text{B}}T} + \ln \cosh \frac{\Delta - \hbar\omega_{\text{M}}/2}{2k_{\text{B}}T} - \ln \cosh \frac{eV + \Delta - \hbar\omega_{\text{M}}/2}{2k_{\text{B}}T} \right. \\
&\quad \left. - \ln \cosh \frac{\Delta + \hbar\omega_{\text{M}}/2}{2k_{\text{B}}T} + \ln \cosh \frac{eV - \Delta - \hbar\omega_{\text{M}}/2}{2k_{\text{B}}T} \right],
\end{aligned} \tag{3.54}$$

In the limit of $k_{\text{B}}T \gg \Delta, eV, \hbar\omega_{\text{M}}$, these expressions reduce to

$$\begin{aligned}
\delta I_2(0, \phi) &= -V \frac{2e^2}{h} \sqrt{R_1 R_2} \sin [k_{\text{F}}(L_3 + L) + \phi], \\
\delta I_7(0, \phi) &= V \frac{2e^2}{h} \sqrt{T'_1 T'_2} \sin [k_{\text{F}}(L_3 - L) - \phi],
\end{aligned} \tag{3.55}$$

whereas in the opposite limit $k_{\text{B}}T \rightarrow 0$, we find that the currents vanish, consistent with our previous results. The existence of a temperature-independent visibility of the Aharonov-Bohm oscillations of the DC current at high temperatures continues up to temperatures $k_{\text{B}}T \sim \min(L, L_3)/\hbar v_{\text{F}}$ where L and L_3 are the lengths of the segments of the Aharonov-Bohm ring. The visibility of the Aharonov-Bohm effect is suppressed at higher temperatures because of thermal smearing effects [not present in the simple model shown in Eq. (3.43)]. In Fig. 3.8, we show $\delta I_2(0, \phi)$ from Eq. (3.54), confirming the enhancement of the Aharonov-Bohm oscillations compared to the zero-temperature result of panel 3 of Fig. 3.7.

3.7 Conclusion

In this work, we analyzed electrical transport through a helical edge of a two-dimensional topological insulator exchange-coupled to a magnetic insulator. Despite the presence of an excitation gap, the magnet has no effect on the current if it has an easy-plane anisotropy with the easy plane perpendicular to the spin quantization axis of the helical edge [14, 13]. Here, we show that the exchange coupling to the magnet does affect electrical transport in an interferometer geometry: (1) In

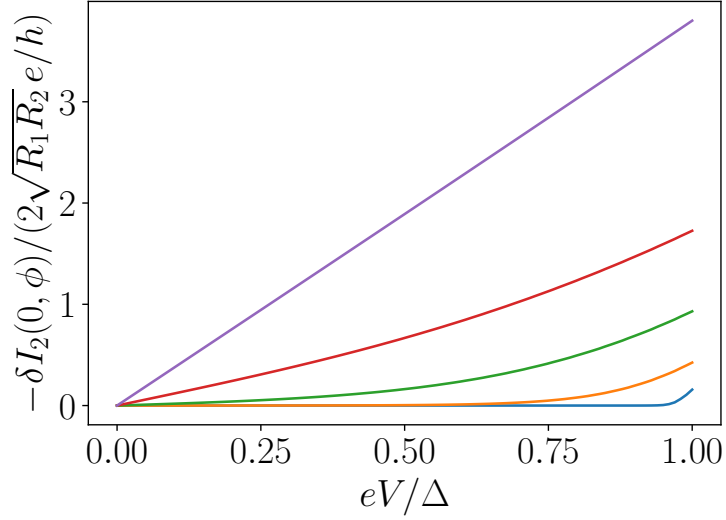


Figure 3.8: Aharonov-Bohm current $\delta I_2(0, \phi)$ from Eq. (3.54) as a function of applied bias V in lead “1” for several values of $k_B T/\Delta$; from bottom to top they are 0.01, 0.1, 0.25, 0.5 and 2. The precession frequency ω_M is determined from the solution of Eq. (3.47) at finite T . The phases are chosen such that $\sin(k_F(L_3 + L) + \phi) = 1$.

a four-terminal geometry, the application of a DC voltage leads to AC currents at frequencies ω_M and $2\omega_M$ with ω_M being the precession frequency of the magnet’s magnetization and (2) if the Fermi energy is in the magnet-induced gap, the usual Aharonov-Bohm-flux dependent oscillations of the DC current are strongly suppressed at zero temperature or bias voltage and show a maximum at temperature or voltage comparable to the magnet-induced gap.

Time-reversal symmetry prohibits backscattering at the two point contacts that define the interferometer. In the limit of helical edges with a well-defined spin polarization, forward scattering between different edges is also suppressed (although it will still be finite), because it requires a spin flip. The alternating currents exist only if there is such spin-flip scattering at the point contacts. They can be traced back to an interference contribution between transmission paths through the interferometer that involve a (spin-flipping) reflection from the precessing magnet and a spin-flip scattering at the contacts. The precessing magnetization inserts a time-dependent phase factor in this interference contribution, thus causing an alternating current contribution for a time-independent applied bias. This origin of the alternating current contribution as a periodic modulation of the interference correction to the (steady-state) conductance must be contrasted with the origin of the direct current through the magnet, which can be seen as a current “pumped” by the precession

magnetization [14]. Consequentially, the magnitude of the direct current through the magnet is closely related to the precession frequency — it is one electron per period of the precessing magnetization —, whereas, depending on the properties of the point contacts and the specific way of biasing the interferometer, the magnitude of the alternating current components can be smaller or larger than that.

An easy-plane ferromagnet exhibits a “spin superfluid” state [81, 83], which has its origin in the formal analogy between the $U(1)$ low-energy degree of freedom of a magnetic moment with easy-plane anisotropy and the $U(1)$ freedom of the superfluid phase [82]. Under suitable external driving, such a spin superfluid can enter into a spiral state in which it carries a dissipationless spin current [81]. In non-topological systems, the bottleneck for observing this dissipationless current is its conversion to measurable spin or charge currents outside the magnet [84, 85]. The system that we consider here (and that was previously considered in Refs. [14, 13]) offers a scenario for a perfect conversion between the charge current in the helical edge of a two-dimensional topological insulator and the “spin superfluid” of the easy-plane ferromagnet. In addition to the absence of shot noise predicted in Ref. [13], the transport properties we identify in this article are unique signatures of the anomalous electric transport in this system.

4 Spontaneous current of a Weyl-semimetal - superconductor heterostructure

This chapter presents the contents of the article [103].

4.1 Introduction

A Weyl semimetal is a three-dimensional crystal with topologically protected nodal points in the band structure [6, 104, 105]. The nodes have a well-defined chirality and they appear in pairs, such that in total the sum of the chiralities vanishes [106]. One manifestation of chiral Weyl nodes and the associated chiral anomaly in crystals is the existence of topologically protected surface states, which connect the projections of two Weyl nodes of opposite chirality on the surface band structure, in the form of two “Fermi arcs” located at opposite surfaces of the Weyl semimetal and moving in opposite directions. Another manifestation is the chiral magnetic effect — an external-magnetic-field induced current of Weyl Fermions directed parallel or antiparallel to the magnetic field depending on the chirality — which leads to unusual non-equilibrium transport properties of the crystal [107, 108, 109, 110, 111]. In equilibrium the chiral anomaly usually remains hidden, since the chiral currents must compensate each other, in agreement with general band-theoretic considerations [112].

As was shown by O’Brien, Beenakker, and Adagideli [15] (see also Ref. [16]), there is, however, a way to circumvent the compensation of chiral anomalies in equilibrium with the help of superconductivity. This is most easily seen in a minimal model of a magnetic Weyl semimetal with two Weyl nodes of opposite chirality and a superconducting s -wave pair potential. If the pair momentum is tuned to the momentum of one of the two Weyl nodes via a flux or a supercurrent bias, superconductivity is induced there and the Weyl node is gapped out, while the node of opposite chirality is left mostly unaffected. In an applied magnetic field, this unaffected chirality gives rise to an equilibrium current, as the opposite chirality is no longer available to carry the compensating current. Unfortunately, making a Weyl semimetal superconducting [113, 114, 115, 116] meets the difficulty of a vanishing density of states at the Weyl nodes, which suppresses the critical temperature. Another obstacle, specifically in the case of a magnetic Weyl semimetal considered in this work, is the

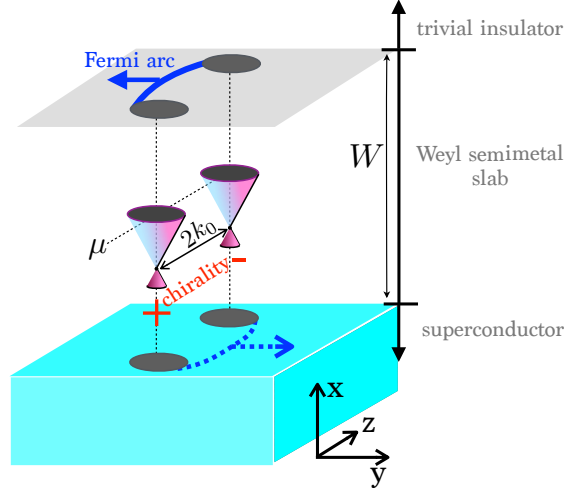


Figure 4.1: Mixed momentum-/real-space illustration of the SN heterostructure considered in this article. It consists of a Weyl semimetal slab of a finite width W with two Weyl nodes separated along the k_z axis and counterpropagating Fermi arcs on the top (solid-blue) and bottom (dotted-blue) surfaces. The Weyl semimetal slab borders on a superconductor (light-blue) at the bottom surface and it is capped by a trivial insulator at the top surface. Because of this built-in spatial asymmetry of the heterostructure, the superconducting proximity effect acts asymmetrically on the two Fermi arcs.

competition with magnetism.

An alternative route to achieve superconducting phases in Weyl semimetals is to make use of the proximity-induced superconductivity in heterostructures by combining an otherwise non-superconducting Weyl semimetal (N) and a conventional superconductor (S) [117, 118, 119, 120]. One prominent type of such heterostructures is the Josephson junction (SNS-heterostructure), which has been extensively studied theoretically exploring the influence of various types of superconducting pairing mechanisms [32, 17, 121, 122, 123, 124, 125, 126, 127, 128, 129, 130, 131, 132, 133], and has also been realized experimentally [134, 119, 135, 136, 137, 138]. Other examples of similar heterostructures are NS-type [139, 140, 141, 142, 117, 143, 144, 145, 120, 146, 147, 148, 149], and NSN-type [150, 151, 152, 153, 154] heterostructures.

While most of these studies investigate equilibrium currents that flow perpendicular to the superconductor - Weyl-semimetal interface, in this article we theoretically investigate the equilibrium current in a bilayer consisting of a Weyl semimetal and a single superconductor (SN bilayer), as illustrated in Fig. 4.1, for which the equilibrium current flows parallel to the interface. We consider a magnetic Weyl semimetal and a conventional s -wave superconductor, both are microscopically inversion-symmetric, so that inversion symmetry is broken only by the interface. To allow for a comparison between different phases, we consider a model for

the normal region which, as a function of parameters, may be in a trivial magnetic insulator phase, Weyl-semimetal phase, or a (three-dimensional) weak Chern insulator phase. We find a significant contribution to the equilibrium current from surface states (Fermi arcs in case of a Weyl semimetal, chiral surface states for the weak Chern insulator), which differs in sign and magnitude from the interfacial current of a trivial insulator [155]. Although our minimal model shows a clear signature at the onset of the topological regime, the magnitude of the equilibrium current is non-universal, because for an inversion-symmetric Weyl semimetal the proximity superconductivity pairs electrons in the topological low-energy band with electrons in a non-topological high-energy band — an effect known as “chirality blockade” [17]. For the minimal model we can isolate the singular contribution to the current from the Fermi-arc surface states by comparing equilibrium currents in a finite-width slab for a chemical potential inside and outside the finite-size gap of the Fermi-arc states at the Weyl node.

The contribution of topological surface states can be interpreted as the result of an effective charge renormalization of the chiral surface modes at the SN interface [156], which leads to a disbalance with the counterpropagating surface modes of the opposite surface and results in a finite current. In this way, the idea of bulk superconductivity acting asymmetrically on chiral states in momentum space [15, 16] is transferred to proximitized superconductivity acting asymmetrically on chiral states in real space. In the former case the equilibrium current is carried by the disbalanced chiral Weyl Fermions in an external magnetic field, in the latter by the disbalanced chiral surface states at zero external magnetic field.

This article is structured as follows: After introducing the minimal model for the SN heterostructure in chapter 4.2, we calculate and discuss the equilibrium current in chapter 4.3. We conclude in chapter 4.4.

4.2 Model

We consider a bilayer consisting of a superconductor (S) and a normal region (N) of width W . We choose coordinates such that the x axis is perpendicular to the superconductor interface and the superconductor interface is at $x = 0$. The normal region corresponds to $0 < x < W$.

Depending on parameters in our model Hamiltonian, the normal region is a topologically trivial magnetic insulator, a magnetic Weyl semimetal, or a three-dimensional weak Chern insulator. At $x = W$ the normal region layer is capped by a non-magnetic trivial insulator. Below, we give lattice models for the Weyl semimetal, the superconductor, and the trivial insulator. To keep the notation simple, the lattice constant and \hbar are set to unity.

4.2.1 Normal region

We model the normal region with the four-band Hamiltonian

$$H^{(W)}(\mathbf{k}) = t\tau_3(\sigma_1 \sin k_x + \sigma_2 \sin k_y) + m(\mathbf{k})\tau_1\sigma_0 + \beta\tau_0\sigma_3 - \mu\tau_0\sigma_0, \quad (4.1)$$

with

$$m(\mathbf{k}) = m_0 + t'(2 - \cos k_x - \cos k_y) + t'_z(1 - \cos k_z), \quad (4.2)$$

where the σ_i and τ_i , $i = 0, 1, 2, 3$ are Pauli matrices corresponding to spin and orbital degrees of freedom, respectively. (These include the identity matrices σ_0 and τ_0 .) Furthermore, μ is the chemical potential, t , t' , and t'_z are hopping parameters, m_0 an orbital-selective on-site potential, and β the exchange field, which is directed in the z direction. For definiteness, all of these parameters are assumed to be positive. The Hamiltonian, shown in Eq. (4.1), satisfies inversion symmetry,

$$H^{(W)}(\mathbf{k}) = \tau_1 H^{(W)}(-\mathbf{k}) \tau_1, \quad (4.3)$$

whereas time-reversal symmetry is broken by the exchange field. (Time-reversal symmetry is represented as $\sigma_2 K$, where K is complex conjugation.) At zero chemical potential μ , the Hamiltonian, see Eq. (4.1), also satisfies a mirror antisymmetry,

$$H_{\mu=0}^{(W)}(k_x, k_y, k_z) = -\sigma_2 \tau_3 H_{\mu=0}^{(W)}(k_x, -k_y, k_z) \sigma_2 \tau_3. \quad (4.4)$$

The Hamiltonian, given in Eq. (4.1), resembles minimal models motivated by materials of the Bi_2Se_3 family [112], where, however, for simplicity we omitted a term proportional to $\tau_3 \sigma_3 \sin k_z$. [Such a term does not significantly alter the topological phases that we are going to study, but its absence makes the analysis more transparent. A term $\propto \tau_3 \sigma_3 \sin k_z$ preserves the inversion symmetry, Eq. (4.3), and the mirror antisymmetry, Eq. (4.4), at $\mu = 0$. We verified that our conclusions remain valid if we include this term.]

The eigenvalues of the Hamiltonian, Eq. (4.1), can easily be calculated in closed form. For each momentum \mathbf{k} there are four eigenvalues, labeled $\varepsilon_{\pm, \pm}$,

$$\varepsilon_{\pm, \pm}(\mathbf{k}) = -\mu \pm \sqrt{t^2(\sin^2 k_x + \sin^2 k_y) + (m(\mathbf{k}) \pm \beta)^2}. \quad (4.5)$$

The two bands with energy eigenvalues $\varepsilon_{\pm, +}(\mathbf{k})$ are completely gapped. The other two bands, which have energy eigenvalues $\varepsilon_{\pm, -}(\mathbf{k})$, may also be gapped or feature two Weyl nodes, depending on the value of the exchange field β . The Weyl-semimetal phase is found for

$$m_0 < \beta < m_0 + 2t'_z. \quad (4.6)$$

In this case, two Weyl nodes exist at $\mathbf{k} = \{0, 0, \pm k_0\}^T$, with

$$k_0 = 2 \arcsin \sqrt{\frac{\beta - m_0}{2t'_z}}, \quad m_0 < \beta < m_0 + 2t'_z. \quad (4.7)$$

For $\beta \downarrow m_0$, one has $k_0 \rightarrow 0$: The two Weyl nodes merge at $k_z = 0$ and gap out for $\beta < m_0$. Hence, for

$$0 < \beta < m_0, \quad (4.8)$$

the system becomes a trivial magnetic insulator, which for a finite exchange field $\beta > 0$ is magnetic. For $\beta \uparrow m_0 + 2t'_z$, one has $k_0 \rightarrow \pi$, and the Weyl nodes merge and gap out at the Brillouin zone boundary. For

$$\beta > m_0 + 2t'_z, \quad (4.9)$$

the system thus becomes a weak Chern insulator [4, 157], which has open surface-state contours extending over the whole Brillouin zone.

To prepare for the description of superconductor heterostructures using the Bogoliubov-de Gennes (BdG) formalism, we double the degrees of freedom by introducing holes with Hamiltonian $-\sigma_2 H^{(W)}(-\mathbf{k})^* \sigma_2$. The resulting Bogoliubov-de Gennes Hamiltonian

$$\mathcal{H}^{(W)} = \begin{pmatrix} H^{(W)} & 0 \\ 0 & -\sigma_2 H^{(W)}(-\mathbf{k})^* \sigma_2 \end{pmatrix}, \quad (4.10)$$

has particle-hole symmetry,

$$\mathcal{H}(\mathbf{k}) = -\nu_2 \sigma_2 \mathcal{H}(-\mathbf{k})^* \nu_2 \sigma_2, \quad (4.11)$$

where Pauli matrices ν_j , $j = 0, 1, 2, 3$, represent the particle-hole degree of freedom.

4.2.2 Heterostructure

The normal region at $0 < x < W$ is embedded between a superconductor for $x < 0$ and a trivial insulator for $x > W$, which we both model by semi-infinite systems in the following way: The lattice Hamiltonians for the superconductor (S) and trivial insulator (I) in the Bogoliubov-de Gennes formulation are

$$\mathcal{H}^{(S)}(\mathbf{k}) = t\nu_3\tau_3\sigma_1 \sin k_x + \Delta\nu_1\tau_0\sigma_0, \quad (4.12)$$

$$\mathcal{H}^{(I)}(\mathbf{k}) = t\nu_3\tau_3\sigma_1 \sin k_x + m^{(I)}\nu_3\tau_1\sigma_0, \quad (4.13)$$

where $\Delta > 0$ is the superconducting order parameter and $m^{(I)} \rightarrow \infty$ the mass gap in the insulating region. Both the superconductor and the insulator satisfy inversion symmetry,

$$\mathcal{H}^{(S,I)}(\mathbf{k}) = \tau_1 \mathcal{H}^{(S,I)}(-\mathbf{k}) \tau_1, \quad (4.14)$$

characteristic of superconducting order with even inversion parity, and time-reversal symmetry,

$$\mathcal{H}^{(S,I)}(\mathbf{k}) = \sigma_2 \mathcal{H}^{(S,I)}(-\mathbf{k})^* \sigma_2. \quad (4.15)$$

To describe the heterostructure with an x -dependent Hamiltonian, we replace k_x by $-i\partial_x$ and linearize the Hamiltonians $\mathcal{H}^{(W)}$, $\mathcal{H}^{(S)}$, and $\mathcal{H}^{(I)}$ in k_x . In this way, we obtain the Hamiltonian

$$\mathcal{H} = -it\nu_3\tau_3\sigma_1\partial_x + \mathcal{M}(x), \quad (4.16)$$

where

$$\mathcal{M}(x) = \mathcal{M}^{(S)} \equiv \Delta\nu_1\sigma_0, \quad (4.17a)$$

for $x < 0$,

$$\mathcal{M}(x) = \mathcal{M}^{(W)} \equiv t\nu_3\tau_3\sigma_2 \sin k_y + m(k_y, k_z)\nu_3\tau_1\sigma_0 + \beta\nu_0\sigma_3 - \mu\nu_3\sigma_0, \quad (4.17b)$$

for $0 < x < W$, and

$$\mathcal{M}(x) = \mathcal{M}^{(I)} \equiv m^{(I)}\nu_3\tau_1\sigma_0, \quad (4.17c)$$

for $x > W$, respectively. Here

$$m(k_y, k_z) = m_0 + t'(1 - \cos k_y) + t'_z(1 - \cos k_z), \quad (4.18)$$

is the linearized mass term in the normal region.

4.2.3 Block diagonalization, chirality, Fermi arcs

A unitary transformation can be used to bring the Hamiltonian to a block-diagonal form. Labeling the two blocks by the parameter $\tau = \pm 1$, the transformation reads

$$\mathcal{H}_\tau = [U \mathcal{H} U^\dagger]_\tau, \quad U = e^{i(\pi/4)\nu_0\tau_2\sigma_3}. \quad (4.19)$$

The transformation acts non trivially only on the mass term, which transforms as

$$[U\nu_3\tau_1\sigma_0U^\dagger]_\tau = \tau\nu_3\sigma_3, \quad (4.20)$$

while the transformation of the other terms simply replaces τ_3 by τ . After the unitary transformation from Eq. (4.19) the diagonal blocks of the Hamiltonian, Eq. (4.16), then read

$$\mathcal{H}_\tau = -it\tau\nu_3\sigma_1\partial_x + \mathcal{M}_\tau(x), \quad (4.21)$$

with $\mathcal{M}_\tau(x) = \mathcal{M}^{(S)}$, given by Eq. (4.17a), for $x < 0$, $\mathcal{M}(x) = \mathcal{M}_\tau^{(W)}$,

$$\mathcal{M}_\tau^{(W)} = t\tau\nu_3\sigma_2 \sin k_y + m(k_y, k_z)\tau\mu_3\sigma_3 - \mu\nu_3\sigma_0 + \beta\nu_0\sigma_3, \quad (4.22)$$

for $0 < x < W$, and $\mathcal{M}(x) = \mathcal{M}_\tau^{(I)}$,

$$\mathcal{M}_\tau^{(I)} = m^{(I)}\tau\nu_3\sigma_3, \quad (4.23)$$

for $x > W$. In the transformed basis, inversion, time-reversal, particle-hole conjugation, and the mirror antisymmetry shown in Eq. (4.4) are represented as $\tau_3\sigma_3$, $\tau_2\sigma_1K$, $\nu_2\tau_2\sigma_1K$, and $\sigma_2\tau_3$, respectively.

After the unitary transformation, the Weyl nodes are found in the blocks $\tau = -1$ for electrons and $\tau = +1$ for holes, respectively. Expanding $\mathcal{H}_\tau^{(W)}$ around the Weyl nodes in the form $\sum_i v_i\sigma_i(k_i - K_i)$, where K_i is the node position, we can identify the chirality $\chi = \text{sign}(v_1v_2v_3)$. For our convention that all model parameters are positive, $\chi = \mp$ for the node at $k_z = \pm k_0$ for both electrons and holes, as indicated for electrons in Fig. 4.1.

To find Fermi-arc surface states at the interface with the trivial insulator at $x = W$, we consider electron and hole eigenstates of the insulator that decay for $x > W$, taken at $x = W$,

$$\psi_{e/h}(W) = a_{e/h} \begin{pmatrix} 1 \\ i \end{pmatrix}, \quad (4.24)$$

with normalization coefficients $a_{e/h}$ that have to be determined separately. For the normal region $x < W$ we use the Ansatz

$$\psi_{e/h}(x) = a_{e/h} \begin{pmatrix} 1 \\ i \end{pmatrix} e^{\alpha(x-W)}. \quad (4.25)$$

The decay coefficient $\alpha > 0$ and the energy ε can be found by insertion of the Ansatz of Eq. (4.25) into the Bogoliubov-de Gennes equation

$$[\mathcal{H}_\tau^{(W)} - \varepsilon] \begin{pmatrix} \psi_e(x) \\ \psi_h(x) \end{pmatrix} = 0. \quad (4.26)$$

For $\tau = -1$ we find an electron-like solution with $\alpha = \beta - m(k_y, k_z)$ and energy

$$\varepsilon_e(k_y, k_z) = -t \sin k_y - \mu. \quad (4.27)$$

For $\tau = +1$, the solution is hole-like and has energy

$$\varepsilon_h(k_y, k_z) = -t \sin k_y + \mu. \quad (4.28)$$

Both solutions move in the y direction with velocity $v_F = d\varepsilon_{e/h}/dk_y = -t \cos k_y$, as illustrated (for electrons) in Fig. 4.1. For small k_y the condition $\alpha > 0$ is satisfied for $|k_z| < k_0$, *i.e.*, for k_z between the two Weyl points.

4.3 Equilibrium current

Superconductor–normal-metal heterostructures with a magnetic N region are known to exhibit an equilibrium current in the direction of $\mathbf{E} \times \mathbf{B}$, where here the role of the time-reversal breaking (magnetic) field \mathbf{B} is played by the exchange field (described by the term proportional to β in $\mathcal{H}^{(W)}$ and here pointing in the z direction) and the role of the inversion-symmetry breaking (electric) field \mathbf{E} is played by a confinement-potential gradient of the interface (here in the x direction) [155]. In our geometry we thus expect to find an equilibrium current in the y direction.

4.3.1 Scattering formulation

We calculate the equilibrium current density I_y as the derivative of the ground state energy E to the vector potential A_y . The vector potential A_y enters the Bogoliubov-de Gennes Hamiltonian \mathcal{H} of Eq. (4.16) via the standard substitution $k_y \rightarrow k_y - \nu_3 e A_y$. Then the equilibrium current I_y is

$$\begin{aligned} I_y &= \frac{1}{2} \sum_{\tau} \int_{-\infty}^0 d\varepsilon \varepsilon \frac{\partial}{\partial A_y} \frac{dN_{\tau}(\varepsilon)}{d\varepsilon} \\ &= -\frac{1}{2} \sum_{\tau} \int_{-\infty}^0 d\varepsilon \frac{\partial N_{\tau}(\varepsilon)}{\partial A_y}, \end{aligned} \quad (4.29)$$

where $dN_{\tau}(\varepsilon)/d\varepsilon$ is the density of states of the Hamiltonian \mathcal{H}_{τ} of Eq. (4.21) and $N_{\tau}(\varepsilon)$ is the cumulative density of states.

The density of states $dN_{\tau}(\varepsilon)/d\varepsilon$ is a sum of delta-function contributions for $|\varepsilon| < \Delta$ and continuous otherwise. In principle, $dN_{\tau}(\varepsilon)/d\varepsilon$ may depend on A_y in both the discrete and continuous parts of the spectrum [158]. To capture both contributions, we adopt a procedure used by Brouwer and Beenakker for the calculation of the Josephson effect in a chaotic quantum dot [159]. Following Ref. [159], we determine $N_{\tau}(\varepsilon)$ by matching solutions of the Bogoliubov-de Gennes equation $\mathcal{H}_{\tau}\psi = \varepsilon\psi$ in the superconducting region $x < 0$ and in the normal region $x > 0$. To this end, we insert an “ideal lead” between the superconducting region at $x < 0$ and the normal region at $x > 0$, described by the Hamiltonian of Eq. (4.21) with $\mathcal{M}_{\tau} = 0$. At the end of the calculation, the length of the ideal lead is sent to zero. In the ideal lead, the Bogoliubov-de Gennes equation is solved by the scattering states

$$\psi_{\tau;\nu,\pm}(x) = e^{\pm i\varepsilon x/t} |\nu, \pm\nu\tau\rangle, \quad (4.30)$$

where $|\nu, \sigma\rangle$ with $\nu, \sigma = \pm 1$ is an eigenspinor of ν_3 at eigenvalue ν and of σ_1 at eigenvalue σ . The eigenstates $\psi_{\tau;\nu,+}$ and $\psi_{\tau;\nu,-}$ represent solutions moving in the positive and negative x directions, respectively. The solutions with $\nu = 1$ are electron-like; the eigenstates with $\nu = -1$ are hole-like.

In the ideal-lead segment around $x = 0$, the full solution of the Bogoliubov-de Gennes equation is a linear combination of the scattering states given in Eq. (4.30),

$$\psi_\tau(x) = \sum_\nu [a_{\tau,\nu}\psi_{\tau;\nu,+}(x) + b_{\tau,\nu}\psi_{\tau;\nu,-}(x)]. \quad (4.31)$$

Viewing the coefficients $a_{\tau,\nu}$ and $b_{\tau,\nu}$ as amplitudes of quasiparticles incident on and reflected from the normal region, respectively, we may relate them via the scattering matrix $S_\tau(\varepsilon)$ of the normal region,

$$\begin{pmatrix} b_{\tau,+} \\ b_{\tau,-} \end{pmatrix} = S_\tau(\varepsilon) \begin{pmatrix} a_{\tau,+} \\ a_{\tau,-} \end{pmatrix}. \quad (4.32)$$

(The dependence of $S_\tau(\varepsilon)$ on k_y and k_z is kept implicit.) When seen from the superconductor, the coefficients a_ν represent the reflected amplitudes, whereas the coefficients b_ν represent the incident amplitude, so that one has the relation

$$\begin{pmatrix} a_{\tau,+} \\ a_{\tau,-} \end{pmatrix} = S_\tau^{(S)}(\varepsilon) \begin{pmatrix} b_{\tau,+} \\ b_{\tau,-} \end{pmatrix}, \quad (4.33)$$

where $S_\tau^{(S)}(\varepsilon)$ is the scattering matrix of the superconducting region. Upon combining Eqs. (4.32) and (4.33), one finds that nontrivial solutions of the Bogoliubov-de Gennes equation exist only if

$$\det[1 - S_\tau(\varepsilon)S_\tau^{(S)}(\varepsilon)] = 0. \quad (4.34)$$

Since $S_\tau(\varepsilon)$ and $S_\tau^{(S)}(\varepsilon)$ are analytic functions of ε in the upper half of the complex plane, we may directly obtain the cumulative density of states $N_\tau(\varepsilon)$ as [159]

$$\begin{aligned} N_\tau(\varepsilon) = & -\frac{1}{\pi} \int \frac{dk_y dk_z}{(2\pi)^2} \text{Im} \left\{ \ln \det[1 - S_\tau(\varepsilon^+)S_\tau^{(S)}(\varepsilon^+)] \right. \\ & \left. - \frac{1}{2} \ln[\det(S_\tau(\varepsilon))] - \frac{1}{2} \ln[\det(S_\tau^{(S)}(\varepsilon))] \right\}, \end{aligned} \quad (4.35)$$

where $\varepsilon^+ = \varepsilon + i\eta$, η being a positive infinitesimal.

The second and third terms between the brackets in Eq. (4.35) do not contribute to the current after integration to k_y . The first term in Eq. (4.35) is analytic in the upper half of the complex plane and vanishes for $\text{Im } \varepsilon \rightarrow \infty$. Shifting the integration along the negative real axis to the positive imaginary axis, we then find

$$I_y = \int \frac{dk_z}{2\pi} \mathcal{I}_y(k_z), \quad (4.36)$$

where

$$\mathcal{I}_y(k_z) = -\frac{1}{2\pi} \sum_\tau \int \frac{dk_y}{2\pi} \text{Re} \int_0^\infty d\omega \frac{\partial}{\partial A_y} \ln \det[1 - S_\tau(i\omega)S_\tau^{(S)}(i\omega)]. \quad (4.37)$$

Under particle-hole conjugation, the basis state $\psi_{\tau;\nu,\pm}(x)$ of Eq. (4.30) is mapped to $\mp\psi_{-\tau;-\nu,\pm}(x)$, while simultaneously inverting $\varepsilon \rightarrow -\varepsilon$ and $k_{y,z} \rightarrow -k_{y,z}$, and vice versa. For this choice of the scattering states, particle-hole symmetry imposes the condition

$$S_{\tau}(\varepsilon; k_y, k_z) = -\nu_1 S_{-\tau}^*(-\varepsilon; -k_y, -k_z) \nu_1. \quad (4.38)$$

Calculating the scattering matrix $S^{(S)}$ of the superconductor one obtains

$$S_{\tau}^{(S)}(\varepsilon) = e^{-i\gamma(\varepsilon)} \nu_1, \quad \gamma = \arccos(\varepsilon/\Delta), \quad (4.39)$$

which is the standard result for Andreev reflection off an s -wave spin-singlet superconductor [18]. The scattering matrix $S_{\tau}(\varepsilon)$ of the normal region is diagonal with respect to the particle-hole index ν ,

$$S_{\tau}(\varepsilon; k_y, k_z) = \begin{pmatrix} r_{\tau}(\varepsilon; k_y, k_z) & 0 \\ 0 & -r_{-\tau}(-\varepsilon; -k_y, -k_z)^* \end{pmatrix}, \quad (4.40)$$

where $r_{\tau}(\varepsilon; k_y, k_z)$ is the reflection amplitude for electron-like quasiparticles. Inserting Eqs. (4.39) and (4.40) into Eq. (4.37) and performing a partial integration to k_y , we find

$$\begin{aligned} \mathcal{I}_y(k_z) &= \frac{2e}{\pi} \int \frac{dk_y}{2\pi} \text{Re} \int_0^{\infty} d\omega \frac{\partial r_{+}(i\omega; k_y, k_z)}{\partial k_y} \\ &\quad \times \frac{r_{-}(i\omega; -k_y, -k_z)^*}{e^{2i\gamma(i\omega)} + r_{+}(i\omega; k_y, k_z) r_{-}(i\omega; -k_y, -k_z)^*}. \end{aligned} \quad (4.41)$$

Because of the mirror antisymmetry at $\mu = 0$ given in Eq. (4.4), the reflection amplitudes satisfy $r_{\tau}(\varepsilon; k_y, k_z) = r_{\tau}(\varepsilon; -k_y, k_z)^*$, from which it follows that the current vanishes at $\mu = 0$. We use this feature of our model to focus our calculation on the derivative $d\mathcal{I}_y(k_z)/d\mu$ at small μ .

4.3.2 Reflection amplitudes of normal region

We calculate the reflection amplitude r_{τ} by expressing it in terms of the reflection and transmission amplitudes $r_{\tau}^{(W)}$, $r'_{\tau}{}^{(W)}$, $t_{\tau}^{(W)}$, and $t'_{\tau}{}^{(W)}$ of the normal region $0 < x < W$ and the reflection phase $i\tau$ of the insulator at $x > W$,

$$r_{\tau} = r_{\tau}^{(W)} + \frac{i\tau t'_{\tau}{}^{(W)} t_{\tau}^{(W)}}{1 - i\tau r'_{\tau}{}^{(W)}}. \quad (4.42)$$

In this notation, the unprimed amplitudes $r_{\tau}^{(W)}$ and $t_{\tau}^{(W)}$ refer to reflection and transmission from the normal region for particles incident at the interface with the superconductor (S), whereas the primed amplitudes $r'_{\tau}{}^{(W)}$ and $t'_{\tau}{}^{(W)}$ are for particles

incident at the interface with the trivial insulator (I). Solving the scattering problem with the Hamiltonian of Eq. (4.21), we find the explicit expressions

$$\begin{aligned} r_\tau^{(\text{W})}(\varepsilon; k_y, k_z) &= r'_\tau{}^{(\text{W})}(\varepsilon; -k_y, -k_z) \\ &= i\tau \frac{m(k_y, k_z) + \beta\tau - it\tau \sin k_y}{t\kappa_\tau \coth(\kappa_\tau W) - i(\varepsilon + \mu)}, \end{aligned} \quad (4.43)$$

$$\begin{aligned} t_\tau^{(\text{W})}(\varepsilon; k_y, k_z) &= t'_\tau{}^{(\text{W})}(\varepsilon; -k_y, -k_z) \\ &= \frac{t\kappa_\tau / \sinh(\kappa_\tau W)}{t\kappa_\tau \coth(\kappa_\tau W) - i(\varepsilon + \mu)}, \end{aligned} \quad (4.44)$$

where we abbreviated

$$\kappa_\tau^2 t^2 = d_\tau(k_x, k_y)^2 - (\varepsilon + \mu)^2, \quad (4.45)$$

with

$$d_\tau(k_y, k_z) = \sqrt{t^2 \sin^2 k_y + (\beta + \tau m(k_y, k_z))^2}, \quad (4.46)$$

the gap in the k_z -dependent spectrum of the Hamiltonian shown in Eq. (4.21), see Eq. (4.5). The symmetry relation between primed and unprimed reflection and transmission amplitudes is a consequence of the inversion symmetry from Eq. (4.15).

To evaluate the k_z -resolved current density $\mathcal{I}_y(k_z)$, it is convenient to consider the three-dimensional Hamiltonian $\mathcal{H}(k_x, k_y, k_z)$ as family of two-dimensional Hamiltonians $\mathcal{H}(k_x, k_y)$ that parametrically depend on k_z . The two-dimensional Hamiltonian $\mathcal{H}^{(\text{W})}(k_x, k_y)$ describes a trivial (two-dimensional) insulator if $\beta < m_0$ or if $m_0 < \beta < m_0 + 2t'_z$ and $|k_z| > k_0$, see Eqs. (4.6)–(4.8). It describes a (two-dimensional) topologically nontrivial Chern insulator if $m_0 < \beta < m_0 + 2t'_z$ and $|k_z| < k_0$ or if $\beta > m_0 + 2t'_z$.

For the calculation of the equilibrium current I_y , we find it convenient to parametrize the reflection amplitudes $r_\tau^{(\text{W})}$, and $r'_\tau{}^{(\text{W})}$ in terms of the transmission coefficient $T_\tau = |t_\tau^{(\text{W})}|^2$ and the phase shifts ϕ_τ and ϕ'_τ ,

$$\begin{aligned} r_\tau^{(\text{W})} &= i\tau \sqrt{1 - T_\tau} e^{i\phi_\tau}, \\ r'_\tau{}^{(\text{W})} &= i\tau \sqrt{1 - T_\tau} e^{i\phi'_\tau}. \end{aligned} \quad (4.47)$$

Expressions for the reflection phases ϕ_τ and ϕ'_τ can be obtained from Eq. (4.43). For small k_y , ε , and μ , the reflection phase ϕ_+ of the high-energy band is well approximated by

$$\begin{aligned} \phi_+(k_y, k_z) &= \phi'_+(-k_y, -k_z) \\ &\approx (\varepsilon + \mu - k_y t) / d_+. \end{aligned} \quad (4.48)$$

The approximations for the reflection phase for the low-energy band for small k_y , ε , and μ are different for the trivial regime $\beta < m_0$ or $|k_z| > k_0$ and the topological regime $\beta > m_0 + 2t'_z$ or $|k_z| < k_0$,

$$\begin{aligned} \phi_-(k_y, k_z) &= \phi'_-(-k_y, -k_z) \\ &\approx \begin{cases} (\varepsilon + \mu + k_y t)/d_- & \text{trivial,} \\ \pi + (\varepsilon + \mu - k_y t)/d_- & \text{topological.} \end{cases} \end{aligned} \quad (4.49)$$

The fact that $\phi_- = \pi$ at $k_y = 0$ in the topological case is what causes the appearance of the Fermi-arc surface states near $k_y = 0$. With the parametrization defined in Eqs. (4.47), the reflection amplitude $r_\tau(\varepsilon; k_y, k_z)$ reads

$$r_\tau = i\tau e^{i\phi_\tau} \frac{e^{i\phi'_\tau} + \sqrt{1 - T_\tau}}{e^{i\phi'_\tau} \sqrt{1 - T_\tau} + 1}. \quad (4.50)$$

4.3.3 k_z -resolved current density for large W

We will now discuss the k_z -resolved current $\mathcal{I}_y(k_z)$ well inside the trivial and topological regimes, so that the two-dimensional Hamiltonian $\mathcal{H}^{(W)}(k_x, k_y)$ describes a gapped phase with a gap magnitude on the order of the band width. The case that k_z is in the vicinity of k_0 will be addressed in chapter 4.3.5.

For our calculation of $\mathcal{I}_y(k_z)$ we assume that the width W of the normal region is much larger than the lattice spacing (which is set to one). The energy scale corresponding to the inverse width, t/W , the pair potential Δ , and the chemical potential μ are considered to be much smaller than the band width $t \sim t' \sim t'_z$. The energy difference of the high- and low-energy bands, $2m_0$, is considered to be on the order of the band width.

With this hierarchy of energy and length scales, the energy dependence of the reflection amplitudes of the normal region may typically be neglected when compared to the energy dependence of the phase shift γ for Andreev reflection from the superconductor. Also, one has $\kappa_\tau W \gg 1$, so that transmission is exponentially suppressed, $T_\tau \downarrow 0$. Assuming continuity of the current with $T_\tau \downarrow 0$, which we discuss in more detail in chapter 4.3.8, we may set

$$r_\tau(i\omega; k_y, k_z) = i\tau e^{i\phi_\tau(k_y, k_z)}, \quad (4.51)$$

where the reflection phase $\phi_\tau(k_y, k_z)$ of the normal region is evaluated at $\varepsilon = 0$ since the energy dependence is dominated by the energy dependence of the reflection phase $e^{-i\gamma}$ of the superconductor. This approximation breaks down if $e^{i\phi'_\tau} = -1$, because then the denominator in Eq. (4.50) vanishes for $T_\tau \downarrow 0$ so that the energy dependence of $r_\tau(\varepsilon; k_y, k_z)$ becomes important, which occurs if a Fermi-arc state at the surface at $x = W$ crosses the Fermi level. This case will be discussed in Subsec.

4.3.4. With the approximation from Eq. (4.51), the ω -integration in Eq. (4.41) may then be performed, with the result

$$\mathcal{I}_y(k_z) = -\frac{e\Delta}{2} \int \frac{dk_y}{2\pi} \frac{\partial\phi_+}{\partial k_y} s(\phi) \sin(\phi/2), \quad (4.52)$$

where

$$\phi(k_y, k_z) = \phi_+(k_y, k_z) - \phi_-(-k_y, -k_z), \quad (4.53)$$

and $s(\phi) = \text{sign} \cos(\phi/2)$.

Effectively, the approximations used to derive Eq. (4.52) from the general result of Eq. (4.41) amount to restricting to contributions from the discrete part of the Andreev spectrum. (This approximation is known as the “short-junction limit” in the context of the Josephson effect.) To show that Eq. (4.52) represents the contribution from the discrete part of the Andreev spectrum, we note that, if we neglect the energy dependence of the reflection amplitudes from the normal region, Andreev bound states appear at discrete energies $\varepsilon_{\pm}(k_y, k_z)$ satisfying the quantization condition

$$e^{-i2\gamma(\varepsilon_{\pm})} e^{i\phi_+(k_y, k_z)} e^{i\phi_-(-k_y, -k_z)} = 1. \quad (4.54)$$

Solving for $\varepsilon_{\pm}(k_y, k_z)$, one finds

$$\varepsilon_{\pm}(k_y, k_z) = \pm\Delta \cos(\phi/2). \quad (4.55)$$

The current associated with a single Andreev level is $\partial\varepsilon_{\pm}(k_y, k_z)/\partial A_y$. To find the total current we integrate over the contributions from all Andreev levels with energy $\varepsilon_{\pm}(k_y, k_z) < 0$,

$$\mathcal{I}_y(k_z) = \frac{1}{2} \sum_{\pm} \int \frac{dk_y}{2\pi} \frac{\partial\varepsilon_{\pm}}{\partial A_y} \Theta(-\varepsilon_{\pm}), \quad (4.56)$$

where the Heaviside function $\Theta(x) = 1$ if $x > 0$ and 0 otherwise. Upon substitution of Eq. (4.55) for ε_{\pm} , one recovers Eq. (4.52).

To find the derivative $d\mathcal{I}_y(k_z)/d\mu$ (recall that $\mathcal{I}_y(k_z) = 0$ for $\mu = 0$, see the discussion at the end of chapter 4.3.1) we observe that from Eq. (4.43) we have

$$\frac{\partial\phi_{\tau}}{\partial\mu} = \frac{1}{d_{\tau}}, \quad (4.57)$$

where the gap $d_{\tau}(k_y, k_z)$ was defined in Eq. (4.46). For the μ -derivative of the k_z -resolved current $\mathcal{I}_y(k_z)$ we then find a “regular” contribution and a “singular” contribution, which follows from the derivative of the discontinuity of the step function $s(\phi)$ at $\phi = \pi \pmod{2\pi}$,

$$\frac{d\mathcal{I}_y(k_z)}{d\mu} = \frac{d\mathcal{I}_y(k_z)^{(r)}}{d\mu} + \frac{d\mathcal{I}_y(k_z)^{(s)}}{d\mu}, \quad (4.58)$$

with

$$\frac{d\mathcal{I}_y(k_z)^{(r)}}{d\mu} = -\frac{e\Delta}{4} \int \frac{dk_y}{2\pi} \left[\left(\frac{1}{d_+} - \frac{1}{d_-} \right) \frac{\partial\phi_+}{\partial k_y} \cos \frac{\phi}{2} - \frac{2}{d_+^2} \frac{\partial d_+}{\partial k_y} \sin \frac{\phi}{2} \right] s(\phi), \quad (4.59)$$

$$\frac{d\mathcal{I}_y(k_z)^{(s)}}{d\mu} = e\Delta \int \frac{dk_y}{2\pi} \frac{\partial\phi_+}{\partial k_y} \left(\frac{1}{d_+} - \frac{1}{d_-} \right) \delta(\phi - \pi), \quad (4.60)$$

where the delta function should be periodically extended with period 2π . In the limit of a large exchange field β , d_- is much smaller than d_+ and one may further approximate $d\mathcal{I}_y(k_z)/d\mu$ by restricting to the terms inversely proportional to d_- .

On the basis of Eqs. (4.59) and (4.60) we can compare $d\mathcal{I}_y(k_z)/d\mu$ in the trivial and topological regimes. The phases ϕ_+ and ϕ_- are shown vs. k_y for typical model parameters in Fig. 4.2(a) and (b). In the topologically trivial case, generically both ϕ_+ and ϕ_- have a weak k_y -dependence and ϕ remains close to zero. In this case, the singular contribution $[d\mathcal{I}_y(k_z)/d\mu]^{(s)}$ is absent. Considering the ‘‘regular’’ contribution shown in Eq. (4.59), we see that the dominant contribution to the total equilibrium current I_y comes from regions in which the gap d_- is smallest, which is in the vicinity of the Weyl points, *i.e.*, for $|k_z| \downarrow k_0$. The sign of the equilibrium current is determined by the derivative $d\phi_+/dk_y$ near $k_y = 0$.

In the topological case, as a result of the band inversion from the sign change of $\beta - m(k_y, k_z)$, the phase ϕ_- decreases by 2π upon going from $k_y = -\pi$ to $k_y = \pi$. Hence, the singularity in the integrand at $\phi = \pi \pmod{2\pi}$ cannot be avoided. This gives rise to the singular contribution $[d\mathcal{I}_y(k_z)/d\mu]^{(s)}$ of Eq. (4.60). Since ϕ_- is close to π in the vicinity of $k_y = 0$, the integrand in Eq. (4.60) has support precisely where the derivative $\partial\phi_+/\partial k_y$ is maximal, see Fig. 4.2(c). As a consequence, in the topological regime, the total current $d\mathcal{I}_y(k_z)/d\mu$ has larger magnitude and opposite sign when compared to the trivial regime, see Fig. 4.2(e).

To obtain an explicit expression for a special parameter choice well inside the topological regime, one may consider $k_z = 0$ and $\beta = m_0 + t'$, $t' = t$, in which case $\kappa_- = 1$ and $\phi_-(k_y, 0) \approx \pi - k_y$ for all k_y . Additionally assuming a large gap $d_+ \approx \beta + m_0 \gg t$, so that $\phi_+(k_y, 0) \approx -(t/(m_0 + \beta)) \sin k_y$, the current becomes

$$\frac{d\mathcal{I}_y(0)}{d\mu} \approx \frac{2e\Delta}{3\pi(\beta + m_0)}. \quad (4.61)$$

For the trivial case we consider the leading-order term in β/t , since the current vanishes at $\beta = 0$, and take $m_0 = t = t'$ and $k_z = 0$, which gives

$$\frac{d\mathcal{I}_y(0)}{d\mu} \approx -\frac{e\Delta\beta}{12\pi t^2}. \quad (4.62)$$

Comparing Eqs. (4.61) and (4.62) also shows the opposite signs of the equilibrium current in the two regimes.

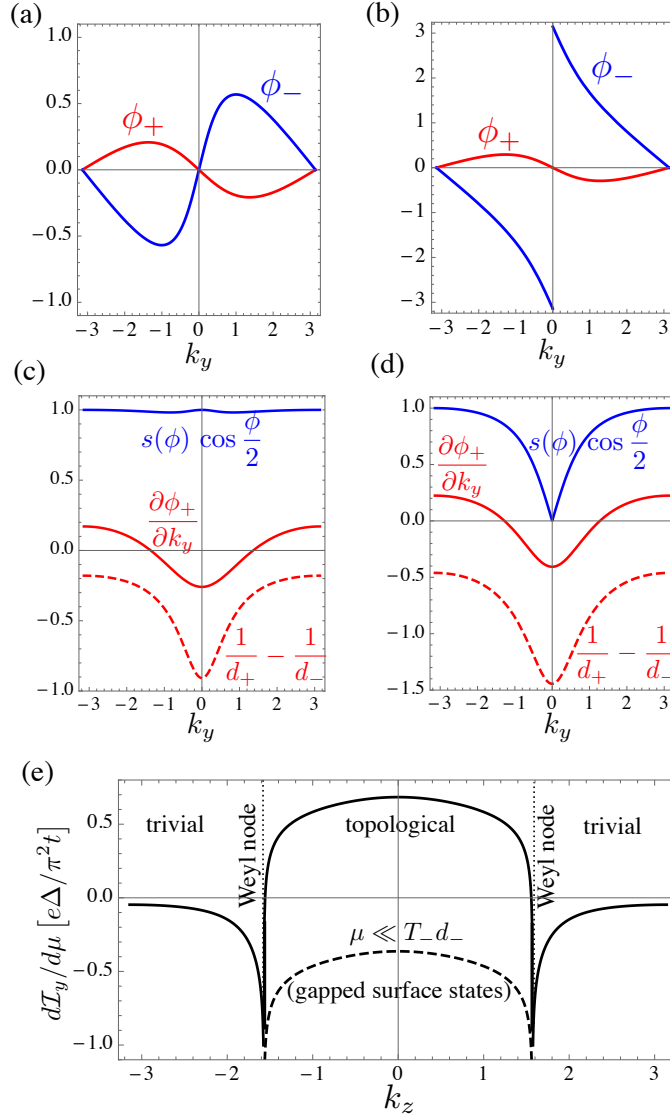


Figure 4.2: (a) and (b): Reflection phases $\phi_{\pm}(k_y, k_z)$ at chemical potential $\mu \rightarrow 0$ and energy $\varepsilon = 0$ (after first taking the limit $W \rightarrow \infty$) for parameter choices corresponding to the trivial (a) and topological (b) regimes. (c) and (d): Factors $s(\phi) \cos(\phi/2)$ (blue), $(t/d_+ - t/d_-)$ (dashed-red) and $\partial\phi_+/\partial k_y$ (solid-red) for the same parameter choices as in (a) and (b), respectively. (e): k_z -resolved equilibrium current $\mathcal{I}_y(k_z)$ as a function of k_z from Eq. (4.58) (solid curve). The sign of the current changes if k_z goes from the topological region (k_z between the Weyl nodes at $\pm k_0$) to the trivial region. The dashed line shows the result at ultrasmall chemical potential within the finite-size gap of surface states, see Eq. (4.65). The parameters are $m_0 = 0.5 t$, $\beta = 1.5 t$, $t = t' = t'_z = 1$. In panels (a) and (c) we further set $k_z = 1$; in panels (b) and (d) we set $k_z = 2.6$.

4.3.4 Finite-size effects

For small transmission coefficient T_- of the low energy band, the presence of the Fermi-arc states at the interface with the trivial insulator at $x = W$ causes a narrow resonance in the reflection amplitude $r_-(\varepsilon; k_y, k_z)$. This resonance occurs, when the denominator in Eq. (4.50) is approximately zero, $e^{i\phi'_\tau} \approx -1$. In this case, the assumption that the energy dependence of $r_-(\varepsilon; k_y, k_z)$ can be neglected when compared to the energy dependence of the Andreev reflection phase $e^{-i\gamma(\varepsilon)}$ is obviously violated, despite the fact that the gap $d_- \gg \Delta$.

For the minimal model we consider in this article, this issue affects the topological regime $\beta > m_0$, $|k_z| < k_0$ only. Here we consider the case of small $\mu \ll t$, so that the resonance appears in the vicinity of $k_y = 0$. For small transmission coefficient T_- , the full reflection amplitude r_- of Eq. (4.50) may then be well approximated as

$$r_- = -ie^{i\phi_-} w(k_y t + \varepsilon + \mu), \quad (4.63)$$

with

$$w(\varepsilon) = \frac{2\varepsilon - iT_- d_-}{2\varepsilon + iT_- d_-}. \quad (4.64)$$

Since $w(k_y t + i\omega + \mu) \approx 1$ if $|k_y t + i\omega + \mu| \gtrsim T_- d_-$, the presence of the factor $w(k_y t + i\omega + \mu)$ has little effect on the integrand in Eq. (4.41) in the limit of small transmission T_- if $\mu \gg T_- d_-$, except for a small integration region around $k_y t \approx -\mu$ and $\omega \lesssim T_- d_-$. Because of the smallness of the integration region in which w significantly differs from unity, the net finite-size effect on $d\mathcal{I}_y(k_z)/d\mu$ after integration over k_y and ω is small and goes to zero if $T_- \rightarrow 0$. For $\mu \lesssim T_- d_-$ this conclusion cannot be drawn, however, because the singularity in the fraction in Eq. (4.64) coincides with the singularity of the integrand in $d\mathcal{I}_y(k_z)/d\mu$, which led to the singular contribution shown in Eq. (4.60).

To analyze this limit of “ultrasmall” chemical potential μ in further detail, we observe that the singular contributions of the integration in Eq. (4.41) from the vanishing of the denominator and from the finite-size factor $w(k_y t + i\omega + \mu)$ are limited to a small interval $-\delta < k_y < \delta$ around $k_y = 0$, where $\delta \ll 1$ may be chosen large enough that $w(\pm\delta t + \mu + i\omega) \approx 1$. It follows that the “regular” contribution of Eq. (4.59) to $d\mathcal{I}_y(k_z)/d\mu$, which is associated with momenta k_y outside this interval, is unaffected by the finite-size effects. On the other hand, as we show in detail in chapter 4.3.7, upon inclusion of the finite-size effects the integrand of the singular contribution $d\mathcal{I}_y(k_z)^{(s)}/d\mu$ is multiplied by a negative factor $-(d_+ + d_-)/(d_+ - d_-)$, when compared to the result given in Eq. (4.60) for $\mu \gg T_- d_-$. Hence for ultrasmall chemical potential $\mu \ll T_- d_-$ we find

$$\frac{d\mathcal{I}_y(k_z)}{d\mu} = \frac{d\mathcal{I}_y(k_z)^{(r)}}{d\mu} + \frac{d\mathcal{I}_y(k_z)^{(s)}}{d\mu}, \quad (4.65)$$

with $[d\mathcal{I}_y(k_z)/d\mu]^{(r)}$ given by Eq. (4.59) and

$$\frac{d\mathcal{I}_y(k_z)^{(s)}}{d\mu} = e\Delta \int \frac{dk_y}{2\pi} \frac{\partial\phi_+}{\partial k_y} \left(\frac{1}{d_+} + \frac{1}{d_-} \right) \delta(\phi - \pi). \quad (4.66)$$

The sign change of the singular contribution leads to a significant *reduction* of the equilibrium current in the case of an ultrasmall chemical potential $\mu \ll T_-d_-$, when compared to the case $\mu \gg T_-d_-$.

To obtain an order-of-magnitude estimate, we again set $k_z = 0$ and consider the well-established topological regime $\beta = m_0 + t'$, $t' = t$, $k_z = 0$, $\beta + m_0 \gg 1$, for which we find, that

$$\frac{d\mathcal{I}_y(0)}{d\mu} \approx -\frac{e\Delta}{3\pi(\beta + m_0)}, \quad (4.67)$$

if $\mu \ll T_-d_-$. Comparison to Eq. (4.61) shows that at ultrasmall chemical potential the equilibrium current is approximately $-1/2$ times the current at finite μ .

Physically, the energy $\sim T_-d_- \sim t e^{-2W}$ that separates the regimes of “ultrasmall” and “finite” μ , is associated with the finite-size gap of the Fermi-arc surface states, whose wavefunctions decay exponentially away from the surfaces. Based on our result that in the topological regime the equilibrium current is strongly modified when the chemical potential is inside this finite-size gap, we interpret the difference between the finite- μ and ultrasmall- μ limits as the contribution of the topological surface states to $d\mathcal{I}_y/d\mu$. The difference between the large- μ and small- μ limits involves the singular contribution $[d\mathcal{I}_y/d\mu]^{(s)}$ only. In the well-established topological regime the surface-state contribution assumes the value $2[d\mathcal{I}_y/d\mu]^{(s)}$, with $[d\mathcal{I}_y/d\mu]^{(s)}$ given in Eq. (4.60).

4.3.5 Total current density

The full equilibrium current density I_y involves the integral of $\mathcal{I}_y(k_z)$ over k_z . The k_z -resolved current density $\mathcal{I}_y(k_z)$ is calculated in chapter 4.3.3, for the case that the normal region is gapped at momentum k_z and that the gap $d_\tau \gg \Delta$. This condition is no longer satisfied for the low-energy band if k_z is in the immediate vicinity of the Weyl points, because $d_- \rightarrow 0$ there.

That the results of chapter 4.3.3 cease to be valid if d_- becomes small in comparison to Δ is also reflected in the expression in Eq. (4.58) for $d\mathcal{I}_y(k_z)/d\mu$, which diverges $\propto \Delta/d_-$ if $d_-/\Delta \rightarrow 0$. This divergence should be cut off for $d_- \sim \Delta$. To see this, we evaluate $d\mathcal{I}_y(k_z)/d\mu$ in the opposite limit $d_- \ll \Delta$, in which we may neglect the energy dependence of the Andreev reflection phase $e^{-i\gamma(\varepsilon)}$ and of the reflection amplitude r_+ of the high-energy band, but keep the full energy dependence of the reflection amplitude r_- of the low-energy band.

Starting point of our calculation is Eq. (4.41). Since r_- depends on energy ε and chemical potential μ through the combination $\varepsilon + \mu$ only, upon analytic continuation $\varepsilon \rightarrow i\omega$, one has $\partial r_-^*/\partial\mu = i\partial r_-^*/\partial\omega$. When calculating $d\mathcal{I}_y(k_z)/d\mu$, the integrand in Eq. (4.41) then is a total derivative to ω and we find

$$\frac{d\mathcal{I}_y(k_z)}{d\mu} = \frac{2e}{\pi} \int \frac{dk_y}{2\pi} \text{Re} \frac{\partial\phi_+}{\partial k_y} \frac{1}{e^{-i\phi} + 1}, \quad (4.68)$$

where, as before, $\phi(k_y, k_z) = \phi_+(k_y, k_z) - \phi_-(-k_y, -k_z)$. Using $\text{Re} 1/(e^{-i\phi} + 1) = 1/2 - \pi\delta(\phi - \pi)$ we find that $d\mathcal{I}_y(k_z)/d\mu \sim e\partial\phi_+/\partial k_y$, which is the same order-of-magnitude estimate as one would obtain from Eq. (4.58) by cutting off the small- d_- -divergence at $d_- \sim \Delta$. [We note that the condition $d_- \ll \Delta$ may not be fulfilled for all k_y simultaneously, so that, strictly speaking, the approximations leading to Eq. (4.68) do not apply to the full range of the k_y -integration. This, however, does not affect the order-of-magnitude estimate of $d\mathcal{I}_y(k_z)/d\mu \sim e\partial\phi_+/\partial k_y$ that follows from Eq. (4.68).]

We thus find that $d\mathcal{I}_y(k_z)/d\mu \sim e\partial\phi_+/\partial k_y$ is a regular function of k_z in the vicinity of the Weyl points at $k_z = \pm k_0$. Since the range of momenta k_z affected by the violation of the condition $d_\tau \gg \Delta$ is correspondingly small, we conclude that the contribution of the Weyl points to the total current $dI_y/d\mu$ is small and that one may obtain $dI_y/d\mu$ by integration of the k_z -resolved result of Eq. (4.58) for $d\mathcal{I}_y(k_z)/d\mu$, omitting the immediate vicinity of the Weyl points from the integration range.

4.3.6 Numerical results

In Fig. 4.3 we compare the k_z -resolved equilibrium current $d\mathcal{I}_y(k_z)/d\mu$ obtained directly from Eq. (4.41) with the approximation of Eq. (4.58). We find excellent agreement away from the Weyl points. We observe that $d\mathcal{I}_y(k_z)/d\mu$ has opposite signs for $\mu \ll T_-d_-$ and $\mu \gg T_-d_-$ in the topological regime (k_z between the Weyl points), while there is no difference between the cases of large and small μ in the trivial regime. Except for the finite-size effect at ultrasmall chemical potentials, we observe only a weak dependence on the width W of the normal region, which is bound to the small vicinity ($d_- \lesssim \Delta$) of Weyl nodes (data not shown).

Figure 4.4 shows the total current density $dI_y/d\mu$, see Eq. (4.36), as a function of the exchange field β . For comparison, the ultrasmall- μ limit and the difference between the cases of ultrasmall and finite μ are also shown (dashed curves in Fig. 4.4). The current vanishes at $\beta = 0$ because the system is time-reversal invariant there. Its magnitude increases with β in the trivial insulator regime $\beta < m_0$. Upon entering the Weyl-semimetal regime, $dI_y/d\mu$ receives an upturn due to the positive contribution of the Fermi arcs. In the weak Chern insulator regime $\beta > m_0 + 2t'_z$,

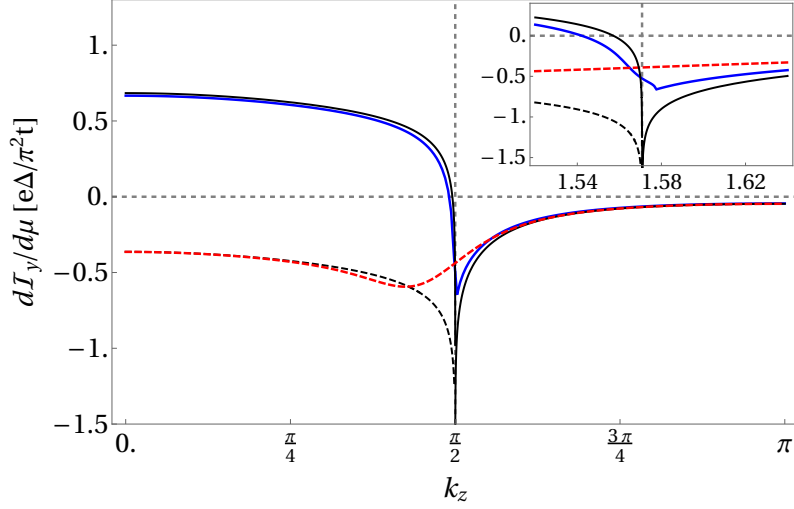


Figure 4.3: k_z -resolved equilibrium current $d\mathcal{I}_y/d\mu$. The superconducting gap $\Delta = 0.01 t$; the other parameters are the same as in Fig. 4.2. The solid-blue and dashed-red curves are obtained from Eq. (4.41) with finite chemical potential $\mu = 0.01 t$ and $\mu = 10^{-6} t$, respectively; The width of the normal region is $W = 300$ and $W = 5$, respectively. The solid- and dashed-black curves are obtained from Eqs. (4.58) and (4.65), respectively. The inset shows a closeup at the Weyl node at $k_0 \approx \pi/2$. The discontinuity in the derivative of $d\mathcal{I}_y/d\mu$ vs. k_z near k_0 is a finite-size effect and disappears upon further increasing W .

$dI_y/d\mu$ decreases upon (further) increasing β , but the difference between ultrasmall and finite chemical potential μ (dashed curve) persists.

To understand the apparent plateau in the Weyl-semimetal region $m_0 < \beta < m_0 + 2t'_2$ and the decrease with β in the Chern-insulator regime $\beta > m_0 + 2t'_z$, we note that the order of magnitude of the contribution of Fermi arcs (the difference between $dI_y/d\mu$ for $\mu \gg T_-d_-$ and $\mu \ll T_-d_-$) can be estimated from the difference of Eqs. (4.61) and (4.67), multiplying by the distance $2k_0$ between the Weyl points in the topological region,

$$\frac{dI_y^{\text{FA}}}{d\mu} \sim \frac{e\Delta k_0}{\beta + m_0}, \quad (4.69)$$

where one needs to set $k_0 = \pi$ in the Chern-insulator regime. The apparent plateau in the Weyl-semimetal regime appears, because the increase of the factor k_0 in the numerator with β is compensated by the increase of the denominator. In the Chern-insulator regime, the numerator in Eq. (4.69) is independent of β , whereas the denominator continues to increase with β , explaining the decrease of the current in the Chern-insulator regime. Note that k_0 has a singular dependence on β at the boundaries of the Weyl-semimetal regime at $\beta = m_0$ and $\beta = m_0 + 2t'_z$, see Eq. (4.7), which relates to the sharp upturns of the current. We verified that these sharp

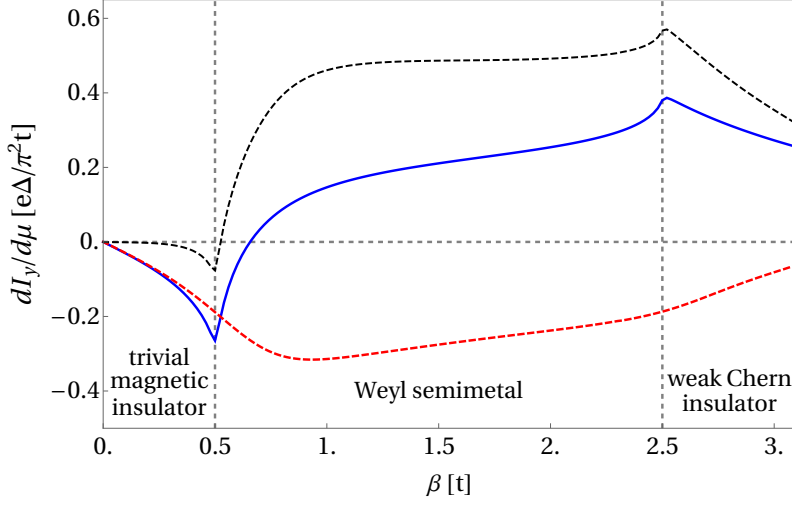


Figure 4.4: Equilibrium current $dI_y/d\mu$ as a function of the exchange field β . The solid-blue curve is for finite chemical potential $\mu = 0.01 t$ and width $W = 300$, which meets the condition $\mu \gg T_- d_-$ for most of reciprocal space. The dashed-red curve is for ultrasmall chemical potential $\mu = 10^{-6} t$ and width $W = 5$, which meets the condition $\mu \ll T_- d_-$ for most of reciprocal space. The black-dashed curve shows the difference of these two cases, which is the contribution to $dI_y/d\mu$ associated with the Fermi arcs. Other parameters are same as in Figs. 4.2 and 4.3.

features are eliminated if $dI_y/d\mu$ is considered as a function of the node separation $2k_0$ in the Weyl-semimetal regime (data not shown).

4.3.7 $[d\mathcal{I}_y(k_z)/d\mu]^{(s)}$ for $\mu \downarrow 0$

To show that the singular contribution to $d\mathcal{I}_y/d\mu$ changes sign in the limit $\mu \ll T_- d_-$ of an “ultrasmall” chemical potential (as compared to the case $\mu \gg T_- d_-$ of a “finite” chemical potential), we consider the regime of small k_y and μ in more detail. The equilibrium current for finite W is found from Eq. (4.41) by replacing $r_+ r_-^*$ by $-e^{i\phi} w^*$, where the function $w(\mu + i\omega - k_y t)$ is given in Eq. (4.64), and by restricting the k_y -integration to the interval $-\delta < k_y < \delta$,

$$\mathcal{I}_y(k_z)^{(s)} = \frac{2e}{\pi} \int_{-\delta}^{\delta} \frac{dk_y}{2\pi} \text{Im} \int_0^{\infty} d\omega \frac{\partial \phi_+}{\partial k_y} \frac{w^*}{e^{2i\gamma(\omega) - i\phi} - w^*}. \quad (4.70)$$

The integration boundaries $\pm\delta$ are chosen such that, on the one hand, $w \approx 1$ for $|k_y| = \delta$, whereas, on the other hand, $\delta \downarrow 0$ as $T_- \rightarrow 0$.

To find $[d\mathcal{I}_y(k_z)/d\mu]^{(s)}$, we have to differentiate the integrand in Eq. (4.70) with respect to μ . Using that for small k_y one has $\partial w/\partial \mu = -(1/t)\partial w/\partial k_y$ and $\partial \phi/\partial \mu = (1/d_+ - 1/d_-) = -(1/t)\partial \phi/\partial k_y - 2/d_-$ and using that ϕ_+ is an odd function of k_y

for $\mu \rightarrow 0$, so that we may treat $\partial\phi_+/\partial k_y$ as a constant inside the integration range $-\delta < k_y < \delta$, we obtain

$$\frac{d\mathcal{I}_y(k_z)^{(s)}}{d\mu} = \frac{2e}{\pi} \int_{-\delta}^{\delta} \frac{dk_y}{2\pi} \text{Im} \int_0^{\infty} d\omega \frac{\partial\phi_+}{\partial k_y} \left(-\frac{1}{t} \frac{d}{dk_y} - \frac{2}{d_-} \frac{\partial}{\partial\phi} \right) \frac{w^*}{e^{2i\gamma(\omega)-i\phi} - w^*}. \quad (4.71)$$

Since the first term between the brackets, which is proportional to d/dk_y , is a total derivative and since $w^* \approx 1$ at both ends of the integration domain, we may set $w^* \rightarrow 1$ in the integrand when evaluating the first term. This allows us to relate the first term to the equilibrium current at finite μ . Again using that $(1/t)\partial\phi/\partial k_y = -(1/d_+ + 1/d_-) = (d_+ + d_-)/(d_+ - d_-)\partial\phi/\partial\mu$, we recognize that the first term is $-(d_+ + d_-)/(d_+ - d_-)$ times the singular contribution of Eq. (4.60).

The second term between the brackets vanishes to leading order in Δ/d_- : To leading order in Δ/d_- the energy dependence in w^* can be neglected and the ω integration can be performed similarly as when going from Eq. (4.41) to Eq. (4.52) with the phase modified by w^* , which approaches 1 upon taking the limit $T_- \rightarrow 0$. The whole integrand is thus non-singular in this limit and, upon integration, the term vanishes for $T_- \rightarrow 0$ due to the vanishing integration range.

4.3.8 Continuity of the current in the limit $T_- \downarrow 0$

In a previous chapter we derived the current at the transmission amplitude set to zero from the beginning. Here we repeat the calculation in a more careful way, taking the limit $T_- \rightarrow 0$ at the end, to show that the current is a continuous function of T_- at $T_- = 0$. For simplicity we only consider the well-established topological regimes at $k_z = 0$, $\beta = m_0 + t$, and $t = t' = t'_z$. The goal is thus to reproduce Eqs. (4.61) and (4.67).

Starting point is Eq. (4.41), where we set $k_z = 0$,

$$\begin{aligned} \mathcal{I}_y(0) &= \frac{2e}{\pi} \int \frac{dk_y}{2\pi} \text{Re} \int_0^{\infty} d\omega \frac{\partial r_+(i\omega; k_y, 0)}{\partial k_y} \\ &\quad \times \frac{r_-(i\omega; -k_y, 0)^*}{e^{2i\gamma(i\omega)} + r_+(i\omega; k_y, 0)r_-(i\omega; -k_y, 0)^*}. \end{aligned} \quad (4.72)$$

We consider leading order in the gap $d_+ \approx \beta + m_0$ of the high-energy band, allowing to approximate $r_+^{(W)} = i \exp[-it \sin k_y / (\beta + m_0)]$ and leading to

$$\mathcal{I}_y(0) = \frac{2et}{\pi(\beta + m_0)} \int \frac{dk_y}{2\pi} \cos k_y \text{Re} \int_0^{\infty} d\omega \frac{r_-(i\omega; -k_y, 0)^*}{e^{2i\gamma(i\omega)} + ir_-(i\omega; -k_y, 0)^*}. \quad (4.73)$$

For the non-trivial band we take the full reflection amplitude of Eq. (4.50),

$$r_- = -ie^{i\phi_-} \frac{e^{i\phi'_-} + \sqrt{1-T}}{e^{i\phi'_-} \sqrt{1-T} + 1}, \quad (4.74)$$

where for brevity we have written T instead of T_- . In the well-established topological regime at $k_z = 0$, $\beta = m_0 + t$, and $t = t' = t'_z$, the reflection phase for the non-trivial band is $\phi_-(k_y, k_z) = \pi + \mu/t - k_y$. Further, we introduce $Z = \exp(-ik_y)$ and use $dk_y \cos k_y = idZ(1 + Z^2)/2Z^2$, as well as $\omega = \Delta \sinh \zeta$ and $d\omega = d\zeta \Delta \cosh \zeta$ (so that $e^{2i\gamma} = -e^{2\zeta}$) to obtain

$$\begin{aligned} \mathcal{I}_y(0) = & - \frac{\Delta e t}{\pi(\beta + m_0)\sqrt{1-T}} \text{Re} \int_0^\infty d\zeta \oint \frac{dZ}{2\pi i} \cosh \zeta \\ & \times \frac{i(e^{-i\mu/t} - \sqrt{1-T}Z)(1 + Z^2)}{Z(Z - Z_-)(Z - Z_+)}, \end{aligned} \quad (4.75)$$

where

$$Z_\pm = e^\zeta \frac{\pm i \sqrt{\sin^2(i\zeta - \mu/t) - T} + \cos(i\zeta - \mu/t)}{\sqrt{1-T}}. \quad (4.76)$$

The integration contour of Z is the unit circle in the complex plane enclosing two poles, one at $Z = 0$ and the other at $Z = Z_+$.

For $T = 0$ only the pole at $Z = 0$ contributes to the integral, due to cancellation of the $(Z - Z_+)$ term of the denominator with the first term of the numerator in Eq. (4.75), and it gives

$$\mathcal{I}_y^{(0)}(0) = - \frac{\Delta e t}{\pi(\beta + m_0)} \text{Im} \int_0^\infty d\zeta \cosh \zeta e^{-2\zeta - i\mu/t}, \quad (4.77)$$

which for $\mu \ll t$ evaluates to

$$\frac{d\mathcal{I}_y^{(0)}(0)}{d\mu} = \frac{2e\Delta}{3\pi(\beta + m_0)}, \quad (4.78)$$

reproducing Eq. (4.61).

For $T > 0$ both poles at $Z = 0$ and $Z = Z_+$ contribute to the integration. The contribution of the $Z = 0$ pole gives the same as the result Eq. (4.77) for $T = 0$ up to a factor of $1/\sqrt{1-T} \rightarrow 1$.

The contribution to the integral from the pole at $Z = Z_+$ is

$$\begin{aligned} \mathcal{I}_y^{(1)}(0) = & - \frac{e\Delta}{2\pi(\beta + m_0)} \text{Im} \int_0^\infty d\zeta g(i\zeta - \mu/t) \\ & \times [z(i\zeta - \mu/t) (1 + e^{2\zeta}) + z^{-1}(i\zeta - \mu/t) (1 + e^{-2\zeta})], \end{aligned} \quad (4.79)$$

where we abbreviated

$$g(i\zeta - \mu/t) = \frac{e^{-i\mu/t} - \sqrt{1-T}Z_+}{\sqrt{1-T}(Z_+ - Z_-)}, \quad (4.80)$$

$$z(i\zeta - \mu/t) = e^{-\zeta} Z_+. \quad (4.81)$$

(One verifies that g and z are functions of $i\zeta - \mu/t$ only.) Since it contributes for $T > 0$ only, the pole at Z_+ can be seen to represent a contribution to the equilibrium current from the Fermi arc at the insulating side of the semimetal. To estimate this contribution in the limit of small T , we note that the difference $Z_+ - Z_-$ is

$$Z_+ - Z_- = 2ie^\zeta \sqrt{\frac{\sin^2(i\zeta - \mu/t) - T}{1 - T}}. \quad (4.82)$$

To further evaluate this expression in the limit of small transmission T , we note that for $T \ll 1$ one has

$$Z_+ = e^{-i\mu/t} \left[1 - i\frac{T}{2} \cot(i\zeta - \mu/t) + \dots \right]. \quad (4.83)$$

In the limit of large ζ , this expansion is convergent and gives a numerator of order T in Eq. (4.79). Hence, for large ζ , the integral in Eq. (4.79) is convergent and of order T . If $\mu \neq 0$ this conclusion applies to the entire integration domain $\zeta > 0$, so that we conclude that the finite- T correction to the result shown in Eq. (4.77) is of order T and smoothly vanishes for $T \downarrow 0$ if $\mu \neq 0$. The case $\mu = 0$ is different because then the expansion shown in Eq. (4.83) is singular for $\zeta \rightarrow 0$. In the limit of small ζ one finds, if $\mu = 0$, that

$$\begin{aligned} g(i\zeta) &= -\frac{\sqrt{\zeta^2 + T} - \zeta}{2\sqrt{\zeta^2 + T}} \\ &= -\frac{T}{2\sqrt{\zeta^2 + T}(\sqrt{\zeta^2 + T} + \zeta)}. \end{aligned} \quad (4.84)$$

We now divide up the ζ integral into a region $0 < \zeta < T^{\alpha/4}$ and a region $T^\alpha < \zeta$ with $0 < \alpha < 1/2$. In the former region, the remaining factors of the integration are approximately constant and integration of Eq. (4.84) gives a contribution to $\mathcal{I}_y^{(1)}(0)$ that is of order \sqrt{T} . In the region $\zeta > T^\alpha$ one may still use the small- T expansion from Eq. (4.83) to arrive at a systematic expansion around the result at $T = 0$. Since both contributions to the integral vanish in the limit $T \rightarrow 0$, we conclude that $\mathcal{I}_y^{(1)}(0) \rightarrow 0$ for $T \rightarrow 0$ even if $\mu = 0$, although the convergence may be slower than for generic μ .

We now consider the derivative of Eq. (4.79) with respect to μ at $\mu = 0$ before taking the limit $T \rightarrow 0$. We use that $d/d\mu = (i/t)d/d\zeta$ acting on $z(i\zeta - \mu/t)$ and $g(i\zeta - \mu/t)$, to obtain

$$\begin{aligned} \frac{d\mathcal{I}_y^{(1)}(0)}{d\mu} &= -\frac{e\Delta}{2\pi(\beta + m_0)d_-} \operatorname{Re} \int_0^\infty d\zeta \left(1 + e^{2\zeta} \right) \\ &\quad \times \frac{d}{d\zeta} g(i\zeta) z(i\zeta) + \left(1 + e^{-2\zeta} \right) \frac{d}{d\zeta} \frac{g(i\zeta)}{z(i\zeta)}. \end{aligned} \quad (4.85)$$

Using

$$\lim_{T \rightarrow 0} \frac{g(0)}{z(0)} = \lim_{T \rightarrow 0} g(0)z(0) = -\frac{1}{2}, \quad (4.86)$$

partial integration gives,

$$\frac{d\mathcal{I}_y^{(1)}(0)}{d\mu} = -\frac{e\Delta}{\pi(\beta + m_0)} \left[1 - \text{Re} \int_0^\infty d\zeta \left(e^{2\zeta} g(i\zeta)z(i\zeta) - e^{-2\zeta} \frac{g(i\zeta)}{z(i\zeta)} \right) \right]. \quad (4.87)$$

The remaining integral vanishes for $T \rightarrow 0$ similarly as the current in (4.79) at $\mu = 0$ as shown above, hence

$$\frac{d\mathcal{I}_y^{(1)}(0)}{d\mu} = -\frac{e\Delta}{\pi(\beta + m_0)}. \quad (4.88)$$

Thus for the total current $\mathcal{I}_y^{(0)}(0) + \mathcal{I}_y^{(1)}(0)$ in the ordered limit $\mu \rightarrow 0$, $T \rightarrow 0$ we obtain

$$\frac{d\mathcal{I}_y(0)}{d\mu} = -\frac{e\Delta}{3\pi(\beta + m_0)}, \quad (4.89)$$

reproducing Eq. (4.67).

4.4 Discussion and conclusion

We have investigated the equilibrium current in a minimal model describing an SN heterostructure, where S is a conventional s -wave superconductor and, depending on the value of the exchange field β , the normal region (N) can be a magnetic insulator with a topologically trivial band structure, a Weyl semimetal with broken time-reversal symmetry, or a three-dimensional weak Chern insulator. The constituents of the heterostructure are microscopically inversion-symmetric, so that inversion symmetry is broken only by the heterostructure geometry. In all three regimes, time-reversal symmetry is broken by the exchange field.

In the trivial-insulator regime we find an equilibrium current that is proportional to the exchange field β at small β . It quantifies the interface current of a superconductor - magnetic insulator heterostructure, which is known to be generally possible in the presence of spin-orbit coupling. Previously such an equilibrium current has been predicted only for a system with interfacial Rashba spin-orbit coupling [155], instead of the intrinsic spin-orbit coupling considered here.

In the topological regime of a Weyl semimetal or a weak Chern insulator the current shows a qualitatively different behavior. Upon entering the topological regimes the β -dependence of the equilibrium current abruptly changes, causing a reversal of

the sign of the current well inside the topological regime. The decisive contribution comes from the topological surface states, which we can identify within a minimal model (motivated by materials of the Bi_2Se_3 family [112]) by comparing the equilibrium currents for a chemical potential inside and above the finite-size gap of the surface states. In contrast, the Weyl nodes of the bulk band structure, which the Fermi arcs connect, do not give a significant contribution to the equilibrium current.

That we find a large contribution of Fermi arcs and an insignificant contribution of Weyl nodes relates to previous studies which found that the bulk states of an inversion-symmetric, magnetic Weyl semimetal are mainly unaffected by superconductivity due to a “chirality blockade” [17]. Accordingly, we expect that this would change if the chirality blockade is lifted, which happens when at least one of the constituents of the heterostructure breaks the microscopic inversion symmetry [17]. In our model, the chirality blockade manifests itself through the fact that Andreev reflection from the superconductor switches quasiparticles between the topologically trivial high-energy band and the (potentially) topologically nontrivial low-energy band. It is this connection of the trivial and the nontrivial band by the superconducting pairing that also makes the magnitude of the equilibrium current non-universal in both the topologically trivial and nontrivial parameter regimes.

Whereas the “chirality blockade” prevents the bulk Weyl points to be strongly affected by the proximity superconductivity, Fermi-arc surface states at the interface with the superconductor, on the other hand, undergo a renormalization of their effective charge [156], which however is weak because of the chirality blockade. Relating the Fermi-arc current contribution of Eq. (4.69) to the charge renormalization of Fermi arcs one can interpret the former in terms of an uncompensated chiral current of surface states. Specifically, one can consider that each Fermi arc contributes to the current density

$$\frac{dI_y^{(\text{arc})}}{d\mu} = \text{sign}(v) \frac{k_0 q}{(2\pi)^2}, \quad (4.90)$$

where v is the velocity of the Fermi arc and q the effective charge. The Fermi-arc contribution to the current of the Fermi arcs is reproduced if the charge at the superconductor interface is renormalized to

$$q \sim -e \left[1 - \frac{\Delta}{(\beta + m_0)} \right], \quad (4.91)$$

while the charge of the opposite surface remains unaffected ($q = -e$). The sign of the Fermi-arc velocity has been discussed in chapter 4.2 and is illustrated in Fig. 4.1.

The contribution of Fermi arcs can be seen as a real-space counterpart to the superconductivity-enabled equilibrium chiral magnetic effect [15, 16], in which a

disbalance of chiral Landau levels of a pair of Weyl Fermions is produced by current- or flux-biased bulk superconductivity acting asymmetrically in momentum space on the chiral Landau levels. The fundamental connection of chiral Landau levels and Fermi arcs allows for the complementary effect that we just described. The differences between chiral Landau levels and Fermi arcs are that the latter continue to exist in zero magnetic field and are separated in real space. Our work shows that these differences can be used to realize the equilibrium chiral magnetic effect via the superconducting proximity effect, without flux or current bias, and at zero magnetic field.

Relevant materials where the Fermi-arc contribution to the equilibrium current should be important are magnetic Weyl semimetals, such as GdPtBi [160] and $\text{Co}_3\text{Sn}_2\text{S}_2$ [151]. Our work, however, also shows that the experimental detection of this effect is challenging because the equilibrium current is not exclusively due to Fermi arcs. The isolation of the Fermi-arc contribution that we could obtain in the minimal model (relying on an ultras-small chemical potential or an ultras-small, constant width of the Weyl semimetal, and mirror antisymmetry) does not seem to be experimentally realizable on the basis of existing materials. We believe, however, that characteristic signatures or other peculiar effects may be found in further studies of the equilibrium current, such as exploring its response to external magnetic fields.

5 Conclusion

In this thesis we have studied linearly dispersing electrons in systems of varying dimensionality and under the influence of disorder and a magnetic coupling. Linear dispersion relations appear in condensed matter systems and they lead to interesting physical phenomena due to their relativistic nature and also their connection to topology in condensed matter physics.

First, we studied the density of states at the nodal points of systems in two and three dimensions, graphene and Weyl semimetals, under the influence of disorder. These materials show vastly different behavior as the disorder strength is increased: In two dimensions any nonzero disorder strength immediately produces a finite density of states, whereas in three dimensions it remains zero until a critical disorder strength is reached. This sharp transition between a semimetallic and metallic regime in a Weyl semimetal is the subject of intense study and it remains unclear whether it is a true quantum phase transition or not. We compare high-precision numerical data with first- and second-order perturbation theory calculations. Our results speak in favor of the interpretation of this transition as a quantum phase transition, though further research into this question is necessary. For instance, other types of disorder, such as vector disorder, could be studied. One should also attempt to include the rare-region events in the disorder model, perhaps by allowing for more long-range disorder correlations.

The second system in question is a four-lead interferometer device made of helical edge states, which again feature a linear dispersion relation around a nodal point, where one of the edges is locally coupled to a magnet. We find that this time-reversal symmetry breaking coupling in combination with the interference of different electron paths through the interferometer gives rise to time-dependent currents even for time-independent bias voltages applied to the device, and also a strong suppression of the Aharonov-Bohm oscillations caused by a flux through the interferometer for small enough applied bias voltages. A future avenue worth pursuing would be to replace the magnet with an antiferromagnet, due to the fact that there are many known antiferromagnetic insulators (NiO, CoO, Cr₂O₃...), see Ref. [161] for a review on antiferromagnetic spintronics. Antiferromagnets also have a natural easy-plane anisotropy, an essential ingredient for the physics of our interferometer, and they typically have much higher precession frequencies compared to ferromagnets [161]. Similar interferometers without magnetic couplings have been already studied in

experiments [22, 23, 24], and as mentioned the more natural choice for experimental work would be an antiferromagnet.

Third and last we turn our attention to a layered heterostructure consisting of a finite-width Weyl semimetal slab in between the vacuum and a superconductor. Weyl semimetals have nodal points around which the dispersion of electrons is linear and also host linearly dispersing Fermi-arc surface states. We find that this heterostructure produces an equilibrium current along the interface with the superconductor and we can show that it is carried mostly by the Fermi-arc surface states by comparing different parameter regimes. We interpret this current as a real-space counterpart to the chiral magnetic effect, due to the superconductor acting asymmetrically on the two surfaces of the Weyl semimetal slab. In the future one could study similar layered heterostructures but with other types of superconducting couplings. One possibility would be to explore the consequence of a finite-momentum superconducting pairing or one that breaks inversion symmetry, both of which are not affected by the chirality blockade.

Bibliography

- [1] C. Herring. Accidental degeneracy in the energy bands of crystals. *Phys. Rev.*, 52:365, 1937.
- [2] S. Das Sarma, S. Adam, E. H. Hwang, and E. Rossi. Electronic transport in two-dimensional graphene. *Rev. Mod. Phys.*, 83(2):407–470, 2011.
- [3] A. H. Castro Neto, F. Guinea, N. M. R. Peres, K. S. Novoselov, and A. K. Geim. The electronic properties of graphene. *Rev. Mod. Phys.*, 81(1):109–162, 2009.
- [4] M. Z. Hasan and C. L. Kane. Colloquium: Topological insulators. *Rev. Mod. Phys.*, 82:3045, 2010.
- [5] J. Wang and S.-C. Zhang. Topological states of condensed matter. *Nat. Mater.*, 16(11):1062–1067, 2017.
- [6] N. P. Armitage, E. J. Mele, and A. Vishwanath. Weyl and Dirac semimetals in three dimensional solids. *Rev. Mod. Phys.*, 90:015001, 2018.
- [7] J. Bardeen and W. H. Brattain. The transistor, a semi-conductor triode. *Phys. Rev.*, 74:230–231, 1948.
- [8] B. D. Josephson. Possible new effects in superconductive tunnelling. *Phys. Lett.*, 1(7):251–253, 1962.
- [9] R. C. Jaklevic, J. Lambe, A. H. Silver, and J. E. Mercereau. Quantum interference effects in Josephson tunneling. *Phys. Rev. Lett.*, 12:159–160, 1964.
- [10] G. Binasch, P. Grünberg, F. Saurenbach, and W. Zinn. Enhanced magnetoresistance in layered magnetic structures with antiferromagnetic interlayer exchange. *Phys. Rev. B*, 39:4828–4830, 1989.
- [11] M. N. Baibich, J. M. Broto, A. Fert, F. Nguyen Van Dau, F. Petroff, P. Etienne, G. Creuzet, A. Friederich, and J. Chazelas. Giant magnetoresistance of (001)Fe/(001)Cr magnetic superlattices. *Phys. Rev. Lett.*, 61:2472–2475, 1988.
- [12] S. V. Syzranov and L. Radzihovsky. High-dimensional disorder-driven phenomena in Weyl semimetals, semiconductors, and related systems. *Annu. Rev. Condens. Matter Phys.*, 9(1):35–58, 2018.

- [13] P. G. Silvestrov, P. Recher, and P. W. Brouwer. Noiseless manipulation of helical edge state transport by a quantum magnet. *Phys. Rev. B*, 93:205130, 2016.
- [14] Q. Meng, S. Vishveshwara, and T. L. Hughes. Spin-transfer torque and electric current in helical edge states in quantum spin Hall devices. *Phys. Rev. B*, 90:205403, 2014.
- [15] T. E. O'Brien, C. W. J. Beenakker, and I. Adagideli. Superconductivity provides access to the chiral magnetic effect of an unpaired Weyl cone. *Phys. Rev. Lett*, 118:207701, 2017.
- [16] M. J. Pacholski, C. W. J. Beenakker, and I. Adagideli. Universal chiral magnetic effect in the vortex lattice of a Weyl superconductor. *Ann. Phys. (NY)*, 417:168103, 2020.
- [17] N. Bovenzi, M. Breitzkreiz, P. Baireuther, T. E. O'Brien, J. Tworzydło, I. Adagideli, and C. W. J. Beenakker. Chirality blockade of Andreev reflection in a magnetic Weyl semimetal. *Phys. Rev. B*, 96:035437, 2017.
- [18] A. F. Andreev. The thermal conductivity of the intermediate state in superconductors. *Zh. Eksp. Teor. Fiz*, 46:1823, 1964. [Sov. Phys. JETP 19, 1228 (1964)].
- [19] K. von Klitzing. The quantized Hall effect. *Rev. Mod. Phys.*, 58(3):519–531, 1986.
- [20] D. J. Thouless. Quantization of particle transport. *Phys. Rev. B*, 27:6083, 1983.
- [21] A. Bruch, S. V. Kusminskiy, G. Refael, and F. von Oppen. Interacting adiabatic quantum motor. *Phys. Rev. B*, 97:195411, 2018.
- [22] Y. Ji, Y. Chung, D. Sprinzak, M. Heiblum, D. Mahalu, and H. Shtrikman. An electronic Mach-Zehnder interferometer. *Nature*, 422(6930):415–418, 2003.
- [23] F. E. Camino, W. Zhou, and V. J. Goldman. Aharonov-Bohm electron interferometer in the integer quantum Hall regime. *Phys. Rev. B*, 72:155313, 2005.
- [24] Y. Ronen, T. Werkmeister, D. Haie Najafabadi, A. T. Pierce, L. E. Anderson, Y. J. Shin, S. Y. Lee, Y. H. Lee, B. Johnson, K. Watanabe, T. Taniguchi, A. Yacoby, and P. Kim. Aharonov-Bohm effect in graphene-based Fabry-Pérot quantum Hall interferometers. *Nat. Nanotechnol.*, 16(5):563–569, 2021.

- [25] Y. Aharonov and D. Bohm. Significance of electromagnetic potentials in the quantum theory. *Phys. Rev.*, 115:485–491, 1959.
- [26] M. Büttiker. Scattering theory of current and intensity noise correlations in conductors and wave guides. *Phys. Rev. B*, 46:12485–12507, 1992.
- [27] Ya. M. Blanter and M. Büttiker. Shot noise in mesoscopic conductors. *Phys. Rep.*, 336(1-2):1–166, 2000.
- [28] E. R. Mucciolo and C. H. Lewenkopf. TOPICAL REVIEW: Disorder and electronic transport in graphene. *Journal of Physics Condensed Matter*, 22(27):273201, 2010.
- [29] H. B. Nielsen and M. Ninomiya. A no-go theorem for regularizing chiral Fermions. *Physics Letters B*, 105(2-3):219–223, 1981.
- [30] K. Y. Yang, Y. M. Lu, and Y. Ran. Quantum Hall effects in a Weyl semimetal: Possible application in pyrochlore iridates. *Phys. Rev. B*, 84:075129, 2011.
- [31] J. S. Bell and R. Jackiw. A PCAC puzzle: $\pi^0 \rightarrow \gamma\gamma$ in the σ -model, 1969.
- [32] K. A. Madsen, E. J. Bergholtz, and P. W. Brouwer. Josephson effect in a Weyl semimetal junction. *Phys. Rev. B*, 95:064511, 2017.
- [33] A. A. Burkov and L. Balents. Weyl semimetal in a topological insulator multilayer. *Phys. Rev. Lett*, 107:127205, 2011.
- [34] T. Meng and L. Balents. Weyl superconductors. *Phys. Rev. B*, 86:054504, 2012.
- [35] P. W. Anderson. Absence of diffusion in certain random lattices. *Phys. Rev.*, 109:1492–1505, 1958.
- [36] B. Sbierski, G. Pohl, E. J. Bergholtz, and P. W. Brouwer. Quantum transport of disordered Weyl semimetals at the nodal point. *Phys. Rev. Lett*, 113(10):026602, 2014.
- [37] R. Nandkishore, D. A. Huse, and S. L. Sondhi. Rare region effects dominate weakly disordered three-dimensional Dirac points. *Phys. Rev. B*, 89:245110, 2014.
- [38] J. H. Pixley, D. A. Huse, and S. Das Sarma. Rare-region-induced avoided quantum criticality in disordered three-dimensional Dirac and Weyl semimetals. *Phys. Rev. X*, 6:021042, 2016.

- [39] J. H. Pixley, Y.-Z. Chou, P. Goswami, D. A. Huse, R. Nandkishore, L. Radzihovsky, and S. Das Sarma. Single-particle excitations in disordered Weyl fluids. *Phys. Rev. B*, 95:235101, 2017.
- [40] M. Buchhold, S. Diehl, and A. Altland. Nodal points of Weyl semimetals survive the presence of moderate disorder. *Phys. Rev. B*, 98:205134, 2018.
- [41] M. Buchhold, S. Diehl, and A. Altland. Vanishing density of states in weakly disordered Weyl semimetals. *Phys. Rev. Lett.*, 121:215301, 2018.
- [42] B. Sbierski, K. A. Madsen, P. W. Brouwer, and C. Karrasch. Quantitative analytical theory for disordered nodal points. *Phys. Rev. B*, 96:064203, 2017.
- [43] K. S. Novoselov, A. K. Geim, S. V. Morozov, D. Jiang, M. I. Katsnelson, I. V. Grigorieva, S. V. Dubonos, and A. A. Firsov. Two-dimensional gas of massless Dirac Fermions in graphene. *Nature*, 438(7065):197–200, 2005.
- [44] B. A. Bernevig. It’s been a Weyl coming. *Nat. Phys.*, 11(9):698–699, 2015.
- [45] A. Weiße, G. Wellein, A. Alvermann, and H. Fehske. The kernel polynomial method. *Rev. Mod. Phys.*, 78(1):275–306, 2006.
- [46] N. M. R. Peres, F. Guinea, and A. H. Castro Neto. Electronic properties of disordered two-dimensional carbon. *Phys. Rev. B*, 73(12):125411, 2006.
- [47] V. M. Pereira, J. M. B. Lopes Dos Santos, and A. H. Castro Neto. Modeling disorder in graphene. *Phys. Rev. B*, 77(11):115109, 2008.
- [48] S. Wu, L. Jing, Q. Li, Q. W. Shi, J. Chen, H. Su, X. Wang, and J. Yang. Average density of states in disordered graphene systems. *Phys. Rev. B*, 77:195411, 2008.
- [49] K. Ziegler, B. Dóra, and P. Thalmeier. Density of states in disordered graphene. *Phys. Rev. B*, 79(23):235431, 2009.
- [50] K. Kobayashi, T. Ohtsuki, K.-I. Imura, and I. F. Herbut. Density of states scaling at the semimetal to metal transition in three dimensional topological insulators. *Phys. Rev. Lett.*, 112:016402, 2014.
- [51] J. H. Pixley, P. Goswami, and S. Das Sarma. Anderson localization and the quantum phase diagram of three dimensional disordered Dirac semimetals. *Phys. Rev. Lett.*, 115:076601, 2015.
- [52] M. Trescher, B. Sbierski, P. W. Brouwer, and E. J. Bergholtz. Tilted disordered Weyl semimetals. *Phys. Rev. B*, 95(4):045139, 2017.

- [53] *Condensed Matter Field Theory*. Cambridge University Press, Cambridge, 2nd edition.
- [54] N. H. Shon and T. Ando. Quantum transport in two-dimensional graphite system. *J. Phys. Soc. Japan*, 67(7):2421–2429, 1998.
- [55] P. M. Ostrovsky, I. V. Gornyi, and A. D. Mirlin. Electron transport in disordered graphene. *Phys. Rev. B*, 74:235443, 2006.
- [56] M. Noro, M. Koshino, and T. Ando. Theory of transport in graphene with long-range scatterers. *J. Phys. Soc. Japan*, 79(9):094713, 2010.
- [57] I. L. Aleiner and K. B. Efetov. Effect of disorder on transport in graphene. *Phys. Rev. Lett.*, 97:236801, 2006.
- [58] E. Fradkin. Critical behavior of disordered degenerate semiconductors. ii. spectrum and transport properties in mean-field theory. *Phys. Rev. B*, 33:3263–3268, 1986.
- [59] E. Fradkin. Critical behavior of disordered degenerate semiconductors. i. models, symmetries, and formalism. *Phys. Rev. B*, 33:3257–3262, 1986.
- [60] R. R. Biswas and S. Ryu. Diffusive transport in Weyl semimetals. *Phys. Rev. B*, 89:014205, 2014.
- [61] Y. Ominato and M. Koshino. Quantum transport in three-dimensional Weyl electron system — in the presence of charged impurity scattering. *Phys. Rev. B*, 91:035202, 2015.
- [62] B. Sbierski and C. Fräßdorf. Strong disorder in nodal semimetals: Schwinger-Dyson–Ward approach. *Phys. Rev. B*, 99:020201, 2019.
- [63] K. A. Madsen, P. W. Brouwer, P. Recher, and P. G. Silvestrov. Interference effects induced by a precessing easy-plane magnet coupled to a helical edge state. *Phys. Rev. B*, 103:115142, 2021.
- [64] C. L. Kane and E. J. Mele. Quantum spin Hall effect in graphene. *Phys. Rev. Lett.*, 95:226801, 2005.
- [65] B. A. Bernevig, T. L. Hughes, and S.-C. Zhang. Quantum spin Hall effect and topological phase transition in HgTe quantum wells. *Science*, 314(5806):1757–1761, 2006.
- [66] C. Wu, B. A. Bernevig, and S.-C. Zhang. Helical liquid and the edge of quantum spin Hall systems. *Phys. Rev. Lett.*, 96:106401, 2006.

- [67] C. Xu and J. E. Moore. Stability of the quantum spin Hall effect: Effects of interactions, disorder, and z_2 topology. *Phys. Rev. B*, 73:045322, 2006.
- [68] M. König, S. Wiedmann, C. Brüne, A. Roth, H. Buhmann, L. W. Molenkamp, X.-L. Qi, and S.-C. Zhang. Quantum spin Hall insulator state in HgTe quantum wells. *Science*, 318(5851):766–770, 2007.
- [69] L. Du, I. Knez, G. Sullivan, and R.-R. Du. Robust helical edge transport in gated InAs/GaSb bilayers. *Phys. Rev. Lett.*, 114:096802, 2015.
- [70] L. Fu and C. L. Kane. Superconducting proximity effect and Majorana Fermions at the surface of a topological insulator. *Phys. Rev. Lett.*, 100:096407, 2008.
- [71] P. Roura-Bas, L. Arrachea, and E. Fradkin. Helical spin thermoelectrics controlled by a side-coupled magnetic quantum dot in the quantum spin Hall state. *Phys. Rev. B*, 98:195429, 2018.
- [72] D. Gresta, M. Real, and L. Arrachea. Optimal thermoelectricity with quantum spin Hall edge states. *Phys. Rev. Lett.*, 123:186801, Oct 2019.
- [73] L. Arrachea and F. von Oppen. Nanomagnet coupled to quantum spin Hall edge: An adiabatic quantum motor. *Physica E Low-Dimensional Systems and Nanostructures*, 74:596–602, 2015.
- [74] J. Maciejko, C. Liu, Y. Oreg, X.-L. Qi, C. Wu, and S.-C. Zhang. Kondo effect in the helical edge liquid of the quantum spin Hall state. *Phys. Rev. Lett.*, 102:256803, 2009.
- [75] Y. Tanaka, A. Furusaki, and K. A. Matveev. Conductance of a helical edge liquid coupled to a magnetic impurity. *Phys. Rev. Lett.*, 106:236402, 2011.
- [76] B. L. Altshuler, I. L. Aleiner, and V. I. Yudson. Localization at the edge of a 2d topological insulator by Kondo impurities with random anisotropies. *Phys. Rev. Lett.*, 111:086401, 2013.
- [77] T. Posske, C.-X. Liu, J. C. Budich, and B. Trauzettel. Exact results for the Kondo screening cloud of two helical liquids. *Phys. Rev. Lett.*, 110:016602, 2013.
- [78] B. Probst, P. Virtanen, and P. Recher. Controlling spin polarization of a quantum dot via a helical edge state. *Phys. Rev. B*, 92:045430, 2015.
- [79] E. Locane and P. W. Brouwer. Current-induced switching of magnetic molecules on topological insulator surfaces. *Phys. Rev. B*, 95:125437, 2017.

- [80] X.-L. Qi, T. L. Hughes, and S.-C. Zhang. Fractional charge and quantized current in the quantum spin Hall state. *Nat. Phys.*, 4:273, 2008.
- [81] J. König, M. C. Bønsager, and A. H. MacDonald. Dissipationless spin transport in thin film ferromagnets. *Phys. Rev. Lett.*, 87:187202, 2001.
- [82] F. S. Nogueira and K.-H. Bennemann. Spin Josephson effect in ferromagnet/ferromagnet tunnel junctions. *EPL*, 67(4):620–626, 2004.
- [83] E. B. Sonin. Spin currents and spin superfluidity. *Adv. Phys.*, 59(3):181–255, 2010.
- [84] S. Takei and Y. Tserkovnyak. Superfluid spin transport through easy-plane ferromagnetic insulators. *Phys. Rev. Lett.*, 112:227201, 2014.
- [85] S. Takei and Y. Tserkovnyak. Nonlocal magnetoresistance mediated by spin superfluidity. *Phys. Rev. Lett.*, 115:156604, 2015.
- [86] H. Skarsvåg, C. Holmqvist, and A. Brataas. Spin superfluidity and long-range transport in thin-film ferromagnets. *Phys. Rev. Lett.*, 115:237201, 2015.
- [87] C. Xiao, B. Xiong, and Q. Niu. Electric driving of magnetization dynamics in a hybrid insulator. *Phys. Rev. B*, 104:064433, 2021.
- [88] P. Virtanen and P. Recher. Dephasing of spin and charge interference in helical Luttinger liquids. *Phys. Rev. B*, 83:115332, 2011.
- [89] F. Dolcini. Full electrical control of charge and spin conductance through interferometry of edge states in topological insulators. *Phys. Rev. B*, 83:165304, 2011.
- [90] G. Dolcetto, M. Sasseti, and T. L. Schmidt. Edge physics in two-dimensional topological insulators. *Riv. del Nuovo Cim.*, 39:113, 2016.
- [91] J. Maciejko, E.-A. Kim, and X.-L. Qi. Spin Aharonov-Bohm effect and topological spin transistor. *Phys. Rev. B*, 82:195409, 2010.
- [92] J. Strunz, J. Wiedenmann, C. Fleckenstein, L. Lunczer, W. Beugeling, V. L. Müller, P. Shekhar, N. T. Ziani, S. Shamim, J. Kleinlein, H. Buhmann, B. Trauzettel, and L. W. Molenkamp. Interacting topological edge channels. *Nat. Phys.*, 16:83, 2020.
- [93] R. C. O’Handley. *Modern magnetic materials: Principles and applications*. Wiley, New York, NY, 2000.

- [94] C. Brüne, A. Roth, H. Buhmann, E. M. Hankiewicz, L. W. Molenkamp, J. Maciejko, X.-L. Qi, and S.-C. Zhang. Spin polarization of the quantum spin Hall edge states. *Nat. Phys.*, 8(6):485–490, 2012.
- [95] C. Liu, T. L. Hughes, X.-L. Qi, K. Wang, and S.-C. Zhang. Quantum spin Hall effect in inverted type-II semiconductors. *Phys. Rev. Lett.*, 100:236601, 2008.
- [96] D. G. Rothe, R. W. Reinthaler, C.-X. Liu, L. W. Molenkamp, S.-C. Zhang, and E. M. Hankiewicz. Fingerprint of different spin-orbit terms for spin transport in HgTe quantum wells. *New Journal of Physics*, 12(6):065012, 2010.
- [97] P. Sternativo and F. Dolcini. Tunnel junction of helical edge states: Determining and controlling spin-preserving and spin-flipping processes through transconductance. *Phys. Rev. B*, 89:035415, 2014.
- [98] C. P. Orth, G. Strübi, and T. L. Schmidt. Point contacts and localization in generic helical liquids. *Phys. Rev. B*, 88:165315, 2013.
- [99] Y. Tserkovnyak, A. Brataas, and G. E. W. Bauer. Enhanced Gilbert damping in thin ferromagnetic films. *Phys. Rev. Lett.*, 88:117601, 2002.
- [100] Y. Tserkovnyak, A. Brataas, G. E. W. Bauer, and B. I. Halperin. Nonlocal magnetization dynamics in ferromagnetic heterostructures. *Rev. Mod. Phys.*, 77:1375–1421, 2005.
- [101] L. P. Kouwenhoven, A. T. Johnson, N. C. van der Vaart, C. J. P. M. Harman, and C. T. Foxon. Quantized current in a quantum-dot turnstile using oscillating tunnel barriers. *Phys. Rev. Lett.*, 67:1626–1629, 1991.
- [102] H. Pothier, P. Lafarge, C. Urbina, D. Esteve, and M. H. Devoret. Single-electron pump based on charging effects. *EPL*, 17:249, 1992.
- [103] K. A. Madsen, P. W. Brouwer, and M. Breitzkreiz. Equilibrium current in a Weyl semimetal–superconductor heterostructure. *Phys. Rev. B*, 104:035109, 2021.
- [104] B. Yan and C. Felser. Topological materials: Weyl semimetals. *Annu. Rev. Condens. Matter Phys.*, 8:337, 2017.
- [105] A. A. Burkov. Weyl metals. *Annu. Rev. Condens. Matter Phys.*, 9:359, 2018.
- [106] H. B. Nielsen and M. Ninomiya. The Adler-Bell-Jackiw anomaly and Weyl fermions in a crystal. *Phys. Lett. B*, 130(6):389, 1983.

- [107] D. E. Kharzeev. The chiral magnetic effect and anomaly-induced transport. *Prog. Part. Nucl. Phys.*, 75:133, 2014.
- [108] A. A. Burkov. Chiral anomaly and transport in Weyl metals. *J. Phys. Condens. Matter*, 27:113201, 2015.
- [109] J. Xiong, S. K. Kushwaha, T. Liang, J. W. Krizan, M. Hirschberger, W. Wang, R. J. Cava, and N. P. Ong. Evidence for the chiral anomaly in the Dirac semimetal Na₃Bi. *Science*, 350:413, 2015.
- [110] X. Huang, L. Zhao, Y. Long, P. Wang, D. Chen, Z. Yang, H. Liang, M. Xue, H. Weng, Z. Fang, X. Dai, and G. Chen. Observation of the chiral-anomaly-induced negative magnetoresistance: In 3D Weyl semimetal TaAs. *Phys. Rev. X*, 5(3):031023, 2015.
- [111] R. D. dos Reis, M. O. Ajeesh, N. Kumar, F. Arnold, C. Shekhar, M. Naumann, M. Schmidt, M. Nicklas, and E. Hassinger. On the search for the chiral anomaly in Weyl semimetals: The negative longitudinal magnetoresistance. *New J. Phys.*, 18(8):085006, 2016.
- [112] M. M. Vazifeh and M. Franz. Electromagnetic response of Weyl semimetals. *Phys. Rev. Lett.*, 111:027201, 2013.
- [113] D. Kang, Y. Zhou, W. Yi, C. Yang, J. Guo, Y. Shi, S. Zhang, Z. Wang, C. Zhang, S. Jiang, A. Li, K. Yang, Q. Wu, G. Zhang, L. Sun, and Z. Zhao. Superconductivity emerging from a suppressed large magnetoresistant state in tungsten ditelluride. *Nat. Commun.*, 6:7804, 2015.
- [114] Y. Qi, P. G. Naumov, M. N. Ali, C. R. Rajamathi, W. Schnelle, O. Barkalov, M. Hanfland, S.-C. Wu, C. Shekhar, and Y. Sun. Superconductivity in Weyl semimetal candidate MoTe₂. *Nat. Commun.*, 7:11038, 2016.
- [115] L. Zhu, Q.-Y. Li, Y.-Y. Lv, S. Li, X.-Y. Zhu, Z.-Y. Jia, Y. B. Chen, J. Wen, and S.-C. Li. Superconductivity in Potassium-Intercalated Td-WTe₂. *Nano Lett.*, 18(10):6585–6590, 2018.
- [116] S. Cai, E. Emmanouilidou, J. Guo, X. Li, Y. Li, K. Yang, A. Li, Q. Wu, N. Ni, and L. Sun. Observation of superconductivity in the pressurized Weyl-semimetal candidate TaIrTe₄. *Phys. Rev. B*, 99(2):020503(R), 2019.
- [117] R. Wang, L. Hao, B. Wang, and C. S. Ting. Quantum anomalies in superconducting Weyl metals. *Phys. Rev. B*, 93(18):184511, 2016.

- [118] M. D. Bachmann, N. Nair, F. Flicker, R. Ilan, T. Meng, N. J. Ghimire, E. D. Bauer, F. Ronning, J. G. Analytis, and P. J. W. Moll. Inducing superconductivity in Weyl semimetal microstructures by selective ion sputtering. *Sci. Adv.*, 3(5):e1602983, 2017.
- [119] O. O. Shvetsov, V. D. Esin, Yu S. Barash, A. V. Timonina, N. N. Kolesnikov, and E. V. Deviatov. Lateral Josephson effect on the surface of the magnetic Weyl semimetal Co₃Sn₂S₂. *Phys. Rev. B*, 101:035304, 2020.
- [120] O. O. Shvetsov, Y. S. Barash, S. V. Egorov, A. V. Timonina, N. N. Kolesnikov, and E. V. Deviatov. Magnetically stable zero-bias anomaly in Andreev contact to the magnetic Weyl semimetal Co₃Sn₂S₂. *EPL*, 132:67002, 2020.
- [121] D. Sinha. Josephson effect in type-I Weyl Semimetals. *Phys. Rev. B*, 102:085144, 2020.
- [122] P. Dutta, F. Parhizgar, and A. M. Black-Schaffer. Finite bulk Josephson currents and chirality blockade removal from inter-orbital pairing in magnetic Weyl semimetals. *Phys. Rev. B*, 101:064514, 2020.
- [123] M. Alidoust and K. Halterman. Evolution of pair correlation symmetries and supercurrent reversal in tilted Weyl semimetals. *Phys. Rev. B*, 101(3):035120, 2020.
- [124] P. Dutta and A. M. Black-Schaffer. Signature of odd-frequency equal-spin triplet pairing in the Josephson current on the surface of Weyl nodal loop semimetals. *Phys. Rev. B*, 100(10):104511, 2019.
- [125] Y. Kim, M. J. Park, and M. J. Gilbert. Probing unconventional superconductivity in inversion symmetric doped Weyl semimetal. *Phys. Rev. B*, 93:214511, 2016.
- [126] S. Uddin, W. Duan, J. Wang, Z. Ma, and J.-F. Liu. Chiral anomaly induced oscillations in the Josephson current in Weyl semimetals. *Phys. Rev. B*, 99(4):045426, 2019.
- [127] A. Chen and M. Franz. Superconducting proximity effect and Majorana flat bands in the surface of a Weyl semimetal. *Phys. Rev. B*, 93(1):201105(R), 2016.
- [128] A. Chen, D. I. Pikulin, and M. Franz. Josephson current signatures of Majorana flat bands on the surface of time-reversal-invariant Weyl and Dirac semimetals. *Phys. Rev. B*, 95(17):174505, 2017.

- [129] M. Alidoust. Self-biased current, magnetic interference response, and superconducting vortices in tilted Weyl semimetals with disorder. *Phys. Rev. B*, 98(24):245418, 2018.
- [130] U. Khanna, D. K. Mukherjee, A. Kundu, and S. Rao. Chiral nodes and oscillations in the Josephson current in Weyl semimetals. *Phys. Rev. B*, 93(12):121409(R), 2016.
- [131] K. Kulikov, D. Sinha, Y. M. Shukrinov, and K. Sengupta. Josephson junctions of Weyl and multi-Weyl semimetals. *Phys. Rev. B*, 101(7):075110, 2020.
- [132] U. Khanna, S. Rao, and A. Kundu. $0 - \pi$ transitions in a Josephson junction of an irradiated Weyl semimetal. *Phys. Rev. B*, 95(20):201115(R), 2017.
- [133] S.-B. Zhang, J. Erdmenger, and B. Trauzettel. Chirality Josephson current due to a novel quantum anomaly in inversion-asymmetric Weyl semimetals. *Phys. Rev. Lett.*, 121(22):226604, 2018.
- [134] A. Kononov, G. Abulizi, K. Qu, J. Yan, D. Mandrus, K. Watanabe, T. Taniguchi, and C. Schönemberger. One-dimensional states residing on edges and steps in few-layer WTe₂. *Nano Lett.*, 20:4228, 2020.
- [135] Y.-B. Choi, Y. Xie, C.-Z. Chen, J.-H. Park, S.-B. Song, J. Yoon, B. J. Kim, T. Taniguchi, K. Watanabe, H.-J. Lee, J.-H. Kim, K. C. Fong, M. N. Ali, K. T. Law, and G.-H. Lee. Evidence of higher order topology in multilayer WTe₂ from Josephson coupling through anisotropic hinge states. *Nat. Mater.*, 19:974, 2020.
- [136] C. Huang, A. Narayan, E. Zhang, S. Liu, C. Yi, Y. Shi, S. Sanvito, and F. Xiu. Observation of edge states in multilayer WTe₂. *Natl. Sci. Rev.*, 7:1468, 2020.
- [137] O. O. Shvetsov, A. Kononov, A. V. Timonina, N. N. Kolesnikov, and E. V. Deviatov. Realization of a double-slit SQUID geometry by Fermi arc surface states in a WTe₂ Weyl semimetal. *JETP Lett.*, 107(12):774–779, 2018.
- [138] O. O. Shvetsov, A. Kononov, A. V. Timonina, N. N. Kolesnikov, and E. V. Deviatov. Subharmonic Shapiro steps in the a.c. Josephson effect for a three-dimensional Weyl semimetal WTe₂. *EPL*, 124(4):47003, dec 2018.
- [139] S. Howlader, S. Saha, R. Kumar, V. Nagpal, S. Patnaik, T. Das, and G. Sheet. Spin-orbit driven spin depolarization in the ferromagnetic Weyl semimetal Co₃Sn₂S₂. *Phys. Rev. B*, 102:104434, 2020.

- [140] S.-B. Zhang, F. Dolcini, D. Breunig, and B. Trauzettel. Appearance of the universal value e^2/h of the zero-bias conductance in a Weyl semimetal-superconductor junction. *Phys. Rev. B*, 97(4):041116(R), 2018.
- [141] Y. Liu, Z.-M. Yu, and S. A. Yang. Transverse shift in Andreev reflection. *Phys. Rev. B*, 96:121101(R), 2017.
- [142] Z. Hou and Q.-F. Sun. Double Andreev reflections in type-II Weyl semimetal-superconductor junctions. *Phys. Rev. B*, 96(15):155305, 2017.
- [143] W. Chen, L. Jiang, R. Shen, L. Sheng, B. G. Wang, and D. Y. Xing. Specular Andreev reflection in inversion-symmetric Weyl semimetals. *EPL*, 103(2):27006, 2013.
- [144] J. Fang, W. Duan, J. Liu, C. Zhang, and Z. Ma. Pairing-dependent superconductivity gap and nonholonomic Andreev reflection in Weyl semimetal/Weyl superconductor heterojunctions. *Phys. Rev. B*, 97(16):165301, 2018.
- [145] Z. Faraei and S. A. Jafari. Induced superconductivity in Fermi arcs. *Phys. Rev. B*, 100:035447, 2019.
- [146] G. Grabecki, A. Dabrowski, P. Iwanowski, A. Hruban, B. J. Kowalski, N. Olzowska, J. Kołodziej, M. Chojnacki, K. Dybko, A. Łusakowski, T. Wojtowicz, T. Wojciechowski, R. Jakiela, and A. Wiśniewski. Conductance spectra of (Nb, Pb, In)/NbP superconductor/Weyl semimetal junctions. *Phys. Rev. B*, 101(8):085113, 2020.
- [147] Y. Naidyuk, O. Kvitnitskaya, D. Bashlakov, S. Aswartham, I. Morozov, I. Chernyavskii, G. Fuchs, S.-L. Drechsler, R. Hühne, K. Nielsch, B. Büchner, and D. Efremov. Surface superconductivity in the Weyl semimetal MoTe2 detected by point contact spectroscopy. *2D Mater.*, 5(4):045014, 2018.
- [148] A. Kononov, O. O. Shvetsov, S. V. Egorov, A. V. Timonina, N. N. Kolesnikov, and E. V. Deviatov. Signature of Fermi arc surface states in Andreev reflection at the WTe2 Weyl semimetal surface. *EPL*, 122(2):27004, 2018.
- [149] L. Aggarwal, S. Gayen, S. Das, R. Kumar, V. Süß, C. Felser, C. Shekhar, and G. Sheet. Mesoscopic superconductivity and high spin polarization coexisting at metallic point contacts on Weyl semimetal TaAs. *Nat. Commun.*, 8(1):13974, 2017.
- [150] D. Breunig, S.-B. Zhang, M. Stehno, and B. Trauzettel. Influence of a chiral chemical potential on Weyl hybrid junctions. *Phys. Rev. B*, 99(17):174501, 2019.

- [151] Y. Liu, Z.-M. Yu, J. Liu, H. Jiang, and S. A. Yang. Transverse shift in crossed Andreev reflection. *Phys. Rev. B*, 98(19):195141, 2018.
- [152] X.-S. Li, S.-F. Zhang, X.-R. Sun, and W.-J. Gong. Double Andreev reflections and double electron transmissions in a normal-superconductor-normal junction based on type-II Weyl semimetal. *New J. Phys.*, 20(10):103005, 2018.
- [153] H. Li and G. Ouyang. Nonlocal transport in superconducting heterostructures based on Weyl semimetals. *Phys. Rev. B*, 100(8):085410, 2019.
- [154] D. Sinha and K. Sengupta. Transport across junctions of a Weyl and a multi-Weyl semimetal. *Phys. Rev. B*, 99(7):075153, 2019.
- [155] S. Mironov and A. Buzdin. Spontaneous currents in superconducting systems with strong spin-orbit coupling. *Phys. Rev. Lett.*, 118(7):077001, 2017.
- [156] P. Baireuther, J. Tworzydło, M. Breitzkreiz, I. Adagideli, and C. W. J. Beenakker. Weyl-Majorana solenoid. *New J. Phys.*, 19:025006, 2017.
- [157] X. L. Qi and S. C. Zhang. Topological insulators and superconductors. *Rev. Mod. Phys.*, 83(4):1057, 2011.
- [158] C. W. J. Beenakker. Quantum transport in semiconductor-superconductor microjunctions. In E. Akkermans, G. Montambaux, J.-L. Pichard, and J. Zinn-Justin, editors, *Mesoscopic Quantum Physics*, page 279. North-Holland, Amsterdam, 1995.
- [159] P. W. Brouwer and C. W.J. Beenakker. Anomalous temperature dependence of the supercurrent through a chaotic Josephson junction. *Chaos Solit. Fractals*, 8(7-8):1249–1260, 1997.
- [160] T. Suzuki, R. Chisnell, A. Devarakonda, Y.-T. Liu, W. Feng, D. Xiao, J. W. Lynn, and J. G. Checkelsky. Large anomalous Hall effect in a half-Heusler antiferromagnet. *Nat. Phys.*, 12(12):1119–1123, 2016.
- [161] V. Baltz, A. Manchon, M. Tsoi, T. Moriyama, T. Ono, and Y. Tserkovnyak. Antiferromagnetic spintronics. *Rev. Mod. Phys.*, 90:015005, 2018.

Acknowledgments

I want to thank the DFG, for financing my PhD position in the CRC TR 183: "Entangled states of matter", and all the people who supported me during the time I spent working on this PhD thesis.

First and foremost my thanks goes to my advisor Piet Brouwer, for giving me the opportunity to work in his research group, all of his valuable advice, patience and kindness. It was an honor to work together with such a brilliant mind.

I also want to thank my other co-authors Björn Sbierski, Christoph Karrasch, Patrik Recher, Peter Silvestrov and Maxim Breitkreiz for our collaborations on the research projects and articles that became this thesis, and Felix von Oppen for agreeing to be my second advisor. It was a pleasure!

I am also very grateful to have spent time with all of my wonderful colleagues at the DCCQS; the great times at the Mensa, Dice seminars, talks, Christmas parties, conferences and of course coffee breaks will never be forgotten!

My special thanks goes to Jacob Steiner for proof reading, and to Gabriele Herrmann, Annette Schumann-Welde and Andreas Heß for helping me deal with all of the administrative issues that came up.

Last but not least my thanks goes to Zoé, my family and all of my friends and WG, for their continuing emotional support. Without all these people I would not have come this far.

Lebenslauf

Mein Lebenslauf wird aus Gründen des Datenschutzes in der elektronischen Fassung meiner Arbeit nicht veröffentlicht.